

# Quantum computing by optical control of electron spins

Ren-Bao Liu\*

*Department of Physics, The Chinese University of Hong Kong, Hong Kong, China*

Wang Yao†

*Department of Physics, The University of Hong Kong, Hong Kong, China*

L. J. Sham‡

*Department of Physics, University of California San Diego, La Jolla, California 92093-0319*

We review the progress and main challenges in implementing large-scale quantum computing by optical control of electron spins in quantum dots (QDs). Relevant systems include self-assembled QDs of III-V or II-VI compound semiconductors (such as InGaAs and CdSe), monolayer fluctuation QDs in compound semiconductor quantum wells, and impurity centers in solids such as P-donors in silicon and nitrogen-vacancy centers in diamond. The decoherence of the electron spin qubits is discussed and various schemes for countering the decoherence problem are reviewed. We put forward designs of local nodes consisting of a few qubits which can be individually addressed and controlled. Remotely separated local nodes are connected by photonic structures (microcavities and waveguides) to form a large-scale distributed quantum system or a quantum network. The operation of the quantum network consists of optical control of a single electron spin, coupling of two spins in a local nodes, optically controlled quantum interfacing between stationary spin qubits in QDs and flying photon qubits in waveguides, rapid initialization of spin qubits, and qubit-specific single-shot non-demolition quantum measurement. The rapid qubit initialization may be realized by selectively enhancing certain entropy dumping channels via phonon or photon baths. The single-shot quantum measurement may be in-situ implemented through the integrated photonic network. The relevance of quantum non-demolition measurement to large-scale quantum computation is discussed. To illustrate the feasibility and demand, the resources are estimated for the benchmark problem of factorizing 15 with Shor's algorithm.

arXiv:1006.5544v1 [quant-ph] 29 Jun 2010

---

\* Email: rliu@cuhk.edu.hk

† Email: wangyao@hkucc.hku.hk

‡ Corresponding author. Email: lsham@ucsd.edu

## CONTENTS

I. Introduction	3
II. Spin Qubits in Quantum Dots	6
A. Confinement of a single electron in a quantum dot	6
B. Energy levels in a charged quantum dot	7
C. Spin relaxation and decoherence in quantum dots	8
D. Decoherence by an interacting nuclear spin bath	9
1. Single electron in a mesoscopic bath of interacting nuclear spins	10
2. Nuclear spin pair-flip excitations and pair correlation approximation	11
3. Timescales of single spin decoherence and ensemble spin echo decay	13
E. Coherence restoration and protection in the nuclear spin bath	14
F. Summary: Quantum dot opportunity	16
III. Physical Structure	18
A. Local nodes	18
B. Distributed structure	20
IV. One- and Two-Qubit Operations	23
A. Single-spin rotation by Raman process	23
B. Two-qubit gates by optical RKKY interaction	25
1. SWAP and $\sqrt{\text{SWAP}}$ gates	27
2. Controlled phase gate	27
C. Issues to be considered	28
V. Qubit Initialization	28
A. Initialization by entropy dumping to photon baths	29
1. Optical pumping	29
2. Single-shot initialization with cavity enhancement	31
B. Initialization by entropy dump to phonon baths	33
VI. Quantum Non-demolition Measurement of Spin Qubits	34
A. Scalability of quantum measurement in quantum computation	35
B. Quantum non-demolition measurement via cavity quantum electrodynamics	36
VII. Networking Local Nodes	37
A. Dot-Cavity-Waveguide structure as spin-photon interface	39
B. Control of spin-photon interface	40
C. Inter-node operations in a quantum network	42
D. Operations with imperfections	43
1. Intrinsic photon leakage into free space	43
2. Unwanted coupling to energy levels beyond the 3-level $\Lambda$ system	43
3. Unknown parameter offsets	44
4. Laser intensity fluctuations	44
5. Laser phase fluctuations	45
6. Deterministic phase and shape variations in photon propagation	45
7. Loss and indeterministic fluctuation in photon propagation	45
E. Summary: Coherent quantum manipulation by remote control	45
VIII. Challenges	46
A. Resource estimate for Shor's algorithm for factorizing 15	46
B. Technologies most needed	49
1. Complex multi-pulse optics	49
2. System fabrication and characterization	49
3. Nano-photonics	50
IX. Conclusion	50

Acknowledgements	51
A. Hole-mixing and selection rules in a quantum dot	51
B. Theory of electron spin decoherence by interacting nuclear spins	53
a. Formal theory of decoherence in a nuclear spin bath	54
b. Pair correlation approximation and pseudo-spin picture	55
C. Quantum measurement in Shor’s algorithm	56
1. Order finding for Shor’s algorithm	56
2. Issues with the measurement	57
3. Ensemble measurement	57
a. Correlated measurement	58
b. Uncorrelated measurement	58
4. Single-object measurement with error	59
5. Quantum non-demolition measurement	60
D. Elementary quantum gates	62
References	62

## I. INTRODUCTION

Based on the quantum parallelism rooted in the superposition principle of quantum mechanics, quantum computers are expected to dramatically outperform their classical counterpart, particularly with exponential speedup in solving some hard problems such as factoring [1]. Toward the ambitious realization of practical quantum computation such as factoring a million-bit number, enormous efforts are still to be put on both the design and invention of software (quantum algorithms) and the hardware development (physical implementation). Here we are mostly interested in the latter part. In principle, all quantum systems (which arguably amount to all physical systems) could be considered for the physical realization. But certain qualifications (such as the DiVincenzo criteria [2]) are to be fulfilled for them to be brought into consideration. Still there is a vast range of systems in the candidate pool, including nuclear spins in liquids [3–7], trapped ions or atoms [8–18], atoms in optical lattices [19–24], photons [25–34], superconducting circuits [35–55], electrons suspended over liquid helium surfaces [56–59], molecular magnets [60], nuclear spins in solids [61, 62], electron spins in semiconductor quantum dots (QDs) [63–79], hole spins in QDs [80, 81], electron spins in impurity centers in semiconductors such as phosphorus donors in silicon [82–86] and nitrogen-vacancy (NV) centers in diamonds [87–100], and non-Abelian anyon excitations in quantum matters with topological orders [101–105]. Here we concentrate on solid-state systems, and in particular on electron spins in semiconductors, while nuclear spins therein are also considered either as an adverse noise source or as a beneficial information storage [106, 107]. Electrical, magnetic and/or optical means may be employed to access and/or manipulate the spins. In this review, we discuss the optical operations which may be applied to electron spins in III-V compound semiconductors where the direct band-gaps facilitate controllable optical transitions.

We shall not give an overall review of different schemes under current investigation for quantum computation. A comprehensive review of progresses and challenges in research of different systems may be found, e.g., in the Quantum Computation Roadmap published by Quantum Institute, LANL. It, however, would be useful to have a perspective of the position and connections of the systems under review in the global picture of quantum computation research. As compared with their “soft” counterparts such as trapped atoms or ions, cavity-trapped or flying photons, electrons floating on liquid helium surfaces, and nuclear spins in liquids, the “hard” solid-state systems as candidates for quantum computers have the advantages of stability and integratability, but have the disadvantages of relatively short coherence time due to interactions with complex environments in solids. The solid-state systems under current investigation include superconducting circuits, nuclear spins in solids, and electron spins in semiconductors. While the qubits in superconducting circuits are made of excitations with macroscopic coherence in superconductors under designed confinement, nuclear or electron spins are natural qubit carriers since the information can be encoded in an intrinsic degree of freedom of elementary particles and thus are very stable. For example, while a superconducting qubit may be lost during the measurement and control processes, a spin qubit would always exist unless the hosting particle like a nucleus or an electron disappears (by decay, ionization, thermal activation, etc.). Also, a spin does not feel an electrical field directly, which makes spins less vulnerable than superconducting qubits to charge or current noises from environments or operating devices. The decoherence of spin qubits may be caused by coupling to other environmental spins, local magnetic field fluctuations, or phonon scattering via spin-orbital interaction, all of which are usually rather weak in semiconductors. So the coherence time of spins are usually very long at low temperature and under a moderately strong magnetic field, varying from microseconds to milliseconds for electron spins (excluding the inhomogeneous broadening effect) [108–111], and longer than

seconds for nuclear spins [112–115]. The weak coupling of spins to environments, of course, has also detrimental effects – the control, initialization and measurement of spins are all challenging tasks. In this regard, electron spins are more tractable than nuclear spins. Nuclear spins have longer coherence memory time but slow operating rate and low detection efficiency. Electron spins are relatively more controllable but less resilient to decoherence. Schemes have been pursued to combine the advantages of the two kinds of systems by using nuclei as storage [106, 107, 116] and electrons as operating units and interfaces [117]. The coupling between nuclear and electron spins is the hyperfine interaction. The hyperfine interaction is a main mechanism causing electron spin decoherence, but it can also be utilized to realize coupled qubit systems.

Electron spin qubits can be formed in various structures, such as doped electrons in QDs and impurities in solids. The fabrication of such systems with designed patterns and structures is possible because of the advances in modern semiconductor technologies and nano-technologies – compatibility with the modern semiconductor industry is an extra advantage of using electron spins as qubits in quantum computation. The direct pump, control and probe of electron spins may be done by electron spin resonance techniques with microwave pulses [88, 110, 111, 117]. For faster operation clock as desired, the electron spin states may be converted to other degrees of freedom through quantum interfacing (the same as one does from nuclear spin states to electron spin states). Then electron spins may be accessed indirectly by control of agents such as excitons in semiconductors and photons generated by recombination of excitons [64, 68–79, 118–120]. Quantum interfacing between spins and photons [119] makes also possible quantum communication between distributed quantum nodes which is required for scalable quantum computation. In this sense, the direct-gap semiconductors such as InAs and GaAs, where ultrafast optical control and interfacing are possible, have some advantages over the indirect gap materials such as silicon, where electrical gating and microwave pulses may be the only possible means of control. As compared with silicon, a main concern with the III-V materials is the much shorter spin coherence time due to the abundance of nuclear spins as noisy environments (in GaAs, e.g., the electron spin coherence time is in the order of microseconds, while in silicon, it is in milliseconds, excluding the effects of phonon scattering and inhomogeneous broadening) [121–132]. Fortunately, there already exist various schemes to elongate the spin coherence time by orders of magnitude, via dynamical control [130, 133–142], or nuclear state preparation [113–115, 143–151].

All these said, we would like to remark that at this point, it would be premature to discourage effort in exploring different physical systems, existing or emerging. It is conceivable that the future quantum computers will be realized by combination of innovative technologies, ideas, concepts, and synthesis of materials and systems. For instance, the idea of topological quantum computation may be implemented with trapped atoms in optical lattice [152]; the systems under the focus of this review involve both stationary electron spins and flying photons [119], which may also be applied to coupled systems of photons and superconducting qubits [47, 49–51]; semiconductor chips may provide micro-trap for ions; photon-based quantum computation may use quantum lights from trapped ions [153], atoms [154, 155], or QDs [156, 157]; and so on. In the present initial stage of quantum computation technology, it would be highly risky to exclude certain candidates just because of difficulties encountered in the beginning of the adventure, since different systems may have their bottleneck problems at different stages. In particular, solid-state systems, while promising with their large-scale stability and integratability in the future, are still facing severe obstacles of environmental noise and control errors for one or a few qubits. In this review, based on many experimentally demonstrated elements and theoretically proposed schemes, we would like to put forward blue prints of relatively large-scale quantum computing via optical control of electron spins in QDs. We should point out that such targets are by no means easy and still require significant advances of technologies and concepts. Also, although our discussions, to be specific, will be based on electron spins in InAs or GaAs QDs, the schemes, with certain modifications, can be applied to a few emerging novel systems such as hole spins in QDs and NV centers in diamond, where the physics is similar to electron spins in QDs.

There are two main concerns with solid-state systems for quantum computation, when compared with their atomic peers like trapped ions or atoms. One is how to fabricate and construct a large array of reproducible or identical qubit units (such as QDs). And the other one is the many-body problem.

The fabrication issue is even worse for the systems to be discussed in this review, namely, QDs under optical control. Most

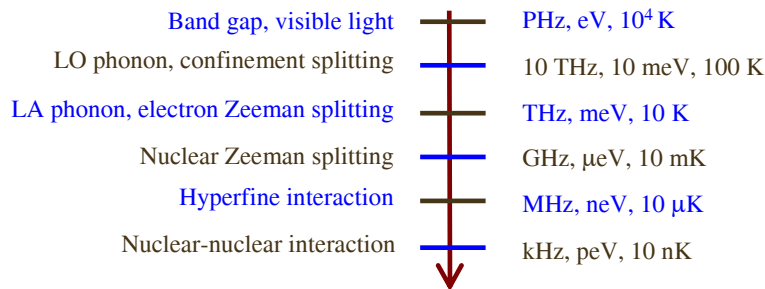


FIG. 1. Relevant energy scales for a typical GaAs semiconductor QD, in terms of frequency, energy, and temperature. The hyperfine constant refers to the interaction between a single nucleus and an electron.

likely, the QDs are formed by molecular beam epitaxy (MBE) growth process such as the self-assembled QDs and the fluctuation QDs. Effort is being made on growth process so well controlled that all the QDs are almost identical and regularly located. There are also such promising systems as impurities in semiconductors such as phosphorus donors in silicon [83] and the NV centers in diamond [158, 159] where the nanometer-precision ion implantation technology may allow a patterned array of qubits represented by the electron spins in the impurity centers. In the foreseeable future, however, we may have to live with the problem of the irregularity. On the positive side, we could take advantage of the irregularity produced by the system fabrication. In small systems for demonstration purposes, the varying size and position of QDs may be used as fingerprints by which different qubits may be addressed and individually controlled by light beams which usually have resolution no better than half the wavelength.

The many-body problem raises two related questions: Can an isolated qubit be properly defined at all among so many particles, and will a coherent superposition state of a qubit last long enough for quantum gates before it collapses due to decoherence in the noisy environment?

It turns out [160] that large gaps between valence bands and conduction bands in semiconductors protect elementary excitations such as excitons and electrons so well that an extra electron doped in a QD is well-defined as a single particle moving with a renormalized effective mass and coupling constants such as the g-factor, in analogy to a low-energy electron in the Dirac sea. The protective gap sets a fundamental limit on the operation speed of quantum computation in solid-systems. Such a limit is far from being approached in current experiments, whether in typical semiconductors where the gap is about 1 eV (for fs-order operation time) or a few meV in superconductors.

In optical control of spins in QDs, decoherence is caused mainly by three mechanisms, namely, coupling to nuclear spins of the host lattice [108, 121–132, 161], phonon scattering [162–168], and spontaneous photon emission during the optical control [68, 169]. For some pseudo-spin qubits with orbital-state dependence (such as the singlet-triplet qubits [108]), the charge fluctuation may also contribute to the environment noise [170, 171]. Besides the standard quantum error correction protocols [172], there are specific strategies to deal with various decoherence mechanisms, which are needed anyway to achieve fidelity of quantum gates above the threshold for quantum error correction. The spontaneous photon emission could be suppressed by completing the optical control rapidly or via off-resonance (virtual) excitation [68, 72, 76, 173]. The phonon scattering may be quenched simply by lowering the temperature to a few kelvins [162–165, 174–177] or by using light-element materials such as diamond [87–100] or organic materials [178, 179] where the spin-orbital coupling is weak. The nuclear spins, being a slow bath, may have their decoherence controlled by certain dynamical decoupling or disentanglement control [130, 133–142]. Again, the normally harmful noise sources could be made useful by design. The photon and phonon baths are rapid entropy dumping pools when certain quantum channels are selectively enhanced [120]. The photon emission, when enhanced by cavities and guided by quantum channels, is an important basis for quantum communication between remotely separated qubits [76, 119]. The nuclear spins, having very slow dynamics, are considered as good local quantum memories [106, 107, 116] with an electron spin in contact acting as a mediator for quantum information operation and transfer.

To achieve large-scale quantum computation, consensus has been reached on several criteria to be fulfilled, known as the “DiVincenzo criteria” [2]. We quote these criteria below as the guidelines for reviewing the progresses and main challenges toward the realization of quantum computation by optical control of electron spins in QDs:

1. *A scalable physical system with well characterized qubits;*
2. *The ability to initialize the state of the qubits to a simple fiducial state;*
3. *Long relevant decoherence times, much longer than the gate operation time;*
4. *A universal set of quantum gates;*
5. *A qubit-specific measurement capability;*
6. *The ability to interconvert stationary and flying qubits;*
7. *The ability faithfully to transmit flying qubits between specified locations.*

The stationary qubits under our focus are well defined by electron spins in QDs, and the flying qubits carrying quantum information between distributed nodes are photons flying in waveguides. We will discuss in more details the decoherence of the spin qubits and show that the decoherence time ( $\sim 10^{-6}$  sec in a typical GaAs QD with the inhomogeneous broadening excluded [108, 109, 115, 147, 180, 181]) is indeed much longer than the quantum gate operation time ( $\sim 10^{-11}$  sec [79, 181, 182]). The one- and two-qubit gates, which form a universal set [172, 183, 184], are realized by optical excitation of charged excitons. Some fundamental physics issues with the initialization and quantum measurement of qubits will be reviewed. Measurement and initialization are put together because they are related to the same physical process. Initialization disposes of entropy to the environment while in measurement the environment acts as part of a readout device. For a large-scale quantum computation blueprint, we use designs of local nodes of a few qubits and structures of distributed nodes connected by quantum channels which may be realized by photonic elements such as waveguides and microcavities. Control schemes of quantum interfacing are also an important topic to be covered. To illustrate the feasibility and demands of the quantum computation in the discussed

systems, the resources, in terms of the number of optical pulses and operation time (compared with the spin decoherence time), will be estimated for the benchmark problem of factoring 15 with Shor's algorithm.

## II. SPIN QUBITS IN QUANTUM DOTS

In this section, we begin (in Sec. II A) with a brief review of the confinement of single electrons in optically controllable semiconductor QDs, followed (in Sec. II B) by discussions of QD energy level structures and optical properties. In Sec. II C, we briefly outline recent theoretical and experimental results on the spin coherence properties of single electrons confined in QDs. Both theories and experiments show that, as phonon mechanisms are suppressed at low temperature ( $\sim 4$  K and below), lattice nuclear spins become the dominant cause for the electron spin decoherence. In Sec. II D, we review the theory of electron spin decoherence by interacting nuclear spins in a QD. Coherence protection of electron spin in the interacting nuclear spin bath is possible by applying a sequence of  $\pi$  pulses to the electron, as discussed in Sec. II E. In Sec. II F, an overview of QD electron spins as qubits is given from the perspective of fault-tolerance requirement for scalable quantum computation, and two other promising spin qubit systems, namely, hole spins and NV center spins, are also discussed.

### A. Confinement of a single electron in a quantum dot

Two types of MBE grown QDs formed in direct bandgap III-V compounds offer a great deal of controllability by ultra-fast optics and are being investigated as building blocks for optically manipulated quantum computers.

The first is referred to as interface fluctuation formed QDs in GaAs/AlGaAs quantum well structures [185–193]. We will refer them in short as GaAs fluctuation QDs. As illustrated in Fig. 2(a) and 3, an electron in such a structure is confined in the growth direction along the  $z$  axis in a low bandgap GaAs layer, with a thickness of tens of Å, between two higher bandgap  $\text{Al}_x\text{Ga}_{1-x}\text{As}$  layers. In the III-V materials, the conduction band minimum occurs at the  $\Gamma$  point in the momentum space and the heterostructure wavefunction of the electron is constructed from the conduction band Bloch functions in the vicinity of the  $\Gamma$  point. Thus the difference in energy of the conduction band minimum in the high and low bandgap materials form a square well potential for electron in the growth direction. The band discontinuity in the interface of the low and high bandgap material is typically hundreds of meV so that the vertical confinement is strong. Growth interruption leads to roughness at the material interfaces, usually a thickness fluctuation of one monolayer. Electron confinement within the plane of the quantum well (in the  $x$  and  $y$  directions) is caused by the quantum well thickness fluctuation. The energy lift by the quantum confinement in the  $z$  direction is roughly  $\frac{\hbar^2}{2m^*}(\frac{\pi}{d})^2$  for the lowest energy state, where  $m^*$  is the effective mass of conduction electron and  $d$  is the quantum well thickness. This energy lift is larger where the quantum well is thinner. Therefore lateral confinement is formed where the quantum well has an island. Fig. 3 shows schematically how monolayer-size fluctuation in a quantum well gives rise to the localized envelope function in the plane. The energy scale of this lateral confinement is typically of several to tens of meV in GaAs fluctuation dot. A GaAs fluctuation dot with lateral size  $\sim 40$  nm can hold several localized energy levels with level spacing of several meV.

The second type of QDs, referred as InAs self-assembled dots, are formed using the Stranski-Krastanow growth mode which utilizes the strain caused by the lattice mismatch between InAs layers and GaAs substrates. InAs self-assembles into islands which are primarily in the shape of a pyramid [see Fig. 2 (b)], with a height of tens of Å and a base size of tens of nanometers [196–199]. In an InAs self-assembled QD, the lateral confinement is much stronger due to the pyramid structure, and the smaller dot size leads to level spacing of  $\sim 10$  meV or larger.

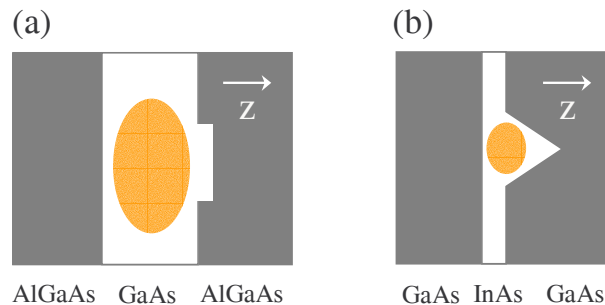


FIG. 2. Illustration of two types of optically controllable QDs. The arrows indicate the growth direction. The ellipse regions show schematically the confinement of electrons in the dots. (a) A GaAs fluctuation QD. (b) An InAs self-assembled QD.

For a GaAs fluctuation QD, a single conduction band electron can be incorporated in the dot by modulation Si doping in the barriers [200]. For an InAs self-assembled dot, gate voltage tuning in an  $n^+$ -intrinsic-Schottky diode structure is a more controllable way to charge and discharge the QD with a single electron [194, 195] (see the schematic illustration in Fig. 4). The qubit is typically encoded in the spin subspace of the lowest energy level of the single electron in the QD.

There are other notable systems where single electrons are localized in nanoscale regions in semiconductors. These include the confinement by electric gates on top of two-dimensional electron gas in GaAs [63, 201, 202], and the localization by impurities such as phosphorus donors in silicon [82–86] or NV centers in diamond [88, 92–98, 100, 117, 203, 204]. The spins of single electrons localized in these systems are also under extensive investigation as qubit carriers.

## B. Energy levels in a charged quantum dot

Control of a spin qubit makes use of a larger Hilbert space in a QD, involving optical transitions from valance bands to conduction bands. In this subsection, we briefly describe the relevant energy level structures and the corresponding optical transition selection rules.

A direct interband transition creates an additional electron in the conduction band by leaving a hole in the valance band. At the  $\Gamma$  point, the fourfold degeneracy of the bulk  $\Gamma_8$  valance band is lifted by the quantum well confinement effect. The top valance subband is a doublet derived from the  $J_z = \pm 3/2$  bulk band, which is also denoted as the “heavy hole” band (see Appendix. A). Other valance bands are irrelevant in our control schemes as they are always far off-resonance. Electrons can be excited from the valance band states of angular momentum  $J_z$  to conduction band states of spin  $S_z$  by absorbing a photon, with the selection rule  $S_z = J_z + \sigma$  where  $\sigma = \pm 1$  corresponds to the circular polarization of light. Therefore, the single electron states are optically coupled to the charged exciton states (also known as trion states) composed of two conduction electrons and one heavy hole. Fig. 5 shows schematically two different types of trion states. The two electrons in Fig. 5(a) occupy different electronic levels of the QD and the two electrons in Fig. 5(b) are in a spin singlet configuration on the same electronic level. The energy spacing between different trion configurations is  $\sim 1 - 10$  meV depending on the QD size. The bandwidth and Rabi frequency of the optical field is much smaller than this energy spacing. So when the frequency of the optical field is near the resonance of one type of trion configuration, the remaining trion configurations can be neglected.

Most manipulation schemes use the ground state trions [Fig. 5(b)] to mediate optical control of the spin. In such cases, the relevant Hilbert space is composed of the two single electron spin states and the two ground state trions (see Fig. 6). For simplicity, we use below the  $e_{\pm}^{\dagger}$  to denote the creation of a conduction band electron of  $S_z = \pm 1/2$  in the lowest energy level of the QD and similarly  $h_{\pm}^{\dagger}$  to denote the creation of a heavy hole with  $J_z = \pm 3/2$  (annihilation of an electron with  $J_z = \mp 3/2$ ).

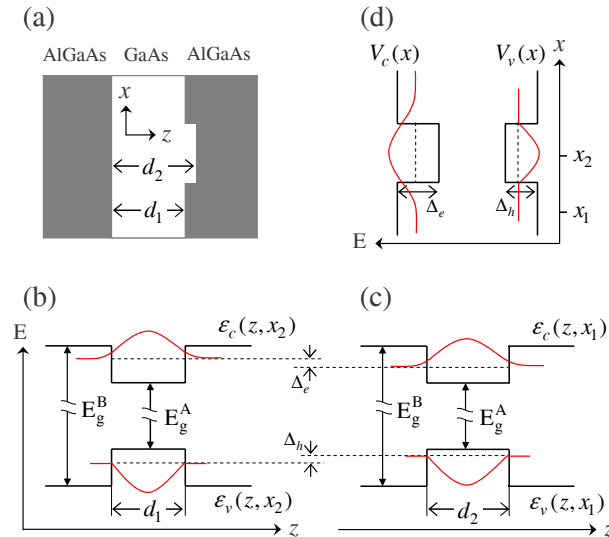


FIG. 3. Schematics of the three-dimensional confinement of electrons and holes in a GaAs fluctuation QD. (a) Interface fluctuation, typically of one monolayer, forms a fluctuation dot. The bright region is the GaAs material and the dark regions are AlGaAs. (b) Vertical confinement for electrons and holes in the growth direction (the  $z$  direction) at  $x = x_1$  where the quantum well is thinner  $d = d_1$ . (c) Vertical confinement in the growth direction at  $x = x_2$  where the quantum well is one monolayer thicker  $d = d_2$ . (d) The difference of the energy lift by vertical confinement in regions of different thickness forms a lateral confinement for the electrons and holes.

The relevant Hilbert space for optical control of spin is:  $|\uparrow\rangle \equiv e_+^\dagger|G\rangle$ ,  $|\downarrow\rangle \equiv e_-^\dagger|G\rangle$ ,  $|t_{\frac{3}{2}}\rangle \equiv e_+^\dagger e_-^\dagger h_+^\dagger|G\rangle$  and  $|t_{-\frac{3}{2}}\rangle \equiv e_+^\dagger e_-^\dagger h_-^\dagger|G\rangle$  where  $|G\rangle$  denotes the configuration with empty conduction bands and full valence bands. The transition selection rule between these four states is shown in Fig. 6(a). For different control schemes, the selection rules represented in other basis sets are also useful. In Fig. 6(b) and (c), we have changed the basis for the spin states and the trion states so that the electron spin states are eigenstates along  $x$ -direction and the trion states are  $|T\pm\rangle \equiv (|t_{3/2}\rangle \pm |t_{-3/2}\rangle) / \sqrt{2}$ . The selection rule can also be represented with the linearly polarized basis for the optical field as shown in Fig. 6(c) [118]. The selective coupling of the QD transitions with light of different polarizations offers sufficient freedom for optical control of the spin. Depending on the polarization and frequency of the optical field, various optical pathways can be established to realize the control in the spin subspace via a second order process through the trion. For example, if the optical field is  $\sigma+$  circularly polarized [Fig. 6(b)], the  $|t_{-\frac{3}{2}}\rangle$  trion state is decoupled from optical field and the relevant dynamics is in a  $\Lambda$ -type three-level system. Raman processes in such three-level systems are central to the optical control of spin dynamics as will be discussed in details later.

### C. Spin relaxation and decoherence in quantum dots

Coherence properties of qubits are crucial to quantum information processing. Spin decoherence of a single electron in a solid results from the coupling to various environmental modes. Typical optical manipulations of spin qubits in QDs are performed in the Voigt or Faraday geometry with a strong magnetic field ( $\sim 1 - 10$  T), and at low temperature ( $\sim$  or  $<$  K) to suppress thermal excitations in the environment [205, 206]. In this subsection, we single out the environmental effects that dominate the spin decoherence under these experimental conditions.

We first show the quantum mechanics of decoherence due to the coupling to a general environment [207–209]. The initial state of the electron spin,  $|\varphi^s(0)\rangle = C_+|\uparrow\rangle + C_-|\downarrow\rangle$ , is prepared as a coherent superposition of the spin up and down states  $|\pm\rangle$  in an external magnetic field. The state of the total system of the spin plus bath at that instant forms an *unentangled* state,  $|\Psi(0)\rangle = |\varphi^s(0)\rangle \otimes |\mathcal{J}\rangle$ . It evolves over time  $t$  to  $|\Psi(t)\rangle = C_+(t)|\uparrow\rangle \otimes |\mathcal{J}^+(t)\rangle + C_-(t)|\downarrow\rangle \otimes |\mathcal{J}^-(t)\rangle$  where the bath states  $|\mathcal{J}^+(t)\rangle$  and  $|\mathcal{J}^-(t)\rangle$  are generally different. The mixed state of the electron spin is determined by its reduced density matrix obtained by tracing over the environment states  $\rho_{\sigma,\sigma'}^s(t) = C_{\sigma'}^*(t)C_\sigma(t)\langle\mathcal{J}^{\sigma'}(t)|\mathcal{J}^\sigma(t)\rangle$ . The diagonal element of the reduced density matrix  $\rho_{\sigma,\sigma}^s$  gives the probability of finding the spin in state  $|\sigma\rangle$ . Either off-diagonal element is a measure of the spin phase coherence. The environment-driven transfer of the probability between the spin states is known as the longitudinal relaxation, while the loss of the off-diagonal element is known as the transverse decoherence. The longitudinal relaxation also contributes to the transverse decoherence. The spin decoherence without longitudinal relaxation is called pure dephasing, characterized by the quantity  $\langle\mathcal{J}^+(t)|\mathcal{J}^-(t)\rangle$ . Pure dephasing is thus a consequence of system-bath entanglement when the bath evolution  $|\mathcal{J}^\pm(t)\rangle$  is conditioned on the system states  $|\pm\rangle$ . The above discussion can be generalized to the situation where the environment is initially in a mixed state. The single electron plus its environment is then described at the initial time by the density matrix  $\rho(0) = |\varphi^s(0)\rangle\langle\varphi^s(0)| \otimes \sum_{\mathcal{J}} P_{\mathcal{J}}|\mathcal{J}\rangle\langle\mathcal{J}|$ , where the reduced density matrix for the electron at any moment is  $\rho_{\sigma,\sigma'}^s(t) = \sum_{\mathcal{J}} P_{\mathcal{J}} C_{\sigma'}^*(t)C_\sigma(t)\langle\mathcal{J}^{\sigma'}(t)|\mathcal{J}^\sigma(t)\rangle$ .

Novel experimental techniques have been developed in the past several years for measurement of the spin relaxation and decoherence in QDs. In GaAs fluctuation dots and InAs self-assembled QDs, optical techniques are commonly used for measuring the spin  $T_1$  time. These include the time domain measurement by optical generation and detection of non-equilibrium spin population [176], and the frequency domain approach of the coherent phase-modulation spectroscopy [177]. In gate-defined QDs,

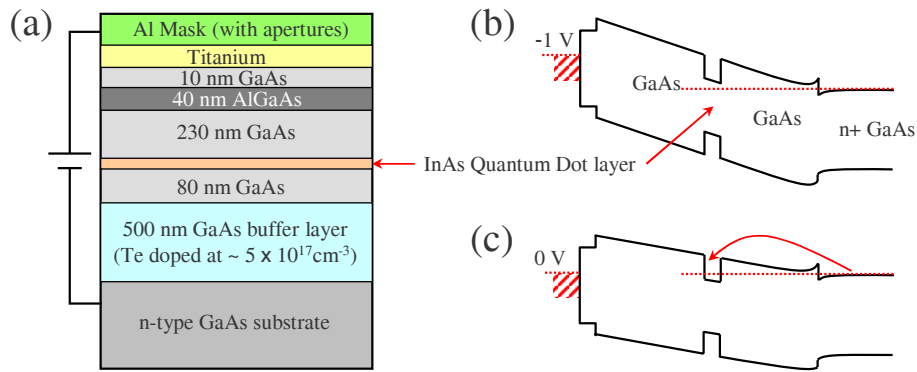


FIG. 4. Gate controlled charging of an InAs self-assembled QD in an  $n^+$ -intrinsic-Schottky (NIS) diode structure. (a) Schematic illustration of the NIS diode structure given in [194, 195]. (b) Band diagram of the NIS diode structure where the InAs QD is uncharged. (c) An InAs QD charged with a single electron.



spin-to-charge conversion can be implemented to trace the time evolution of the initially created spin population [174, 175]. In strong magnetic field of  $\sim 1 - 10$  T and at low temperature ( $\lesssim 1$  K), the experimentally measured value  $T_1 \sim 10^{-4} - 10^{-2}$  s [174–177] are in good agreement with the theoretical predictions of the spin longitudinal relaxation induced by phonon [162–165]. In a recent experiment by Amasha *et al.* [210], spin relaxation rate of a single electron in a lateral QD is studied when the orbital wavefunction is manipulated using gate voltages. The measured dependence of  $T_1$  on orbital confinement and magnetic field is in excellent agreement with theory [163, 166], which confirms that phonon scattering in the presence of spin-orbit coupling is the dominant cause for spin relaxation in magnetic field down to 1 T. In low magnetic field and when spin-orbit coupling strength is weak,  $T_1$  as long as 1 sec is observed [210].

Transverse decoherence may be measured in optically accessible QDs by the frequency domain approach utilizing the Hanle effect [112], or by the time domain pump-probe measurement. In the later approach, a circularly polarized pump pulse initiates spin polarization in the growth direction, whose precession about an in-plane magnetic field is tracked by the differential transmission of a circularly polarized probe beam [205] or the Faraday rotation angle of a linearly polarized probe beam [211]. In a gate-defined double-dot structure, the spin-to-charge conversion process can also be implemented to probe the relative coherence between states of a coupled spin pair, which provides information about the decoherence of a single spin [202, 212]. In these experiments, transverse decoherence times of  $T_2^* \sim 1 - 10$  ns were obtained either from measurements on spatial ensembles of QDs [205, 211, 213] or from time-ensemble measurements of single dots [112, 202, 212]. Spin echo type of measurement was also performed on the gate-defined single GaAs dot [108, 180], which showed an echo decay time of  $T_H \sim \mu\text{s}$ . The sharp difference between  $T_H$  and  $T_2^*$  suggests that the ensemble dephasing is mainly affected by the inhomogeneous broadening of the local environment of the QDs, which is removed in the spin echo measurement. Greilich *et al.* have shown that by using a periodic train of circularly polarized light pulses to excite an ensemble of InAs self-assembled QDs, spin polarization is amplified only in a subset of the ensemble where the electron spin Zeeman frequency has to be an integer multiple of the pulse repetition frequency [109]. These quasi-discrete spectra leads to constructive interference of the spin precession at each pulse arrival time. As dephasing by inhomogeneous broadening is thus removed, single spin  $T_2 \sim \mu\text{s}$  is obtained [109, 124, 146, 150, 151]. Very recently, Hahn echo measurement was also made possible for impurity spins in GaAs where rotations of spins were achieved by ultrafast optical pulses [181]. The measured Hahn echo decay time is  $6 \mu\text{s}$ , consistent with theories and other experiments.

These experiments all show that transverse decoherence times ( $T_2^*$ ,  $T_H$  and  $T_2$ ) are orders of magnitude faster than the longitudinal relaxation time  $T_1$ . On the other hand, theoretical analysis of the phonon mechanisms concludes that pure dephasing due to phonon is well suppressed at the temperature where these experiments are performed ( $\lesssim 1$  K) [166, 167]. As phonon is unlikely to be responsible for the observed fast transverse decoherence, the remaining possibility is then the nuclear spins sitting on the lattice sites which are coupled to the electrons through the hyperfine interaction [108, 121–127, 129–132, 134, 161, 214].

#### D. Decoherence by an interacting nuclear spin bath

In this subsection, we discuss the effects of the lattice nuclear spins on the electron spin coherence. In the relevant III-V materials, all stable isotopes have non-zero nuclear spins. The nuclear magneton is about 3 orders of magnitude smaller than the electron Bohr magneton. A strong magnetic field of 10 T only results in a nuclear zeeman energy of  $\sim$  mK, much smaller than the experimentally achievable temperatures in cryostats ( $\sim 4$  K) or even in dilution refrigerators ( $\gtrsim 50$  mK) (see Fig. 1). Therefore, coupling to a thermalized nuclear spin bath will be an inevitable source of decoherence for quantum computation in III-V materials. As the longitudinal spin relaxation of the electron is found to be much slower than the transverse decoherence, we will focus on the pure dephasing of electron spins. In this Subsection, we set the  $z$ -direction along the direction of the external magnetic field.

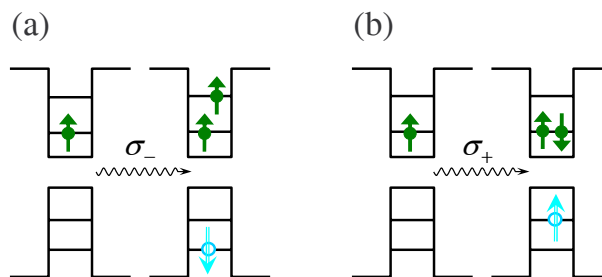


FIG. 5. Schematic illustration of the creation of trion states in a QD. The QD initially holds a single conduction band electron with spin up in the lowest state of the confinement potential. (a) By the Pauli exclusion principle, a  $\sigma_-$  circularly polarized light can create an additional exciton to a higher excited state of the QD. (b)  $\sigma_+$  polarized light can create the lowest energy trion state with two electrons forming a singlet and a hole in the spin up state.

### 1. Single electron in a mesoscopic bath of interacting nuclear spins

In III-V semiconductors, the electron spin is coupled to the lattice nuclear spin through the contact hyperfine interaction. The averaged magnitude of the coupling to a nucleus is inversely proportional to the total number  $N$  of nuclei in the QD. For QDs of all practical sizes ( $N \sim 10^5 - 10^7$ ), this hyperfine coupling is much stronger ( $\sim$  MHz) than the mutual interactions between the nuclear spins ( $\lesssim$  kHz). Therefore, a mesoscopic bath consisting of all nuclear spins within the QD (i.e. in direct contact with the single electron) can be identified (see Fig. 7) [130]. The coupling between the mesoscopic bath and nuclei outside the boundary can be neglected since such dynamics occurs in a much slower timescale as compared with the electron spin decoherence caused by the mesoscopic bath. The decoherence problem can then be solved by considering the quantum dynamics of the coupled mesoscopic system of electron and nuclear spins. The assumption that this mesoscopic system is well isolated from the background lattice has been confirmed in numerical studies where the boundary of the mesoscopic bath is systematically extended and the electron spin coherence shows fast convergence [130]. The nuclear spin bath is typically of a randomized configuration as schematically illustrated in Fig. 7 since the experimentally achievable temperature is always much higher than the nuclear Zeeman energy.

We briefly describe below the key ingredients for electron spin decoherence in the high field limit with details given in Appendix B. By the diagonal part of the electron-nuclear hyperfine interaction, the electron Zeeman energy is conditioned on the nuclear spin states (see Fig.8(a)). In a QD ensemble, the different nuclear spin configurations for each ensemble member lead to inhomogeneous broadening of the Overhauser field for the electron spin. This is the dominant cause of ensemble dephasing in the timescale of  $T_2^*$  which is inversely proportional to the inhomogeneous broadening. Nuclear-nuclear interactions become relevant due to the non-uniform hyperfine coupling strength between the electron and different nuclear spins. Pair-wise nuclear flip-flops can then lead to dynamical fluctuation of the nuclear Overhauser field (see Fig.8(b)). This is the cause of single electron spin decoherence in the nuclear environment which begins with a pure state (referred as *single-system dynamics* hereafter). Electron-nuclear coupling also has an off-diagonal part which tends to cause flip-flop between the electron and a nuclear spin. Because the electron Zeeman energy is much larger than the strength of the hyperfine interaction, the real process of electron nuclear flip-flop is suppressed [124, 127]. However, a second order process which consists of two virtual flips of the single electron ends up as a flip-flop between two nuclear spins (see Fig.8(c)). This effective nuclear interaction due to the single electron is designated as the *extrinsic* interaction [127, 130, 134], as opposed to the *intrinsic* nuclear interactions that exist in the semiconductor matrix, e.g. the dipole-dipole coupling and the indirect coupling mediated by virtual interband transitions via the hyperfine interaction [215–219].

The *extrinsic* nuclear interaction couples any two nuclear spins within the mesoscopic bath and is therefore infinitely-ranged, i.e., throughout the entire mesoscopic region. By contrast, the *intrinsic* nuclear interaction is finite-ranged. For near neighbors, the intrinsic one is much stronger than the extrinsic one for the field strength under consideration. In addition, for the *extrinsic* nuclear interaction, the magnitude is inversely proportional to the external magnetic field and the sign is conditioned on the electron spin states.

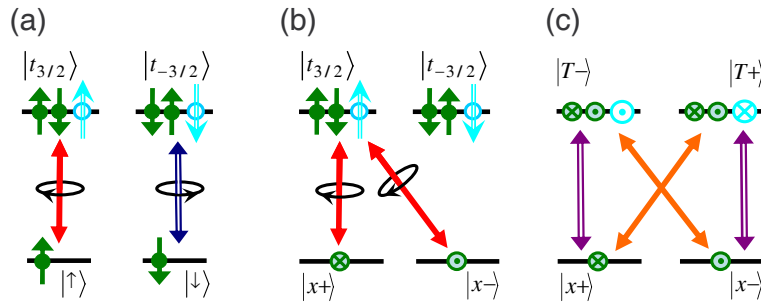


FIG. 6. Optical transition selection rules in a QD illustrated in various basis sets. (a) The basis is the eigenstates of  $\hat{J}_z$ . The solid two-headed arrow denotes  $\sigma_+$  polarized light and the hollow two-headed one  $\sigma_-$  polarized light. (b) The two electron spin states are transformed to the basis in the  $x$  direction:  $|x_{\pm}\rangle \equiv (|\uparrow\rangle \pm |\downarrow\rangle)/\sqrt{2}$ . The solid two-headed arrow denotes  $\sigma_+$  polarized light. (c) The two trion states are also transformed to the basis in the  $x$  direction:  $|T_{\pm}\rangle \equiv (|t_{\frac{3}{2}}\rangle \pm |t_{-\frac{3}{2}}\rangle)/\sqrt{2}$ . Here, the hollow two-headed arrow denotes  $X$ -polarized light and the solid one  $Y$ -polarized light.

## 2. Nuclear spin pair-flip excitations and pair correlation approximation

From the quantum mechanical picture of decoherence (see section II C), pure dephasing of a single quantum system is caused by the bifurcation of environmental evolution under the drive by different system states, or system-bath entanglement. Thus, the nuclear bath evolutions conditioned on different spin states of the electron are key to the solution of electron spin decoherence. The elementary excitations in the nuclear spin bath are pair-flip excitations as shown in Fig. 8(b) and Fig. 8(c). The flip-pairs are independent of each other if they are well separated. For a typical QD with  $N \sim 10^6$  nuclear spins, the number of pairs that can flip-flop in a random configuration is large. We have  $O(N)$  local flip-pairs whose dynamics are dominated by the finite range *intrinsic* nuclear interactions, and  $O(N^2)$  non-local flip-pairs whose dynamics are dominated by the infinite range *extrinsic* nuclear interactions. On the other hand, the number of pair-flips that can occur on the timescale of electron spin decoherence is negligibly small as compared with  $N$ . This is due to the slowness in the nuclear spin interacting dynamics. Thus, the probability of two pair-flips occurring in the neighborhood of each other is negligibly small and pair-flips as elementary excitations can be treated as independent of each other (see Appendix B for details). This approximation is further confirmed by the linked cluster expansion approach [129]. Independent pair-excitation approximation corresponds to keeping the lowest (2nd) order linked diagrams in the exponential factor. Higher order linked diagrams contain more nuclear interaction lines and are negligible in the relevant timescale because of the weakness of the nuclear interactions as compared with the electron-nuclear coupling. For long time evolution (such as for decoherence under pulse control) and for relatively small spin baths, higher order correlations would be important. The linked cluster expansion would be increasingly inefficient for calculating higher order correlations. The density matrix cluster expansion is an alternative method which requires no evaluation of higher order Feynman diagrams and is thus quite convenient [220]. For small spin baths, however, it has been shown that the cluster expansion may not converge to the exact results [221]. For a systematic and accurate account of the higher order correlations in spin baths in the qubit decoherence problem, a cluster-correlation expansion method has been developed [221, 222], which covers the valid ranges of all the methods mentioned above and in particular produces the exact results even for a relatively small bath where the standard cluster expansion fails. The cluster correlation expansion is based on the factorization of the bath dynamics into non-factorizable correlations of certain groups of bath spins. The lowest order of the cluster correlation expansion coincides with the independent pair excitation approximation. We also note that recently the higher order effects of the hyperfine interaction (beyond the pair-excitation considered here) has also been considered for a relatively weak external magnetic field while the pure dephasing condition is still satisfied [132, 214]

The evolution of independent pair-correlations can be described using a geometric representation. A pair-flip  $k$  can be mapped to a Bloch vector which precesses about a pseudo-field (see Fig. 9)

$$\mathbf{h}_k^\pm \equiv (\pm 2A_k + 2B_k, 0, \pm E_k), \quad (1)$$

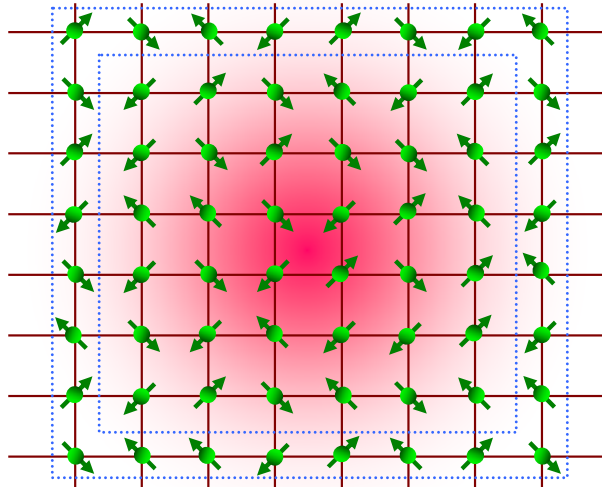


FIG. 7. Schematics of an electron (the shadow) and one layer of lattice nuclear spins in a QD. The two boxes in dotted lines indicate two possible choices of boundary of the mesoscopic nuclear spin bath, which are relatively arbitrary due to the interaction between nuclei within and without the boundary. When the hyperfine interaction dominates over the nuclear spin interaction, such arbitrariness has negligible effects on calculation of the electron spin decoherence as long as all the nuclei in direct contact with the electron spin have been enclosed.

where, for the electron spin state  $|\pm\rangle$ ,  $\pm A_k$  and  $B_k$  are the pair-flip transition amplitudes contributed by the extrinsic nuclear interaction and the intrinsic nuclear interaction, respectively, and  $\pm E_k$  is the energy cost of the pair-flip contributed by the hyperfine interaction (see Appendix B). At the initial time when the electron spin coherence is prepared (see the general formulation of decoherence process in Section II C), the Bloch vector for each pair-flip points in the pseudo  $+z$  direction. As the pseudo-field direction depends on the electron spin state  $|\pm\rangle$ , the pair evolution takes different trajectories conditioned on the electron spin state, and the distance  $\delta_k$  (i.e., distinguishability) between the two separated trajectories turns out to be a measure of the electron spin decoherence,

$$\mathcal{L}_{+,-}^s(t) \approx \prod_k e^{-\delta_k^2/2}. \quad (2)$$

where  $\mathcal{L}_{+,-}^s(t)$  is the ratio between the electron spin coherence at time  $t$  and at time 0 (see the general formulation of decoherence in section II C).  $\delta_k$  also quantifies the amount of entanglement between the electron spin and the  $k$ th flip-pair. The electron spin decoherence is thus the consequence of the entanglement with the pair-flip excitations in the interacting nuclear spin bath.

With single system dynamics solved for an arbitrary random configuration, ensemble dynamics is simply the statistical average of the single system dynamics with the nuclear bath initially in all possible configurations. As the number of flip-pairs is large ( $O(N)$  for local pairs and  $O(N^2)$  non-local pairs), the central limit theorem of statistics leads to a factorized form for ensemble spin coherence,

$$\mathcal{L}_{+,-}(t) = \mathcal{L}_{+,-}^s(t) \times \mathcal{L}_{+,-}^{(0)}(t), \quad (3)$$

where  $\mathcal{L}_{+,-}^s(t)$  is the single-system decoherence in a typical configuration of the nuclear bath, and

$$\mathcal{L}_{+,-}^{(0)}(t) = \sum_{\mathcal{J}} P_{\mathcal{J}} e^{-i\phi_{\mathcal{J}}(t)}, \quad (4)$$

where  $\phi_{\mathcal{J}}(t) = (\Omega_e + \mathcal{E}_{\mathcal{J}})t$  in free-induction decay, and the summation runs over all possible nuclear configurations  $\mathcal{J}$ .  $\Omega_e$  and  $\mathcal{E}_{\mathcal{J}}$  are the electron Zeeman energy resulting from the external magnetic field and from the Overhauser field, respectively, with the latter dependent on the nuclear configuration  $\mathcal{J}$ . The ensemble effect resides entirely in the factor  $\mathcal{L}_{+,-}^{(0)}(t)$ , which may be read as the inhomogeneous broadening of the Overhauser field  $\mathcal{E}_{\mathcal{J}}$  with a distribution function  $P_{\mathcal{J}}$ . The inhomogeneous broadening effect dominates the free-induction decay (FID) in the ensemble dynamics in the form of  $\mathcal{L}_{+,-}^{(0)}(t) = e^{-i\Omega_e t - (t/T_2^*)^2}$ , with the dephasing time  $T_2^* \sim \sqrt{N}\mathcal{A}^{-1} \sim 10$  ns as measured [112, 121, 124, 202, 205, 212, 223], where  $\mathcal{A} \sim \text{THz}$  is the hyperfine constant of the material.

A sequence of  $\pi$  pulses can be applied to the electron spin to eliminate the effects of the inhomogeneous broadening [110, 132, 180, 224]. In a general scenario where the electron spin is flipped at time  $\tau_1, \tau_2, \dots$ , and  $\tau_n$  respectively, we have

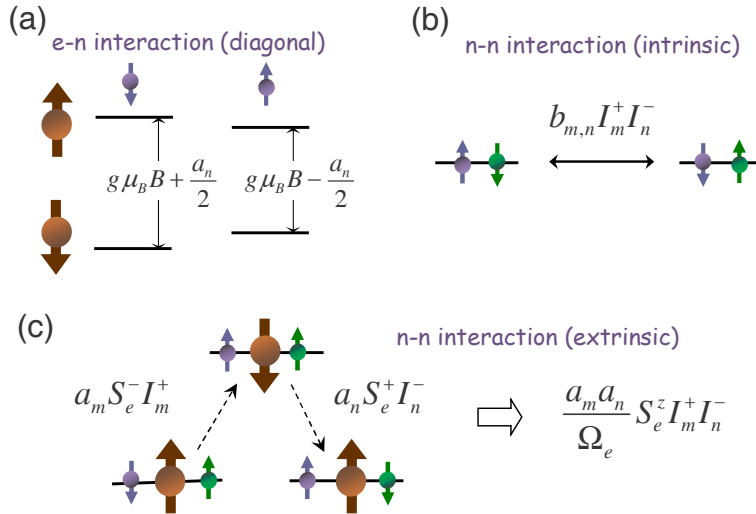


FIG. 8. Nuclear spin processes relevant for electron spin decoherence. (a) By the diagonal part of electron nuclear hyperfine interaction (which involves only the spin vector components along the field  $z$  direction), the electron Zeeman energy depends on the nuclear configuration. (b) Nuclear pair-wise flip-flop by the intrinsic nuclear interactions. (c) Nuclear pair-wise flip-flop mediated by two virtual flips of the electron spin, which results in an effective *extrinsic* nuclear interaction.  $\Omega_e$  is the electron Zeeman energy in the external magnetic field, and  $a_n$  is the hyperfine interaction strength between the electron and the  $n$ th nuclear spin.

$\phi_{\mathcal{J}}(t) = (\Omega_e + \mathcal{E}_{\mathcal{J}}) [\tau_1 - (\tau_2 - \tau_1) + \dots + (-1)^n (t - \tau_n)]$ . When  $\tau_1 - (\tau_2 - \tau_1) + \dots + (-1)^n (t - \tau_n) = 0$  is satisfied,  $\mathcal{L}_{+,-}^{(0)}(t) = 1$  and a spin echo is expected. The echo magnitude will be determined by the dynamical part  $\mathcal{L}_{+,-}^s(t)$ . Under the simplest scenario, a single  $\pi$ -pulse is applied at  $\tau$  and a spin echo is expected at  $t = 2\tau$ , known as Hahn echo [225]. The spin echo profile, i.e., the echo magnitude  $\mathcal{L}_{+,-}^s(2\tau)$  as a function of the echo delay time  $2\tau$ , reveals the dynamical processes that leads to decoherence.

It is worth noting that the factorized form of the ensemble spin coherence, Eq. (3), allows direct observation of single-system dynamics behavior  $\mathcal{L}_{+,-}^s(t)$  from a spatial ensemble measurement when dephasing by inhomogeneous broadening is removed at a general time  $t$ . For example, the mode locking experiment reported in [109, 211] opens up such possibilities as discussed in section II C, where the single spin  $T_2$  (defined here as the FID timescale of  $\mathcal{L}_{+,-}^s(t)$ ) has been extracted from the experimental data.

### 3. Timescales of single spin decoherence and ensemble spin echo decay

In FID, the conjugate Bloch vectors precess along opposite directions for non-local pairs ( $k \in K_A$ ), and symmetrically with respect to the pseudo  $y$ - $z$  plane for the near-neighbor pairs ( $k \in K_B$ ) [Fig. 9]. The decoherence can be readily grouped by the two different mechanisms as

$$\mathcal{L}_{+,-}^s \cong \prod_{k \in K_B} e^{-\frac{t}{2} E_k^2 B_k^2 \text{sinc}^4 \frac{h_k t}{2}} \prod_{k \in K_A} e^{-2t^2 A_k^2 \text{sinc}^2(h_k t)}, \quad (5)$$

where  $h_k = |\mathbf{h}_k^{\pm}|$ . We can see that the extrinsic hyperfine-mediated and the intrinsic couplings lead to the  $e^{-(t/T_{2,A})^2}$  and the  $e^{-(t/T_{2,B})^4}$  behavior respectively in time shorter than the inverse pair-flip energy cost (which corresponds to the width of the excitation spectrum),

$$T_{2,B} \approx b^{-1/2} \mathcal{A}^{-1/2} N^{1/4}; \quad T_{2,A} \approx \Omega_e \mathcal{A}^{-2} N, \quad (6)$$

where  $b$  is the typical value of near neighbor intrinsic nuclear coupling strength  $B_k$  (see Appendix B). The super-exponential decay behaviour of the spin coherence indicates the strong non-Markovian characteristic of the bath dynamics in the short time limit. In the long-time limit, the super-exponential decay will change to an exponential decay time first which indicates the onset of the Markovian dynamics [130, 131, 214]. The dynamics in the even longer time limit (which could occur, e.g., in a highly polarized spin bath), determined by the complex structure of the collective modes of the bath, is rather complicated, and power-law decays have been predicted [128, 214].

Fig. 10 shows the FID in single-system dynamics for a typical dot under various field strengths  $B_{\text{ext}}$ . The strong field dependence of  $T_2$  demonstrates the significance of the extrinsic hyperfine mediated nuclear coupling up to a strong field ( $\sim 10$  T). The short time  $e^{-t^2}$  behavior of decoherence by extrinsic nuclear interactions and the  $e^{-t^4}$  behavior by intrinsic nuclear interaction hold well within the relevant timescale for single spin FID. The field and dot-size dependence shown in Fig. 11, by the intrinsic and extrinsic mechanisms, agrees well with the simple form given in Eqns. (5) and (6). For a small QD or in a small magnetic field, the extrinsic nuclear interaction dominates, while the intrinsic nuclear interaction dominates otherwise. When

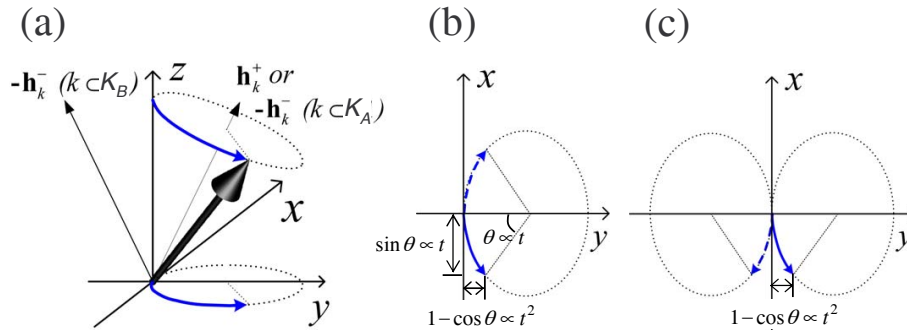


FIG. 9. A geometric picture for understanding the free-induction decay. (a) The evolution of pair-excitation illustrated by the rotation of a Bloch vector and the projected trajectory on the pseudo  $x$ - $y$  plane. Direction of the effective pseudo-field  $\mathbf{h}_k^{\pm}$  are indicated respectively for the set of non-local pairs  $K_A$  and the set of local pairs  $K_B$ . (b) The projection of the Bloch vector trajectories to the pseudo  $x$ - $y$  plane for pair-excitation driven by extrinsic nuclear interaction. The solid (dashed) line denotes the pair evolution conditioned on the electron spin state  $|+\rangle$  ( $|-\rangle$ ). As the rotation angle  $\theta \propto t$ , the distance between the conjugated vectors  $\delta_k \propto t$  at short time. (c) The projection of the Bloch vector trajectories to the pseudo  $x$ - $y$  plane for pair-excitations driven by intrinsic nuclear interactions. The distance between the conjugated vectors  $\delta_k \propto t^2$  at short time.

the two mechanisms are comparable, the single-system FID begins with  $e^{-t^2}$  behavior and may cross over towards  $e^{-t}$  decay as time increases (e.g., see the curve at  $B_{\text{ext}} = 12$  T in Fig. 10(b)). The timescale of single spin FID ranges from  $0.1 \mu\text{s}$  to  $10 \mu\text{s}$  depending on the dot size and external magnetic field, which agrees well with the experimental observation of  $3 \mu\text{s}$  by Greilich *et al.* [109].

In the spin echo scenario, as the electron spin is flipped by the  $\pi$ -pulse, the transition amplitude by extrinsic nuclear interaction  $A_k$  and the hyperfine energy cost  $E_k$  for each pair-flip will change sign after the pulse. Thus, the pair-excitations by the extrinsic hyperfine-mediated nuclear coupling will reverse their precession after the pulse and return to the origin at  $t = 2\tau$ , disentangling the electron spin and the pair excitations (see Fig. 12(a)). So the decoherence driven by the extrinsic hyperfine-mediated coupling is largely eliminated in the spin-echo configuration as shown by the calculation in Fig. 13 [125, 127]. For the pair-excitations driven by the intrinsic coupling, the conjugate Bloch vectors will switch their precession axes which also reverse the entanglement to some extent but no full recovery is obtained at the echo time (see Fig. 12(b)). Finally, the electron spin coherence at the echo time is derived as,

$$\mathcal{L}_{+,-}(2\tau) \cong \prod_{k \in K_B} e^{-2\tau^4 E_k^2 B_k^2 \text{sinc}^4(h_k^B \tau/2)}. \quad (7)$$

Similar to the analysis for single system FID, the spin echo signal begins with the short-time behavior as  $e^{-(2\tau/T_H^{\text{sh}})^4}$ .

The ensemble spin echo profile is numerically calculated and compared with the single-system FID for a typical QD in Fig. 13. While it has been a common practice to equal the spin echo decay time  $T_H$  to the single-system FID time  $T_2$  [123, 220], the two timescales can in fact be significantly different since the bath dynamics is modified by the pulse control of the electron spin. And the spin echo decay and the single-system FID follow different temporal behavior [Fig. 13]. The spin echo decay time of  $\mu\text{s}$  from calculation [127, 130] is in agreement with the Hahn echo measurements by Clark *et al* [181] for impurity spins in GaAs and by Petta *et al* [108] for gate-defined dot in GaAs.

### E. Coherence restoration and protection in the nuclear spin bath

Protection of the electron spin coherence by active physical control is desired which can result in a better physical qubit before the informatic approaches of quantum error correction may be implemented. This is indeed possible for single electron spins in interacting nuclear spin baths.

By a sequence of  $\pi$ -rotations of the electron spin, the ensemble dephasing by inhomogeneous broadening as well as decoherence by *extrinsically* driven nuclear pair-dynamics is efficiently removed at the classical spin echo time, as shown by the previous discussions. Nuclear pair-dynamics driven by the *intrinsic* interactions is also affected by such control as shown in Fig. 12(b): the two separated trajectories meet again sometime after the  $\pi$ -pulse. This intersection signals the disentanglement of the electron from the pair-excitation. Surprisingly, even though different pair-excitations have very different precession frequencies  $h_k$ , the trajectory separation  $\delta_k$  is eliminated for all local pairs in the leading order of  $B_k t$  at  $t = \sqrt{2}\tau$ . This leads to a recovery of the electron spin coherence as illustrated by numerical evaluation shown in Fig. 14. Remarkably, even when the electron spin is flipped after the coherence has completely vanished in single-system dynamics, the coherence may be well recovered at time  $\sqrt{2}\tau$  whereas no coherence is visible at the conventional spin echo time  $2\tau$  [134]. Thus, in this context, the decay of Hahn echo does not mean the irreversible lost of coherence due to the nuclear interacting dynamics. It is simply because the classical spin echo time for phase refocusing in ensemble does not respect the quantum behavior of the interacting dynamics in a mesoscopic

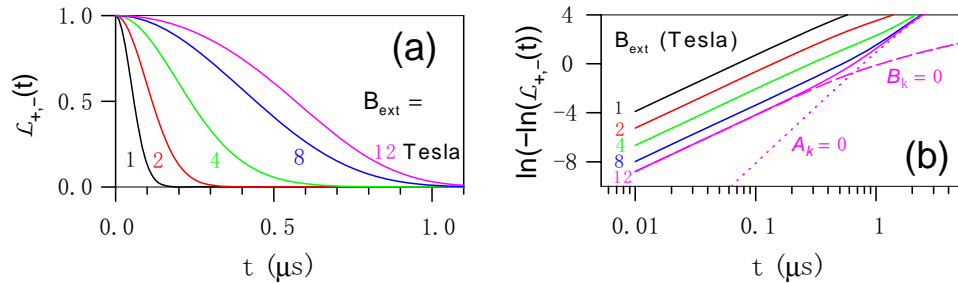


FIG. 10. (Extracted from Ref. [130]) (a) Electron spin coherence as functions of time for various field strengths. (b) The logarithm plot of (a), in which the curve for  $B_{\text{ext}} = 12$  tesla is compared with the contribution by the extrinsic nuclear interaction (the dashed line) and that by the intrinsic nuclear interaction (the dotted line), respectively. The size of the InAs dot is  $33 \times 33 \times 3 \text{ nm}^3$  and the nuclear-spin initial state  $|\mathcal{J}\rangle$  is randomly selected from an ensemble at temperature 1 K. The field strength is indicated by the numbers for each curve.

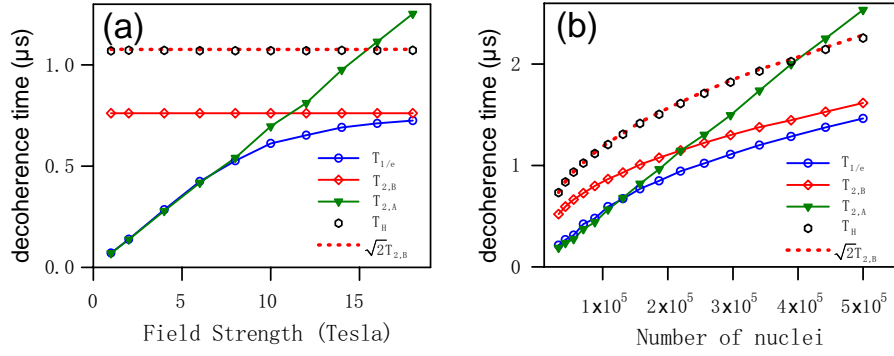


FIG. 11. (Extracted from Ref. [130]) (a) Field dependence of decoherence times with the inhomogeneous broadening effect excluded. The QD is the same as in figure 10 and the temperature is 1 K. (b) Dot-size dependence of decoherence times with the inhomogeneous broadening excluded. The QD size is varied with fixed width : depth : height ratio 33 : 33 : 6. The field strength is 10 tesla and the temperature is 1 K.  $T_{1/e}$  (solid line with circle symbols) – time for FID to  $1/e$  of its initial value,  $T_{2,A}$  (solid line with triangle symbols) – FID decoherence time resulting solely from extrinsic hyperfine-mediated pair-flips,  $T_{2,B}$  (solid line with diamond symbols) – FID decoherence time resulting solely from the intrinsic nuclear spin interaction, and  $T_H$  (circle symbols) – decay time of the Hahn echo signal. The  $\sqrt{2}T_{2,B}$  (dashed curve) is plotted to compare with the Hahn echo decay time.

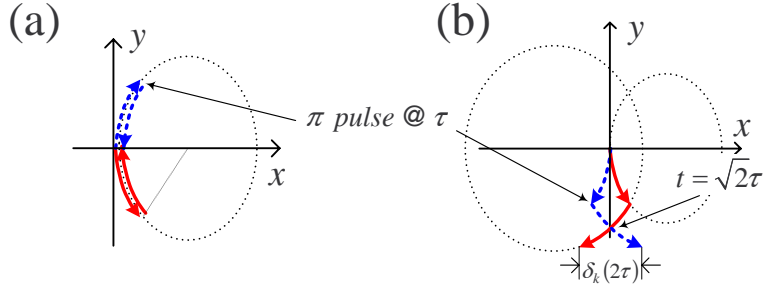


FIG. 12. (a) and (b) Evolution of the pair-excitations under the single-pulse control, driven by the extrinsic and intrinsic nuclear spin interactions, respectively. The red solid (blue dashed) trajectories denote the pair evolutions conditioned on the electron spin state  $|+\rangle$  ( $|-\rangle$ ).

bath. When the extrinsic nuclear interaction is significant, the  $\sqrt{2}\tau$  echo can also be weakened by the non-local pair-dynamics (see Fig. 14).

The  $\sqrt{2}\tau$  coherence echo is observable when the ensemble factor  $\mathcal{L}_{+,-}^{(0)}$  has a timescale longer or comparable to the single spin  $T_2$  time. This is possible with the narrowing of inhomogeneous distribution by nuclear state preparation [113–115, 143–151] (see Sec. II F). Furthermore, the unusual echo at  $\sqrt{2}\tau$  turns out to have a more general occurrence in other echo processes. Months after its first prediction [130, 134], such echo behavior is observed in NMR experiments in a  $^3\text{He}$  gas undergoing Brownian motion in a magnetic field gradient [226].

*Disentanglement from bath* could be the guiding principle for coherence protection with reduced overhead when the bath dynamics is more or less understood. In the present case of protecting electron spin from the nuclear spin bath, we need a pulse sequence to produce a time where the decoherence from all three sources can be removed. We give here a solution which is a two-pulse control. Fig. 14(c) shows that, after a second  $\pi$  pulse at  $3\tau$ , the two conjugated paths corresponding to the electron  $|\pm\rangle$  states, driven by the intrinsic nuclear interaction, cross again at  $4\tau$ , coinciding with the secondary spin echo time for the other two causes. The electron spin is thus disentangled from entire nuclear spin bath to the leading order at  $t = 4\tau$  (see numerical evaluation in Fig. 14(b)).

The power of concatenation design of pulse sequences has been shown in the context of dynamical decoupling of quantum systems from baths [133]. Similarly, the control of quantum system for disentanglement from the bath may be enhanced by concatenation design. We notice that the pair evolution with the two-pulse control of the electron spin can be constructed recursively from the free-induction evolution  $\hat{U}_0^\pm$ , by the concatenation,  $\hat{U}_l^\pm = \hat{U}_{l-1}^\mp \hat{U}_{l-1}^\pm$ ,  $l = 1, 2$  [130, 134]. The process can be extended by iteration to any level as shown in Fig. 15(c). Disentanglement from local and non-local pair-dynamics both occur at  $\tau_l \equiv 2^l\tau$  coinciding with the classic spin echo. The decoherence is reduced by an order of  $b^2\tau_l^2$  at  $\tau_l$  for each additional level of concatenation till saturation at the level  $l_0 \approx -\log_2(b\tau)$  [130]. Hence, the coherence echo magnitude scales with the echo delay

time according to  $\exp(-(\tau_l/T_l)^{2l+2})$  as shown in Fig. 15(b), suggesting that short-time decoherence can be arbitrarily suppressed with additional levels of concatenation. Numerical calculation further shows that a proper level of concatenation allows the protection of electron spin coherence by pulse sequences with interpulse interval as large as  $\sim \mu\text{s}$  (see Fig. 15(a)).

The concatenated control of the decoherence can also be optimized in terms of the number of pulses so that the control errors due to imperfections in the controlling pulses is minimized. The invention of the pulse sequences with the minimum possible number of pulses to suppress the short-time decoherence to a given order of the pulse delay time is due to Uhrig [139] in considering the qubit decoherence in a non-interacting boson bath. Later, the Uhrig decoherence control was conjectured [140] and proved [141] to be universal regardless of the bath Hamiltonian. The Uhrig pulse sequences may also be interlaced with the concatenated pulse sequences for control not only the pure dephasing but also the longitudinal spin relaxation [142, 227]. All these advances help to clear the obstacle of the qubit decoherence in solid environment.

### F. Summary: Quantum dot opportunity

The three-dimensional confinement in QDs leads to the quantized electronic and excitonic energy levels. As a consequence, a QD resembles an atom in terms of the discrete energy levels with long coherence times and well defined optical transition selection rules, although it is essentially a mesoscopic system. The atom-like electronic and optical properties have been well established by experiments in the past decades [199, 200, 205, 206, 213, 228–230], including the initial demonstration of quantum coherent control [231–236].

Experiments also showed that, for single electrons in QDs, spin polarization along an external magnetic field can be preserved for a sufficiently long time ( $T_1 \sim 20$  ms reported for InAs self-assembled dot [176]). A major concern has been the inevitable cause of transverse decoherence by the lattice nuclear spins in III-V materials. Due to the extremely small energy scales even in a strong magnetic field, the nuclear spin bath is of high entropy at experimentally achievable temperature. Ensemble dephasing time  $T_2^* \sim 1-10$  ns in different types of QDs [112, 202], spin echo decay time  $T_H$  in the order of  $\mu\text{s}$  in gate-defined QDs [108, 161] and for impurity spins in GaAs [181], and single spin dephasing time  $T_2 \sim 3 \mu\text{s}$  in self-assembled QDs [109] have been extracted from various experimental approaches, all in agreement with the theoretical analysis of nuclear spin baths [127, 130, 237]. As compared with the spin echo decay, FID in single-system dynamics is subject to the additional cause of decoherence from the extrinsic mechanism, which is dependent on the external magnetic field. In a moderate field of 1 tesla,  $T_2 \sim 100$  ns by theory [127, 130], is an order smaller than the spin echo decay time. Polarization of the nuclear spin bath can partially suppress this decoherence channel [128, 206, 238]. However, a substantial increase of electron spin coherence time would require a nuclear polarization over 99%, which can be extremely difficult. Current experimental capability on nuclear spin polarization in III-V QDs is in the order of 10-70% [112, 239–243].

For spin qubits used as quantum memory, dynamical decoupling schemes can be used to decouple system and environment for coherence protection [133, 244–247], which typically requires frequent manipulations of the spin qubits. As compared with these schemes designed to deal with a general environment, the available solution to the dynamics of the nuclear spin bath makes possible a different approach aiming at disentanglement of the system from the bath only (their decoupling is a sufficient but not necessary condition for disentanglement) [130, 134]. Numerical calculations on realistic QD systems show that designed sequence of  $\pi$ -pulses on the electron can efficiently preserve its spin coherence up to  $\sim 100 \mu\text{s}$  in both single-system and ensemble dynamics. As the interval between adjacent pulses can be as long as  $\mu\text{s}$ , this disentanglement approach not only substantially reduces the overhead but also avoids the problem of unwanted heating of the system from the frequent manipulations required by the dynamical decoupling schemes.

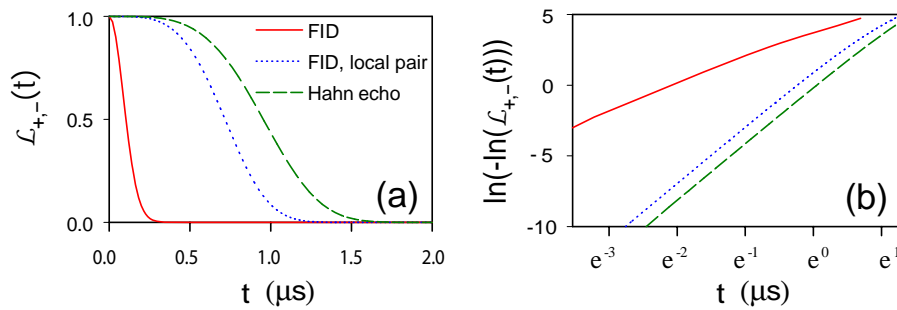


FIG. 13. (Extracted from Ref. [130]) (a) Comparison of the Hahn echo (dashed green line) and the FID (solid red line) signals. The FID signal is also shown with the extrinsic hyperfine-mediated pair-flips neglected (dotted blue line). (b) The logarithm plot of (a). The QD is as in figure 10, with  $B_{\text{ext}} = 2$  tesla.



In the quantum logic control of the spin qubit,  $T_2^*$  is the shortest timescale one encounters. Even with the ultra-fast optical manipulation timescale  $T_{\text{op}} \sim 10$  ps,  $T_2^* \sim 1 - 10$  ns from FID in a thermal nuclear spin bath is not sufficient to satisfy the current fault-tolerant threshold  $T_{\text{coh}}/T_{\text{op}} \sim 10^3 - 10^4$  [248–253]. Considering the efficiency of spin echoes in eliminating the dephasing by inhomogeneous broadening, the combination of the desired control action with these coherence protect operations could offer a promising route towards fault-tolerant quantum information processing. Efforts are being devoted towards the search of universal logic control strategies of coherence protected qubits [246].

An alternative approach is to pre-prepare the nuclear spin bath so that the nuclear field inhomogeneous broadening can be squeezed below its thermal value, as suggested by the various nuclear state preparation schemes [114, 143–145, 148–151]. The resultant enhancement on the  $T_2^*$  time can last for seconds or even longer as nuclear spin relaxation is extremely slow. For optically controllable electron spin in self-assembled dot, enhancement of  $T_2^*$  up to microsecond by nuclear state preparation has been achieved experimentally for a spin ensemble [146], and very recently for a single spin [147]. For electrically controllable spin qubits, enhancement of  $T_2^*$  of a coupled spin pair to microsecond was also reported in a double-dot configuration [115].

When the inhomogeneous broadening effect is suppressed (by spin echo or bath state preparation), dephasing by nuclear interacting dynamics is the limiting factor. Experiments [109] and theories [130] show that, in FID,  $T_2 \sim 0.1 - 10 \mu\text{s}$  for typical self-assembled QDs under a moderate magnetic field, which is sufficiently long to satisfy the fault-tolerant threshold. And the spin coherence time can be still elongated further by dynamical decoupling.

As an alternative, the heavy hole spin in a positively charged QD can also play the role of a qubit carrier. For the  $p$ -type hole bands, the contact hyperfine interaction vanishes and the hole spin is coupled to nuclear spins through the dipolar hyperfine interaction. Theoretical studies shows that the hole-nuclear hyperfine coupling strength is about one order weaker as compared with the electron-nuclear hyperfine coupling [80, 81]. Furthermore, unlike the isotropic electron-nuclear hyperfine interaction, the hole-nuclear coupling is strongly anisotropic. In the absence of heavy-light hole mixing, the hole-nuclear hyperfine interaction is Ising-like with coupling only between spin components along the growth direction [80, 81]. Finite hole-mixing effects can lead to the coupling between the hole and nuclear spin components perpendicular to the growth direction. In the absence of magnetic field, pump-probe and time-resolved photoluminescence experiments on  $p$ -doped self-assembled dot have revealed hole-spin ensemble dephasing time of 14 ns [80]. Most significantly, in a magnetic field perpendicular to the growth direction, coherent population trapping has been observed for a single  $p$ -doped dot which suggests a transverse dephasing time longer than 100 ns [254]. These experimental findings are consistent with the theoretical studies of the hole-nuclear hyperfine coupling [80, 81]. Since the  $p$ -doped QDs have similar energy level-schemes and transition selection rules to the  $n$ -doped ones, hole spins in QDs may be manipulated using optical schemes similar to those for electron spins. For example, high fidelity hole spin initialization has already been demonstrated [255], using similar optical pumping schemes previously adopted for electron spin initialization [256, 257].

Another kind of solid-state electron spin systems which are under exciting development is NV centers in diamond. An NV center in diamond is a defect with a C-C bond substituted with a negatively charged N atom, which has a spin-1 at the ground state. NV center spins are a promising candidate for quantum computing for the following virtues [258]: First, as deep-level

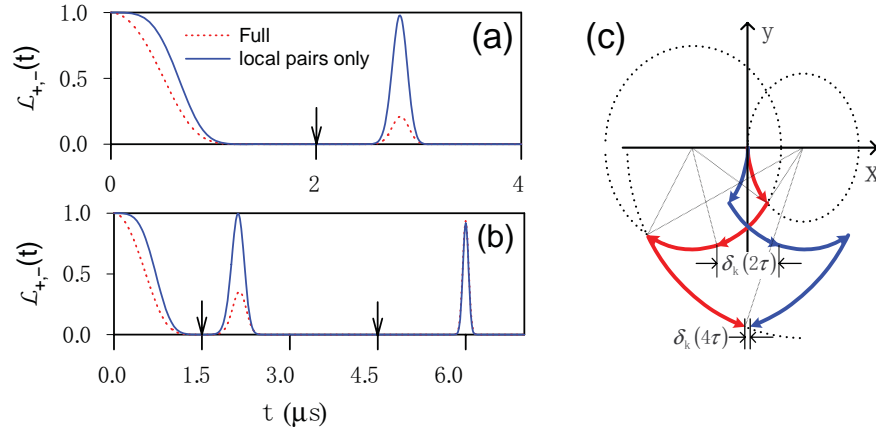


FIG. 14. (Extracted from Refs. [134] and [130]). (a) The electron spin coherence under the control of a short  $\pi$ -pulse applied at  $\tau = 2 \mu\text{s}$  (when the FID signal has vanished), the recoherence at  $\sqrt{2}\tau$  is pronounced while no signal survives at the echo-time  $2\tau$ . (b) The electron spin coherence under the control of a Carr-Purcell pulse sequence. The arrows indicate positions of the  $\pi$  pulses. The solid blue (dotted red) lines are calculated with (without) including the extrinsic hyperfine-mediated pair-flips. The QD is the same as in figure 10 with  $B_{\text{ext}} = 10$  tesla. Inhomogeneous broadening is excluded. (c) The projection of the Bloch vector trajectories to the pseudo  $x$ - $y$  plane for intrinsically driven pair-excitations under the 2-pulse Carr-Purcell control.

defects, they have chemical and thermal stability; Second, the spin-orbit coupling in the light C and N atoms is very weak, so the spin decoherence by phonon scattering is negligible even at room temperature [89, 94]; Third, the natural abundance of isotopes with non-zero spin (C-13) is only about 1% and also the hyperfine interaction between the center spins and the bath nuclear spins is mostly dipolar which is highly anisotropic and decays rapidly with the distance. Thus the electron spin decoherence by the hyperfine coupling is very slow (coherence time  $> 50$  microseconds in natural samples [89] and  $\gtrsim$  milliseconds in C-13 depleted diamond [259]); Fourth, the material is optically transparent and the centers are optically active, feasible for optical access [88, 92, 93, 95, 204] and coupling with cavities or waveguides [260–263]. The proposal of quantum computing with diamond defects [87] exploded to a hot research field after the experimental demonstration of electron spin Rabi oscillation [90] and two-qubit gates for coupled electron and nuclear spins [91] in single NV centers. Awchalom group demonstrated coherent coupling between a “bright” NV center and a “dark” nitrogen center [93]. Gaebel *et al* realized strong coupling between an NV spin and a nitrogen spin at room temperature [94]. Lukin and colleagues showed spin echo of an NV spin and observed coherent coupling between the electron spin and nuclear spins nearby [97]. In 2007, Lukin group managed to isolate and control an NV spin and a strongly coupled nuclear spin [98]. In 2008, Neumann *et al* claimed multipartite entanglement among C-13 nuclear spin near an NV center [264]. Most recently, Lukin group and Wrachtrup group independently demonstrated readout of an NV qubit improved by repetitive retrieval of proximal nuclear spin ancillae [265, 266].

In the remaining part of this review, we will discuss the optical manipulation schemes for QD electron spin qubits, and we expect that most of them shall be applicable for hole spins and NV centers as well, except the distinctive hyperfine effects on the optical processes of the hole spins and of the NV center with its proximity nuclear spin.

### III. PHYSICAL STRUCTURE

#### A. Local nodes

A local node is composed of a few QDs. The specific QD systems of interest include  $\text{In}_{1-x}\text{Ga}_x\text{As}$  self-assembled QDs and GaAs fluctuation QDs. These III-V compound semiconductors have direct band-gaps and thus are suitable for optical control. A fluctuation QD is formed by width fluctuation in a narrow quantum well grown with certain procedure (such as interruption for introducing interface roughness). This kind of dots has lateral confinement size ( $\gtrsim 10$  nm) much larger than the growth direction size ( $\lesssim 5$  nm) and the lateral confinement potential is shallow (usually in the order of a few meV). Thus a fluctuation QD would not host many bound electronic states and often just one, which is still subject to ionization due to thermal or optical excitation. Nonetheless, the loose lateral confinement makes optical transitions in a fluctuation QD well characterized by selection rules resulting from conservation of angular momentum with respect to the growth direction. The large size of fluctuation QDs also makes the dipole moment for inter-band transitions to be large and therefore enhances the optical coupling which is useful for strong coupling in cavity quantum electrodynamics (QED) and has been utilized in demonstrating optical control of excitonic qubits [231, 232]. A self-assembled QD is formed by the spontaneous nucleation of one material (such as InAs) on the surface of a substrate (such as GaAs) which has slightly different lattice constant. Such a QD is relatively small (with lateral size  $\sim 10$  nm)

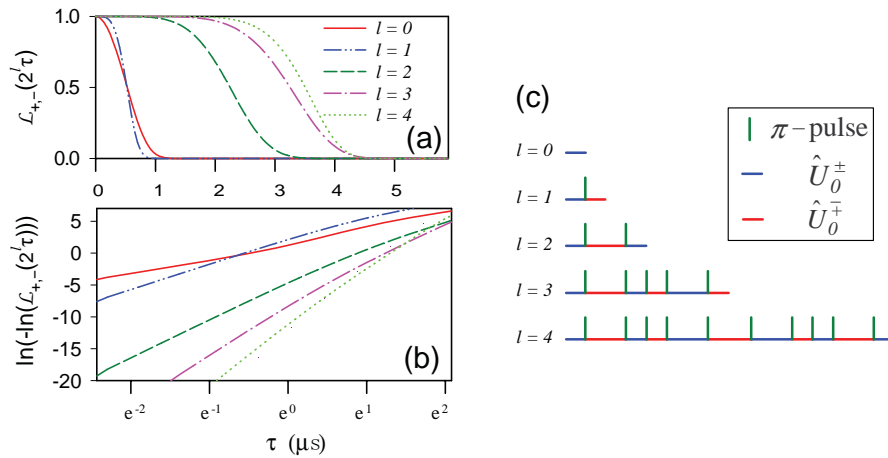


FIG. 15. (Extracted from Ref. [130]) (a) The electron spin coherence under the  $l$ th order concatenation control,  $l = 0, \dots, 4$ , as functions of the pulse delay time  $\tau$ . (b) The logarithm plot of (a). The QD is the same as in Fig. 10 with  $B_{\text{ext}} = 10$  tesla. Ensemble average is taken at  $T = 1$  K. (c) Concatenated sequences of  $\pi$ -pulses flipping the electron spin, represented by vertical bars.

and deep confinement potential (in the order of hundreds of meV) which is defined by the offset between the band-edge of the QD material and that of the substrate. As a result, a self-assembled QD could host quite a few stable bound states, providing extra flexibility for quantum control. There is no obvious reason to exclude other types of QDs such as those formed in II-VI materials and II-VI nanocrystals [267], though they are less comprehensively studied in experiments mostly because of technical difficulties such as the requirement of UV lasers, strong charge fluctuation around QD surfaces due to low material mobility, and complex defects and impurity centers. The optical control schemes discussed in this review can be applied to the NV centers in diamond with some modifications.

In classical electronic computers, the physical layout of logic circuits is planarly extended. It is not hard to expect the planar layout to be used in a quantum computer. In self-assembling growth processes, vertically stacked QDs may be formed to several layers [268]. The vertical structure, however, is not extendable and furthermore, limits the accessibility by optical pulses. Planar distribution is naturally formed both in self-assembled QDs and in fluctuation QDs. Formation of QD molecules or arrays due to lateral coupling is possible [195, 269]. With proper growth art, clusters of QDs with certain patterns may be fabricated [270–272]. Remarkably, NV centers in diamond may be implanted by ion beams with position precision in the order of 10 nm [158, 159]. Having such technology within the scope of our consideration, we assume a local node in a quantum computer composed of a few (usually fewer than 10) QDs (or impurities), laterally distributed and coupled. The control of electron spins in QDs is to be designed after a local node consisting a cluster of QDs has been fabricated and characterized. In this sense, the specific layout of a local node, which could be a ring, a line, or any other graphs naturally formed, does not make essential difference. But a linearly displaced array would be preferable for its simplicity in coupling and practicality in manufacturing.

A scalable physical structure of a QD-based quantum computer should have the following features: (1) the QDs are placed in an extendable layout; (2) the QDs are connected so that electron spins can be coupled to a common photonic or electronic state; and (3) the QDs are individually accessible so that the electron spins are individually controlled. On the one hand, the spatial resolution of near-field optical devices is still not high enough to identify each QD in a cluster. On the other hand, within the limit of current technologies, it is impossible to control the growth of QDs so that they are almost identical. Different sizes and shapes of the QDs would make the exciton transition energies in different QDs different. In this way, the near-field optics and the fingerprint transition frequencies of different QDs may be combined together to individually address each dot or to selectively couple a pair of them. The coupling between spins in general is mediated by virtual tunneling between different QDs which may be activated by virtual optical excitation of excitons in the presence of extra electrons which bear the spins (More details will be discussed in later sections). For NV centers in diamond, such mechanisms are not yet considered, but other schemes may be applicable such as coupling through virtual excitation of cavity modes [64], or hyperfine interaction with nuclear spin baths [100].

We show an example in Figure 16 a working module of 7 qubits in a linearly displaced array of QDs. With the QDs of the size around 50 nm and about 20 nm apart, the 7 dots may be addressed with two micro-lenses attached to, e.g., optical fibers, with resolution of about  $0.2 \mu\text{m}$ . The QDs addressed by the same optical fiber are distinguished by their signature transition frequencies. Using optical pulses with different frequencies and polarizations, each dot and each adjacent dot pair may be (virtually) excited and various single- and two-qubit gates and initialization could be realized, as illustrated in Fig. 17. To realize arbitrary single-spin rotation, a magnetic field is applied along the in-plane-direction (denoted as the  $z$ -direction).

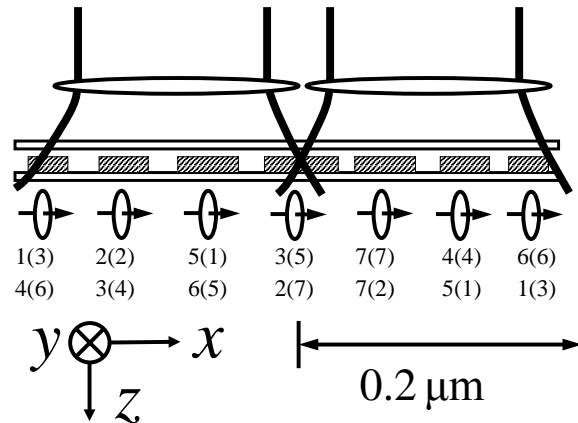


FIG. 16. The physical structure of a local node consisting of seven electron spins in a QD cluster. Each QD is identified by a near-field micro-lens as well as by its characteristic transition energies. The numbers are used to label the qubits for factorizing 15 with the seed number  $a = 4$  (top row) and  $a = 13$  (bottom row), respectively. The numbers in the parentheses label the qubits at the end of computation (see Sec. VIII A for details).

We assume that only neighboring QDs are coupled, for simplicity. Coupling between spins in farther separated dots is to be accomplished by recursively using the nearest neighbor coupling, which increases the number of gates by an amount in the order of the number of dots between the two ends. To minimize the number of operations between separated qubits, the quantum algorithms are compiled by using optimum labeling of the qubits. Taking into account the size of the micro-photon structures (including cavities and waveguides connecting local nodes), a working module of about 10 QDs could occupy an area of about  $10\ \mu\text{m}\times 10\ \mu\text{m}$ , so a quantum chip of size  $10\ \text{cm}\times 10\ \text{cm}$  can in theory accommodate  $10^8$  qubits.

For the purpose of addressing and optical control of a single QD, several near-field optics technologies have been available, such as micro-optical masking and micro-fiber optics [273]. For a cluster of QDs to function under optical control, however, there are still non-trivial technical challenges, including at least fabrication of QD clusters with energy levels and inter-dot couplings falling in the desired parameter ranges, assembling of micro-lenses on the surface of QD clusters, and designing, shaping, and controlling complex laser pulses. The micro-lens technology has been widely used in the digital imaging industry (micro-lenses of similar sizes are routinely used to focus light into individual pixels in commercial digital cameras).

## B. Distributed structure

The electron spin qubits are distinguished by the different optical transition frequencies of the host QDs. Thus, the dot density shall be rather dilute so that each laser spot contains only a small number of QDs ( $\sim O(10)$ , considering the typical inhomogeneous broadening of the excitonic linewidth of  $\sim 10 - 100\ \text{meV}$ , and the requirement of  $\sim 0.1 - 1\ \text{meV}$  frequency separation for optically addressing individual QDs. Therefore, the optical approach predetermines that a local node can only have a limited number of qubits. In order to scale up, a distributed architecture could be a solution [2, 274]. In such structures, clusters of QD electron spin qubits form quantum nodes where logical operations can be performed locally, and connections between clusters are through quantum channels in which the flying qubits take information from one place to another.

The single photon wavepacket is an ideal candidate as the carrier of flying qubits, being widely used in quantum cryptography [275] and linear optics quantum computation [276]. The qubit can be encoded in the photon-number subspace [277] or polarization subspace [276]. While single photon propagation in free space is un-channeled and inefficient, optical waveguides in semiconductors and optical fibers provide directional channels.

In the distributed architecture of optically controlled spin quantum computation, flying photons in waveguides/fibers are responsible for integrating the distributed stationary spin clusters into a globally functioning quantum computer. This requires quantum interfacing between single electron spins in QDs and single photons in waveguide. As mentioned in Sec. II, QD electron spins interact with optical fields via the intermediate states of trions. Such interface at the single photon level requires strong light-matter interactions. As a QD has a fixed optical transition dipole moment which is limited by its size, one way to have such strong light-matter interaction is to confine photons in optical cavity structures with small volumes.

Micro-cavities can be realized in a number of ways in semiconductor structures. We list below the essential properties of a few representative ones:

1. *Microdisk* – See Figs. 18 and 19 for schematic illustrations of the geometry. Light is confined by total internal reflection in the inner wall and the confined modes are known as the whispering gallery modes. Quality factor  $Q \sim O(10^4)$  in III-V materials and  $\sim O(10^5)$  in polymer; mode volume  $V \sim 6(\lambda_0/n)^3$  where  $n$  is the refractive index of the material and  $\lambda_0$  the wavelength of cavity mode [278]. Strong coupling regime for GaAs fluctuation QD embedded in micro-disk structure

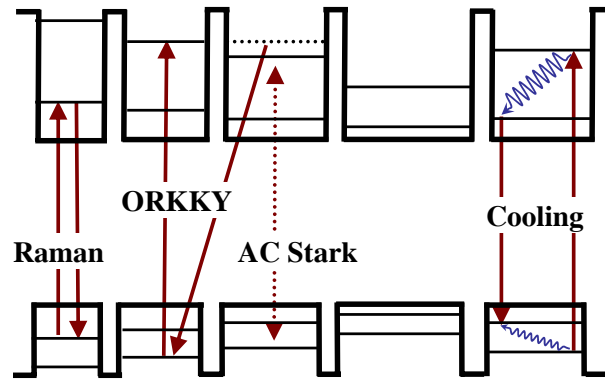


FIG. 17. The energy diagram of various optical processes for quantum gates and initialization: “Raman” for single-spin control or optical pumping and measurement of a single spin, “ORKKY” for two-spin control, “AC Stark” for transient shift of energy levels to realize selective resonance, and “Cooling” for initialization of spins via phonon bath (phonon emission as wavy lines).

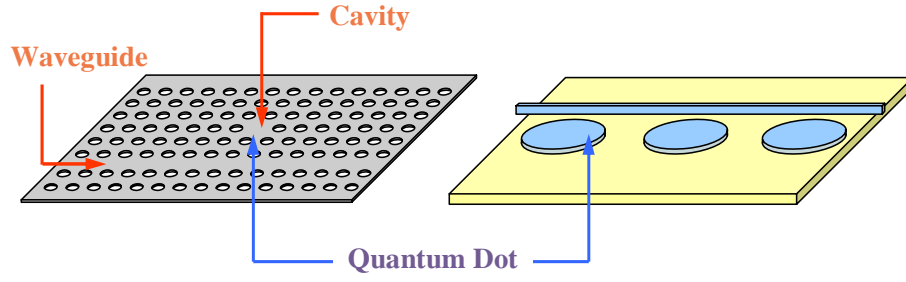


FIG. 18. Left: coupled cavity and waveguide structure formed by point and line defects in 2D photonic bandgap crystals. Right: waveguide coupled micro-disk cavity etched on chip. Layers of QDs can be embedded in the matrix slab where the cavities are formed.

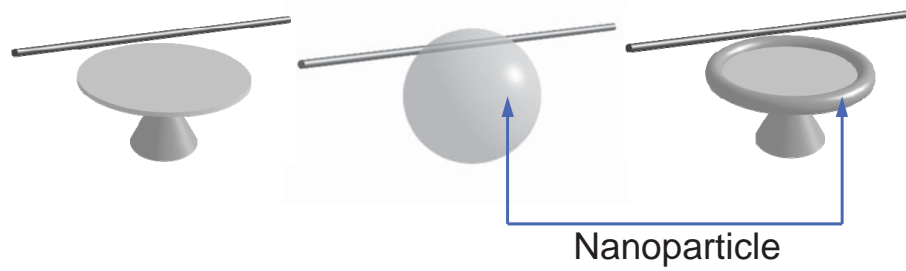


FIG. 19. Left: fiber coupled micro-disc cavity. Middle: fiber coupled micro-sphere cavity. Right: fiber coupled micro-toroid cavity. Semiconductor nanoparticles, e.g. diamond with NV centers, can be adsorbed onto the latter two types of cavities.

similar to the illustration in Fig. 19 has been achieved [279]. Because of the large dipole moment of the fluctuation dot, the measured cavity-dot coupling constant  $g_{\text{cav}} \sim 0.2$  meV signifies strong coupling.

2. *Defect cavity in 2D Photonic Crystal* – Two dimensional photonic bandgap crystals are an ideal structure to form a cavity resonator [280, 281]. Propagation of light in the plane has a forbidden bandgap for carefully designed periodical arrays of air-holes drilled on the 2-D slab. As shown in Fig. 18, by forming a point defect in the 2D array of air holes, light can be almost perfectly confined in the plane of the slab if its frequency lies in the forbidden bandgap. The vertical confinement, achieved by total internal reflection at the semiconductor-air interfaces, is imperfect, in that light with small in-plane wavevectors can leak out of the top and bottom. Vertical leakage can be greatly suppressed by proper engineering of the defect [282, 283].  $Q \sim 6 \times 10^5$  and  $V \sim 1.2(\lambda_0/n)^3 \sim 0.072 \mu\text{m}^3$  have been achieved [282, 283]. Theoretical analysis shows that  $Q$ -factors greater than  $2 \times 10^7$  are realizable by optimizing the structure [283]. The matrix of a 2D photonic crystal can be either silicon or III-V compounds [284]. Strong coupling with single self-assembled InAs QDs has been demonstrated [284, 285], where  $g_{\text{cav}} \sim 0.1$  meV.
3. *Micro-pillar* – Light is vertically confined by distributed Bragg reflector mirrors and horizontally by total internal reflection.  $Q \sim 10^4$  and  $V \sim \mu\text{m}^3$  have been achieved [286, 287]. Strong coupling with single self-assembled InAs QDs has been demonstrated [286, 288], where  $g_{\text{cav}} \sim 0.1$  meV.
4. *Epitaxial cavity* – Vertical confinement is by distributed Bragg reflector mirrors and horizontal confinement by thickness variations, similar to the confinement principle of the fluctuation QD [289].  $Q = 3 \times 10^4$ ,  $V \sim \mu\text{m}^3$  have been achieved [289].
5. *Silicon microsphere* – WGMs are confined by total internal reflection.  $Q$  exceeding  $10^8$  and  $V \sim 10^3 \mu\text{m}^3$  have been achieved [290, 291]. Nanocrystals (such as CdSe nanocrystals [292] and diamond nano-crystals with NV centers [260]) deposited on the surface are usually used for coupling with the cavity photons.
6. *Microtoroid* – See Fig. 19 for an illustration of the geometry. WGMs are confined by total internal reflection.  $Q \sim 10^8$  is achieved with principal diameter  $D \sim 100 \mu\text{m}$  and the minor diameter  $d \sim \mu\text{m}$  [293]. Theoretical analysis shows the possibility of realizing micro-toroid with  $Q$  exceeding  $10^8$  and  $V \sim O(10) \mu\text{m}^3$  [294].

The high quality factor allows photons to be confined for a sufficiently long time inside a cavity and the small mode volume makes possible a large intra-cavity electromagnetic field from a single photon. Both features are critical for the strong dot-cavity coupling, defined by the criteria that a single cavity photon can induce  $\geq 2\pi$  Rabi oscillation of an excitonic transition in a single dot within the lifetimes of the cavity photon and the exciton. Strong coupling has already been realized in several cavity-dot systems [260, 279, 284–286, 288, 292]. With micro-cavity being a playground for strong coupling of a single photon with a single dot, the interface between a flying photon qubit in a waveguide and a stationary spin qubit in a QD can be achieved by evanescent coupling between an optical waveguide/fiber and a micro-cavity containing the QD (see Figs. 18 and 19). A single photon wavepacket propagating in the waveguide can excite a cavity photon which then significantly influences the QD spin dynamics, e.g. through the optical Raman process via the trion states (see Sec. II B) [119]. In addition to the exciting advances in improving the  $Q$ -factor and reducing the mode volume of semiconductor micro-cavities for strong coupling, many other key ingredients towards the construction and control of such a dot-cavity-waveguide coupled structure have been progressively achieved in laboratories. These include the high-efficiency coupling between micro-cavities and optical waveguides/fibers [295–301], precise control of intra-cavity location of QDs [285, 302, 303], fine-tuning of cavity modes into resonance with a given QD transition [285, 302, 304–306], electrically controllable charging of intra-cavity QDs [307], and coherent resonant driving of QD excitonic transitions inside a cavity by an external laser [230, 308].

With the possibility of spin-photon interfacing in dot-cavity-waveguide structures, we are able to outline the construction of a distributed architecture for scalable quantum information processing in an integrated semiconductor platform composed of QDs, optical micro-cavities, and optical waveguides/fibers (see Fig. 20) [309]. In this network structure, a local node contains a limited number of charged QDs, distinguishable by their optical frequencies. The stationary spin qubits form a basis for the quantum memory and quantum logic modules. Optical waveguides/fibers connect distributed nodes with single photon wavepackets as the flying qubits. Micro-cavities offer the playground for the strong interaction between the two types of qubits. Control of a local node will be the focus of Sec. IV. Control of the interfacing between single spins and single photons will be the focus of section VII. With the recent progresses in coupling NV centers in diamond with photons in cavities and waveguides [260–263], similar distributed quantum computing with NV centers is also foreseeable.

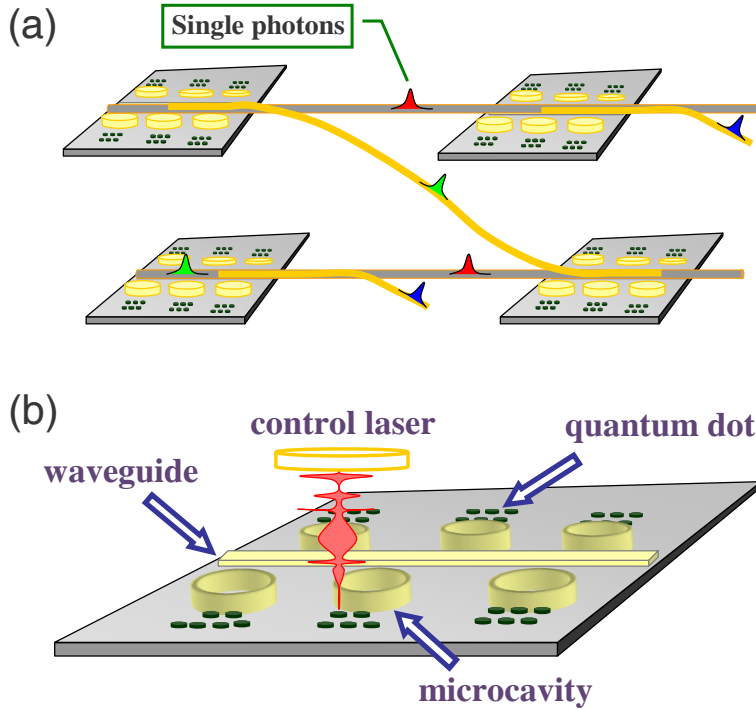


FIG. 20. Distributed quantum information processing in integrated semiconductor structures. (a) Schematics of a distributed quantum computer where communications between computation modules are mediated by single photons in optical waveguides/fibers. (b) The spin-based computation modules on a chip, controlled by ultrafast optics.

#### IV. ONE- AND TWO-QUBIT OPERATIONS

It has been established that universal quantum computation can be accomplished by a set of single-qubit gates and one kind of entanglement gates such as CNOT,  $\sqrt{\text{SWAP}}$ , or controlled phase-shift gate [172, 183, 184]. While there are many alternatives, we follow a more traditional and scalable approach of designing a system which has negligible interaction between qubits when the system is idling, and creating transient interaction between two qubits during the operation.

General speaking, there are two strategies for controlling electron spins in QDs, namely, the direct and the indirect control. As the terminology suggests, the direct control manipulates the electron spins directly which may be realized by rotation of a single spin with an AC magnetic field from, e.g., a microwave or a pulse DC magnetic field [66, 88, 90, 97, 98, 161], and by coupling two spins via exchange interaction mediated by virtual tunneling between QDs switched by, e.g., gate voltages [63, 65, 82]. The direct control schemes are more applicable to electrically defined QD systems made possible by the feasibility of in-situ electrical gates. There is no fundamental obstacle to integrate electrical gates to self-assembled or fluctuation QD systems and to apply the direct control of electron spins. But the much smaller size of these QDs as compared with the splitting-gate defined ones and the much stronger confinement (or much less tunneling probability) cause non-trivial technical problems. The indirect control schemes are based on indirect coupling between electron spin states mediated by virtual excitation of auxiliary energy levels which are modified by (or conditioned on) the states of the spins [64, 68–79, 181, 182]. Usually, such intermediate states are excitons which may be excited by optical pulses. The optical control of electron spins is limited to direct-gap semiconductors but otherwise have a great deal of merits particularly due to the energy scale cascade. As bandgaps in semiconductors are usually larger by orders of magnitude than the electron spin Zeeman energy, the control of the electron spins could be made much faster by using excitation cross the large bandgap. For comparison, electrical control of spins on the nanosecond scale is already the state-of-the-art technique [108, 161], while optical manipulation of electron spins can be completed on the picosecond timescale [78, 79, 181, 182].

In essence, all schemes of optical control of the electron spin states [64, 68–76, 173] are realized by the Raman processes where the virtual excitation of excitons plays the central role. In one-qubit operations, the intermediate states are excitons with one excess electron, i.e., the trion states [68, 72, 76]. In two-qubit operations [64, 68–71, 73–76, 173], the intermediate states are excitons with two excess electrons. The effective exchange interaction between two spins may be induced by the virtual excitation of one exciton tunneling back and forth between two dots, which is similar to the RKKY process and is dubbed optical RKKY interaction to indicate the role of the optical excitation [73–75]. Alternatively, even if there is no tunneling between QDs, the interplay between Coulomb interaction and the spin blocking effect would induce effective interaction between two separated spins when two excitons are (virtually) excited in two dots [68–71, 173]. The spin interaction may also be mediated by virtual photon exchange during the virtual excitation of excitons [64, 76].

More details about the optical control of one-spin and two-spin gates follow. Since the essential physics of various optical control schemes is similar, we will focus on two specific examples, namely, Raman control of single spins, and optical RKKY control of two spins, as an illustration of the physics and the operation conditions.

##### A. Single-spin rotation by Raman process

Arbitrary single-spin rotation can be realized via adiabatic Raman processes mediated by trion states [72, 169]. We will illustrate the basic idea of such a scheme and discuss the non-adiabatic generalization and certain limits of the method. It is worth pointing out that the stimulated Raman adiabatic passage (STIRAP) [310] involving only dark states could not realize an arbitrary rotation but only a spin flip from a known initial state. The adiabatic Raman processes in arbitrary spin rotation involves both dark states and bright states [72].

The control of an electron spin relies critically on the spin states of the excited excitons which are determined by the optical selection rules in the semiconductor QDs. In the III-V semiconductors of zinc-blende crystal structure, the selection rules of optical excitations at the band edge are well defined by the angular momentum conservation in terms of the electron spin in the conduction band and the hole spin in the valence band, which have angular momentum  $s = 1/2$  and  $J = 3/2$ , respectively. In QDs of large lateral sizes and strong confinement in the growth direction (defined as  $z$ -axis), the hole states will be split into two sets of degenerate states, with spin states  $J_z = \pm 3/2$  and  $\pm 1/2$ , respectively, designated as heavy and light holes, respectively, according to their effective mass along the  $z$ -axis. When the lateral sizes of the QD are much larger than the confinement size in the growth direction, the mixing of different angular momentum states by the lateral confinement is small [81]. Thus the optical excitation is restricted by the angular momentum conservation along the  $z$ -axis. Now if the controlling optical pulses are applied normal to the sample surface, the conservation of the angular momentum about the growth direction makes it impossible to flip the electron spin along  $z$ -axis and thus impossible to complete an arbitrary quantum operation, unless the light beam is incident with an angle [311] or the symmetry is broken by a magnetic field with a non-zero in-plane component. Since in the near-field optics, the incident light is usually normal to the surface, we need a static in-plane magnetic field applied (whose direction is defined as  $x$ -axis). Under the strong magnetic field, the electron spin states are split into two Zeeman levels  $|+x\rangle$  and  $|-x\rangle$  with energy  $\pm\omega_c/2$ , respectively. We use these two states as the basis  $|0\rangle$  and  $|1\rangle$  of a qubit. The Zeeman splitting  $\omega_c$  is in the order

of 0.1~1 meV under a magnetic field of a few Tesla. In GaAs fluctuation QDs, the hole states are still near-degenerate, since the large heavy-light hole splitting ( $\Delta_{hl}$  is tens of meV) makes the hole spin splitting  $\sim \omega_c^3/\Delta_{hl}^2$  negligible even under a field as strong as a few Tesla, so the hole states can still be defined by the magnetic quantum number  $J_z$  as  $|\pm 3/2\rangle$ , which will also be denoted by hollow arrows as  $|\downarrow\rangle$  and  $|\uparrow\rangle$ , respectively. In this case, the optical transitions can be separated by the selection rules even when the energy difference due to the electron spin splitting is relatively small. Note that the near-degeneracy of the two trion states is not a necessary condition in the schemes of single spin rotation to be discussed below. Actually, in self-assembled dots where hole states can be split by an in-plane magnetic field due to the large heavy-light hole mixing, the splitting between the trion states can be exploited to separate desired transitions from unwanted ones by energy difference.

To illustrate the essential physics underlying the control process, we ignore the high-lying excited states and model the system by four states consisting of the two split electron spin states and two trion states  $|t_{\pm}\rangle$  which are formed by two electrons in the singlet state  $|\uparrow\downarrow\rangle$  and one hole in the spin state  $|\uparrow\rangle$  or  $|\downarrow\rangle$ , respectively. According to the angular momentum conservation about the  $z$ -axis, the selection rules of the optical excitation, as depicted in Fig. 21 (a), is such that a light with circular polarization  $\sigma^{\pm}$  will induce the transition from the electron states  $|+1/2\rangle$  or  $|-1/2\rangle$  to the trion states  $|t_{\pm}\rangle$ , respectively.

So, under the excitation of an optical pulse with  $\sigma^+$  polarization, the dynamics is reduced to a Raman rotation in the  $\Lambda$ -type three-level system [as shown in Fig. 21 (b)], which is governed by the Hamiltonian

$$H = \omega_c s_x - \Omega^*(t)|+1/2\rangle\langle t_+| - \Omega(t)|t_+\rangle\langle +1/2| - \Delta|t_+\rangle\langle t_+|, \quad (8)$$

where  $s_{x/y/z}$  is the electron spin operator along the  $x$ ,  $y$ , or  $z$  direction, respectively,  $\Omega(t)$  is Rabi frequency of the laser pulse in the rotating frame, and  $\Delta$  is the detuning of the laser relative to the trion state  $|t_+\rangle$ . To eliminate the dynamic phase associated with Zeeman splitting, the quantum operation should be done in the frame rotating together with the free spins under the magnetic field. By the transformation  $S \equiv \exp(i\omega_c t s_x)$ , the Hamiltonian in the precessing frame is written in the matrix form

$$\tilde{H} = \begin{bmatrix} 0 & 0 & -\Omega^*(t)e^{+i\omega_c t/2}/\sqrt{2} \\ 0 & 0 & -\Omega^*(t)e^{-i\omega_c t/2}/\sqrt{2} \\ -\Omega(t)e^{-i\omega_c t/2}/\sqrt{2} & -\Omega(t)e^{+i\omega_c t/2}/\sqrt{2} & -\Delta \end{bmatrix}, \quad (9)$$

in the basis of  $e^{+i\omega_c t/2}| -x\rangle$ ,  $e^{-i\omega_c t}| +x\rangle$ , and  $|t_+\rangle$ .

For large detuning ( $|\Delta|$  much greater than the bandwidth of the optical pulse and the Rabi frequency), the so-called adiabatic approximation is justified and thus under a standard canonical transformation, the off-diagonal terms in the Hamiltonian between the electron spin states and the trion state are eliminated up to the second order of the Rabi frequency. So the transformed effective Hamiltonian is approximated as

$$\tilde{H}_{\text{eff}} \approx \begin{bmatrix} |\Omega(t)|^2/(2\Delta) & -|\Omega(t)|^2 e^{+i\omega_c t}/(2\Delta) & 0 \\ -|\Omega(t)|^2 e^{-i\omega_c t}/(2\Delta) & |\Omega(t)|^2/(2\Delta) & 0 \\ 0 & 0 & -\Delta - |\Omega(t)|^2/\Delta \end{bmatrix}. \quad (10)$$

This is equivalent to a magnetic field with strength  $|\Omega(t)|^2/(2g\mu_B\Delta)$  precessing in the  $x$ - $y$  plane with the angular frequency  $\omega_c$  (the time-dependent optical Stark shift [311] of the electron energy  $|\Omega(t)|^2/(2\Delta)$  contributes only a trivial global phase-shift and can be ignored). In cases that the optical pulse is much shorter than the spin precession period, the effective magnetic field

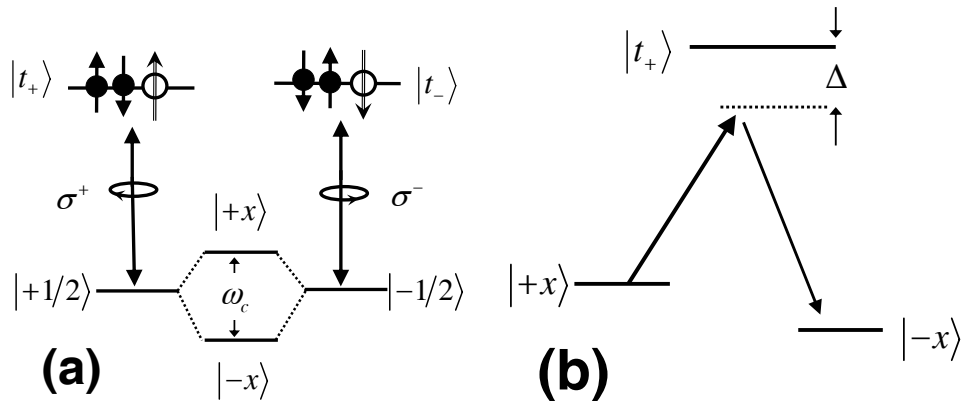


FIG. 21. (a) Optical selection rules for the electron-trion transitions. (b) The Raman process in the  $\Lambda$ -type three-level system formed by the electron spin states and the trion states connected by a  $\sigma^+$ -polarized laser pulse.



becomes an instantaneous pulse which can be controlled in the femtosecond timescales (c.f. the GHz limit on the control of external magnetic field). For  $t \approx n\pi/(\omega_c)$  ( $n$  is an integer, the magnetic field pulse is effectively along the  $z$ -axis, and for time around  $(n + 1/2)\pi/\omega_c$ , the instantaneous rotation of the spin is effectively along the  $y$ -axis. Thus we have two SU(2) generators which can be combined to complete an arbitrary rotation of the electron spin. To be specific, a spin rotation with angle  $\gamma$  along an axis defined by the Euler angles  $(\alpha, \beta)$ , denoted as  $R(\alpha, \beta, \gamma)$ , can be realized by at most 3 elementary rotations along different axes in the  $x$ - $y$  plane, for

$$R(\alpha, \beta, \gamma) = R\left(\frac{\pi}{2}, \frac{\pi}{2} + \beta, \frac{\pi}{2} - \alpha\right) R\left(\frac{\pi}{2}, \beta, \gamma\right) R\left(\frac{\pi}{2}, -\frac{\pi}{2} + \beta, \frac{\pi}{2} - \alpha\right), \quad (11)$$

where the three elementary rotations on the righthand side of the equation can be performed in turn at  $t = -\pi/(2\omega_c) + \beta/\omega_c$ ,  $\beta/\omega_c$ , and  $+\pi/\omega_c + \beta/\omega_c$ , which can be completed within half the precession period of the electron spin. For an electron with Zeeman splitting of 1 meV, the duration of an arbitrary operation of a single spin is less than 2 ps.

To complete a finite rotation of the spin at a time much shorter than the precession period, the Rabi frequency should be large, which, however, could demolish the condition for the adiabatic approximation. For instance, if the Zeeman splitting is 0.1 meV and the detuning is 1 meV, to complete a  $\pi$  rotation within a duration one tenth of the precession period, the Rabi frequency is required to be about 3 meV, greater than the detuning, which makes the adiabatic approximation unjustified. In fact, to validate the adiabatic condition for instantaneous operations, it is required that  $\omega_c \ll \Delta$ , which means slow operations for reasonably large detuning ( $\Delta < 10$  meV). Alternatively, by shaping the control laser pulse, the rotation can also be operated in the non-adiabatic regime or in a non-instantaneous manner. No matter how intense and how fast the optical pulse could be, the spin rotation in general cases, however, is still limited by the precession period, as can be seen from the equation for the spin polarization as

$$\partial_t \langle s_z \rangle = \omega_c \langle s_y \rangle - \partial_t \rho_t, \quad (12)$$

where  $\rho_t$  is the population of the trion state. For a complete operation, the residue population of the trion should be zero, so the change of the spin momentum along the  $z$ -direction is  $|\delta \langle s_z \rangle| = \left| \omega_c \int_0^t \langle s_y \rangle dt \right| \leq \omega_c t$ , which cannot be faster than the precession under the static external magnetic field.

In summary, under a moderate external magnetic field ( $\lesssim 10$  T and  $\omega_c \sim 1$  meV), an arbitrary spin rotation can be accomplished well within 10 ps by up to three ultrashort optical pulses (with simple shape and large detuning) or by one pulse (with engineered shape). Remarkably, control of single electron spins [79, 236, 312] and hole spins [78] in QDs in picosecond timescales have been recently realized in experiments. Using the optical control, Yamamoto's group has demonstrated spin echo for an ensemble of impurities in GaAs [181] and for a single QD spin [313]. Greilich et al have realized optical rotation of an ensemble of QD spins along arbitrary axes [182].

## B. Two-qubit gates by optical RKKY interaction

To implement two-qubit quantum gates, optically induced RKKY interaction (ORKKY) between electrons doped in QDs has been proposed to couple two spins, laterally via continuum excitons [73, 74] or vertically via discrete states [75]. The ORKKY interaction mediated by continuum excitons [73, 74], due to the extension nature of the continuum states, is less controllable in selectively coupling certain spins. The ORKKY interaction between QDs vertically stacked [75], on the other hand, is not applicable to a scalable system with a planar layout. For the sake of scalability, we consider to employ the discrete excited states in laterally coupled QDs to induce the ORKKY interaction, which, as described below, can be controlled to selectively couple spins in designated adjacent QDs. The ORKKY interaction is by nature a Raman process with the ground states formed by the two-electron spin states and the intermediate states by excitons charged with two excess electrons.

The physical process of the optically induced RKKY interaction via discrete intermediate states is depicted by the Feynmann diagram in Fig. 22 (a). The qubits under controls are the spins of two electrons in the ground states of two neighboring QDs, denoted as  $\mathbf{s}_1$  and  $\mathbf{s}_2$ . When the electrons are in the ground states, the inter-dot tunneling is negligible and therefore the two spins have no direct exchange interaction. The basic elements of the ORKKY process for mediated interaction between the two qubits can be described as:

1. an incident optical pulse excites a direct electron-hole pair into the excited electron and hole levels in, say, QD 1, denoted as  $|e_1\rangle \otimes |h_1\rangle$ ;
2. the optically excited electron will interact with the electron spin  $\mathbf{s}_1$  with the strong exchange interaction ( $\lambda_i \sim 5$  meV in a typical InAs QD), while the electron-hole exchange interaction is negligible in comparison;
3. with a strong quasi-cw optical field applied, the excited electron levels in the two QDs can be tuned into resonance by the optical Stark effect, and thus the electron in the excited state  $|e_1\rangle$  can resonantly tunnel into the second QD with the tunneling rate in the order of 10 meV for two QDs separated by 15 nm, while the hole tunneling can be neglected due to the stronger confinement and off-resonance condition;

4. having tunnelled into the excited level of the second QD, the optically excited electron can exchange spins with the excess electron in the second QD via the strong exchange interaction;
5. after the exchange interaction with the second qubit electron, the electron in the excited state can tunnel back into the first QD;
6. the electron back to the first QD can be recombined with the hole by emitting a photon back into the optical pulse, leaving the two excess electrons an effect of indirect spin exchange. Since the laser frequencies can be adjusted to selectively excite the exciton in one QD and to selectively shift the level in another QD by the AC Stark effect, a pair of adjacent QDs can be coupled on demand.

Since the Coulomb and the exchange interactions could be strong for electrons in the discrete states, as compared with the optical Rabi frequency, it is better to treat the interactions non-perturbatively by first exactly diagonalizing the states of charged excitons, and use the eigenstates as the basis for calculating the optically induced indirect exchange interaction. In fact, when the intermediate states are discrete eigenstates of the Coulomb interaction, the ORKKY process becomes equivalent to the Raman process in the multi-level systems with the two-spin states as the ground states and the charged exciton states as the intermediate states. Then the optical excitation can be treated as a perturbation, similar to the case of the single-spin rotation, and the adiabatic approximation may also be adopted when the detuning is large.

As shown in Fig. 22 (b), we assume the following characteristic energies for two neighboring QDs of different sizes, which can be realized by properly adjusting the QD sizes, the separation, and the composite  $x$  in  $\text{In}_{1-x}\text{Ga}_x\text{As}$  in typical cases under consideration: The difference in transition energy between the neighboring dots is  $\delta_{12} \sim 10$  meV, the distance between the ground and excited electron states  $E_{01} \sim 50$  meV, the tunneling strength between neighboring excited states  $t_{12} \sim 10$  meV, and the Coulomb exchange energy between electrons  $\lambda_{1/2} \sim 5$  meV. When the electron-hole pair is excited into the excited single-particle levels in the smaller QD, the difference between the binding energy of the direct exciton (when both the electron and the hole are in the smaller dot) and that of the indirect exciton (when the electron has tunnelled into the large dot), which is  $\sim 10$  meV, can already compensate most of the energy difference ( $\delta_{12}$ ) between the excited single-particle levels in the two dots. And if desired, a further optical pumping can be used to fine-tune the energy levels in the dots so that near-resonance tunneling can occur between the excited levels for electrons in the two dots. The ground single-particle states for electrons and the hole states can be virtually taken as localized due to the relatively high barrier.

To illustrate the basic idea of using the discrete exciton states in laterally coupled QDs for ORKKY interaction between the two qubit spins, we assume that the hole is (virtually) created by the optical pulse only at the first excited level in the smaller QD and the dynamics is essentially determined by the interaction between the two qubit spins and the optically excited electron. The role of the hole is then just to impose the renormalization of the electron energies. As mentioned above, both the tunneling and Coulomb exchange are in the strong coupling regime, they should be considered non-perturbatively. So we can first diagonalize the Hamiltonian with the exchange energy and electron tunneling fully included. As the tunneling is spin-independent, we consider only the bond state of the QD molecule and treat the anti-bond state as in far off-resonance (since it is about 10 meV above). Thus the relevant spins are qubit 1 ( $s_1$ ), qubit 2 ( $s_2$ ), and the spin of the bond molecular state 3 ( $s_3$ ). The Hamiltonian of these three spins is

$$H = 2\lambda_1 s_1 \cdot s_3 + 2\lambda_2 s_2 \cdot s_3 + 2\omega_c (s_1^z + s_2^z + s_3^z), \quad (13)$$

where  $\lambda_1$  and  $\lambda_2$  are the exchange energy in each dot. For simplicity, we assume  $\lambda_1 = \lambda_2 = \lambda$ . The eigenstates and the

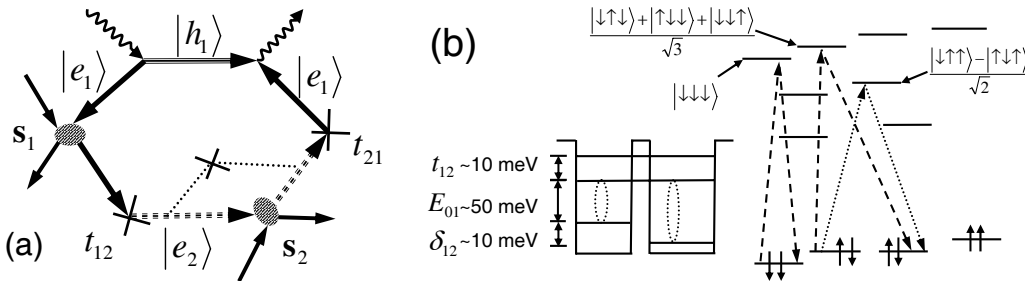


FIG. 22. (a) Feynman diagram for optical RKKY interaction. The straight arrows are electron or holes lines, the wavy arrows are photon lines, the tunneling is the cross vertices, the Coulomb exchange is the scattering vertices, and the AC Stark field is the dotted lines with cross. (b) Energy level schematics for two-qubit gates. The two-spin states are split by the magnetic field, and the exciton charged with two electrons (the hole is understood) is split both by the Coulomb exchange energy and by the magnetic field. The dotted arrows are optical excitation for a SWAP gate, which together with the excitation represented by dashed arrows can also accomplish the phase gate.

corresponding eigen energies can be worked out as

$$\begin{aligned}
|S, \frac{1}{2}, -\frac{1}{2}\rangle &= \frac{1}{\sqrt{2}}(|\downarrow\uparrow\downarrow\rangle - |\uparrow\downarrow\downarrow\rangle), & \varepsilon &= -\omega_c, \\
|S, \frac{1}{2}, +\frac{1}{2}\rangle &= \frac{1}{\sqrt{2}}(|\uparrow\downarrow\uparrow\rangle - |\downarrow\uparrow\uparrow\rangle), & \varepsilon &= +\omega_c, \\
|P, \frac{3}{2}, -\frac{3}{2}\rangle &= |\downarrow\downarrow\downarrow\rangle, & \varepsilon &= \lambda - 3\omega_c, \\
|P, \frac{3}{2}, -\frac{1}{2}\rangle &= \frac{1}{\sqrt{3}}(|\uparrow\downarrow\downarrow\rangle + |\downarrow\uparrow\downarrow\rangle + |\downarrow\downarrow\uparrow\rangle), & \varepsilon &= \lambda - \omega_c, \\
|P, \frac{3}{2}, +\frac{1}{2}\rangle &= \frac{1}{\sqrt{3}}(|\downarrow\uparrow\uparrow\rangle + |\uparrow\downarrow\uparrow\rangle + |\uparrow\uparrow\downarrow\rangle), & \varepsilon &= \lambda + \omega_c, \\
|P, \frac{3}{2}, +\frac{3}{2}\rangle &= |\uparrow\uparrow\uparrow\rangle, & \varepsilon &= \lambda + 3\omega_c, \\
|P, \frac{1}{2}, -\frac{1}{2}\rangle &= \frac{1}{\sqrt{6}}(|\uparrow\downarrow\downarrow\rangle + |\downarrow\uparrow\downarrow\rangle - 2|\downarrow\downarrow\uparrow\rangle), & \varepsilon &= -2\lambda - \omega_c, \\
|P, \frac{1}{2}, +\frac{1}{2}\rangle &= \frac{1}{\sqrt{6}}(|\downarrow\uparrow\uparrow\rangle + |\uparrow\downarrow\uparrow\rangle - 2|\uparrow\uparrow\downarrow\rangle), & \varepsilon &= -2\lambda + \omega_c,
\end{aligned} \tag{14}$$

as schematically shown in Fig. 22 (b), where the up/down arrows indicate in turn the spin states of qubit 1, qubit 2, and the electron created by optical excitation, quantized along the external magnetic field direction. Notice  $\lambda \sim 5 \text{ meV} \gg 2\omega_c \sim 1 \text{ meV}$ . The two-qubit gates can just be realized by the Raman passages between the two-spin ground states mediated by the charged excitons formed by one hole plus three electrons in the spin states shown above. To be specific, we discuss two frequently used two-qubit gates as below.

### 1. SWAP and $\sqrt{\text{SWAP}}$ gates

A SWAP gate interchanges the states of two qubits. Its matrix form is shown in Fig. 45. In the Raman process, it just flips the two states:  $|\uparrow\downarrow\rangle$  and  $|\downarrow\uparrow\rangle$ . The intermediate state connecting these two states by Raman process is  $|S, \frac{1}{2}, \frac{1}{2}\rangle \equiv \frac{1}{\sqrt{2}}(|\uparrow\downarrow\uparrow\rangle - |\downarrow\uparrow\uparrow\rangle)$  (henceforth the hole state in the exciton has been omitted for the sake of simplicity), which is optically coupled only to the two-spin singlet state  $\frac{1}{\sqrt{2}}(|\uparrow\downarrow\rangle - |\downarrow\uparrow\rangle)$ . By performing a  $2n\pi$  Rabi rotation between the intermediated exciton state and the singlet ground state, a pure phase-shift will be induced to the singlet state, whose value is determined by the detuning. When such a phase-shift is controlled to be  $\pi$  (which can be obtained by, e.g., setting the rotation angle to be  $2\pi$  and the detuning is zero), the two states  $|\uparrow\downarrow\rangle$  and  $|\downarrow\uparrow\rangle$  are just flipped and the SWAP gate is realized. In practice, the optical pulse can be tuned off-resonance from the transition to suppress the spontaneous decay. With proper polarization, the optical pulse doesn't excite the nearby state  $|S, \frac{1}{2}, -\frac{1}{2}\rangle$  and all other transitions are at separated by an energy of  $\lambda$ . So this operation can be accomplished in a period of time  $\sim 10 \times (2\pi\lambda^{-1}) \sim 10 \text{ ps}$ . Considering the optical Stark pulse used for tuning the resonant tunneling, a two-qubit SWAP gate in such a scheme would require two optical pulses of duration of about 10 ps.

By choosing a proper detuning, the phase-shift can also be controlled to be  $\pi/2$ , and then the SWAP gate is performed halfway, or the  $\sqrt{\text{SWAP}}$  gate is realized, which has the matrix form

$$U_{SS} = \begin{pmatrix} 1 & 0 & 0 & 0 \\ 0 & \frac{1+i}{2} & \frac{1-i}{2} & 0 \\ 0 & \frac{1-i}{2} & \frac{1+i}{2} & 0 \\ 0 & 0 & 0 & 1 \end{pmatrix}. \tag{15}$$

The  $\sqrt{\text{SWAP}}$  gate can generate entanglement between the two spins and can be used to realize the controlled phase gate and the CNOT gate.

### 2. Controlled phase gate

Another two-qubit gate which can be used in lieu of the CNOT gate for universal quantum computation is the controlled phase gate which induces a phase-shift of the target qubit depending on the state of the controlling qubit. The general matrix form of the controlled phase gate is

$$\begin{pmatrix} e^{i\phi_{\downarrow\downarrow}} & 0 & 0 & 0 \\ 0 & e^{i\phi_{\downarrow\uparrow}} & 0 & 0 \\ 0 & 0 & e^{i\phi_{\uparrow\downarrow}} & 0 \\ 0 & 0 & 0 & e^{i\phi_{\uparrow\uparrow}} \end{pmatrix} = e^{i\frac{\phi_{\downarrow\uparrow} + \phi_{\uparrow\downarrow}}{2}} [R_x(\phi_{\downarrow\downarrow} - \phi_{\downarrow\uparrow}) \otimes R_x(\phi_{\downarrow\uparrow} - \phi_{\downarrow\downarrow})] \begin{pmatrix} 1 & 0 & 0 & 0 \\ 0 & 1 & 0 & 0 \\ 0 & 0 & 1 & 0 \\ 0 & 0 & 0 & e^{i\phi} \end{pmatrix}, \tag{16}$$

where the subscript of the phase-shift indicates the corresponding qubit states,  $R_x(\theta)$  is the single qubit phase-shift of  $\theta$ , and  $\phi \equiv \phi_{\downarrow\downarrow} + \phi_{\uparrow\uparrow} - \phi_{\downarrow\uparrow} - \phi_{\uparrow\downarrow}$ . When  $\phi = \pi$ , the phase gate can be transformed into the CNOT gate by applying certain single-spin gates, which are usually assumed much easier than the two-qubit gates.

As shown in Fig. 22 (b), to obtain the phase-shift, an optical pulse is applied to couple the state  $|\downarrow\downarrow\rangle$  to the exciton state  $|P, \frac{3}{2}, -\frac{3}{2}\rangle \equiv |\downarrow\downarrow\downarrow\rangle$ . The pulse shifts the states by optical Stark effect and induces the phase shift  $\phi_{\downarrow\downarrow}$ . This pulse will also couple the electron state  $(|\downarrow\uparrow\rangle + |\uparrow\downarrow\rangle)/\sqrt{2}$  to the exciton state  $|P, \frac{3}{2}, -\frac{1}{2}\rangle \equiv (|\downarrow\uparrow\downarrow\rangle + |\uparrow\downarrow\downarrow\rangle + |\downarrow\downarrow\uparrow\rangle)/\sqrt{3}$ , inducing a phase shift to  $(|\downarrow\uparrow\rangle + |\uparrow\downarrow\rangle)/\sqrt{2}$  and thus the rotation between  $|\downarrow\uparrow\rangle$  and  $|\uparrow\downarrow\rangle$ . To obtain a pure phase gate, another pulse (with the same energy and polarization as in the SWAP gate) coupling the states  $(|\downarrow\uparrow\rangle - |\uparrow\downarrow\rangle)/\sqrt{2}$  and  $|S, \frac{1}{2}, \frac{1}{2}\rangle \equiv (|\downarrow\uparrow\uparrow\rangle - |\uparrow\downarrow\uparrow\rangle)/\sqrt{2}$  can be used to compensate the rotation. Finally, the conditional phase-shift is  $\phi \equiv \phi_{\downarrow\downarrow} - \phi_{\downarrow\uparrow} - \phi_{\uparrow\downarrow} = -\frac{1}{3}\phi_{\downarrow\downarrow}$ . Similar to the case of the SWAP gate, a phase-shift gate can be realized with three pulses (including the optical Stark pulse) of duration of about 10 ps.

### C. Issues to be considered

In realistic cases, there are several issues which could degrade the fidelity of the quantum gates.

The first one is the relaxation of the intermediate state by spontaneous emission. In the stimulated Raman adiabatic passage [310], the spin states can be flipped without populating the exciton state, which, however, cannot perform a general quantum gate since such a passage depends on the initial state of the spin. To have a general quantum gate which transforms a spin independent of the initial state, both the dark and bright states should be employed. To suppress the spontaneous emission and other scattering processes, it is preferable to have large detuning so as to minimize the population of the intermediate state [68, 72, 169, 173].

Another important effect affecting the fidelity is the imperfection of the selection rules and the hole-mixing [71]. In realistic cases, the QDs would never have perfectly symmetric shape and thus the lateral confinement could cause mixing between states of different angular momentum (such as the heavy-light hole mixing), which is worse for the excited states involved in the two-qubit gates. Such effects, however, only induce systematic errors or unwanted dynamics to the quantum gates designed for ideal condition. In principle, the shapes, polarizations, and timings of the controlling laser pulses can always be readjusted once the realistic system parameters have been measured. It could also be possible to design pulses of certain robustness against small deviations in the system parameters [120, 314], and a scheme of using chirped pulse to implement quantum gates robust against the mixing effect has been proposed [71].

For QDs with reflection symmetry with respect to the growth plane, the imperfect selection rules may be tolerated by re-designing the polarization of the control light. In general cases, especially for small QDs which have irregular shapes, the hole mixing may be used as a resource for quantum control. In previous discussions in Sec. IV A, a static magnetic field applied along a direction other than the growth direction has been required to break the rotation symmetry so that an arbitrary rotation of a single spin is possible. When the conservation of angular momentum with respect to the growth direction is not perfect and thus the “forbidden” transitions would be made partially “allowed” due to the hole mixing, an effective magnetic field along an arbitrary direction for the spin could be induced by a properly polarized light beam through the AC Stark effect and an arbitrary rotation of a single spin could be realized even without an external magnetic field applied. More discussions about the hole mixing and its effects on the optical control are given in Appendix A.

The third problem with the scalability of the quantum computation is the complexity in the energy level structure of multi-dot systems. The analysis and characterization of the many levels with a number of excess electrons require much effort and furthermore [315–319], the optical pulses applied to a desired transition would inevitably affect the other transitions in QDs nearby, making the pulse design very demanding when the system becomes large. In femtosecond chemistry, learning algorithms have been developed to design sophisticated pulses for controlling the complex atomic and molecular dynamics [320–322]. We expect the quantum learning algorithm be a powerful tool to deal with the design complexity in multi-dot systems.

With recent experimental progresses demonstrating the feasibility of optical control of single spins, the optical control of two spins for implementing two-qubit quantum gates is an immediate milestone for future experiments. Indeed, the recent systematic investigation of the optical transitions in coupled QD structures [268, 315, 317–319] has laid a cornerstone for this target.

## V. QUBIT INITIALIZATION

A rapid and continuous supply of refreshed qubits is one criteria for scalable quantum computation [2]. Such a requirement is not only a prerequisite for the initialization of a quantum computer, but also a key element for quantum error correction where errors are continuously generated during the operation in noisy environments and by imperfect control. The initial preparation of a quantum computer could be done slowly, e.g., by simply cooling the system to very low temperature. For quantum error correction, however, rapid reset of qubits is crucial to recycle the spoiled qubits, otherwise a (infinitely) large number of fresh qubits should be prepared and preserved before a quantum computation commences so that the erroneous qubits could be replaced. The dynamical recycling strategy is more economical than a static supply of many qubits which deteriorate. It is desirable that the machine be as small as possible, with operation cost as trade-off.

The essence of qubit initialization is preparing a pure quantum state out of a mixed one. It amounts to cooling a qubit (ideally) to absolutely zero temperature. Thus the key physical process is dumping entropy to the environment. The aim is to build a quantum refrigerator in analogy to a reverse Carnot cycle. In general, the cycle consists of the following steps [120, 256, 257, 323–326]: (1) pumping of the system to an excited state; and (2) relaxation of the excited system with entropy dumped into the environment. To initialize the spin qubit in an ultrafast timescale, a quantum channel capable of dumping entropy rapidly is required.

In a QD, the only available thermal baths for dumping the entropy of an electron spin are the nuclear spins, the host lattice (the phonon bath), and the electromagnetic environment (the photon bath). The coupling between the electron spin and the nuclear spins is very weak (with the rate in the order of  $10^{-6} \text{ sec}^{-1}$ ), so only the phonon or photon bath could be used as entropy drain. The direct coupling of an electron spin with either the lattice vibration or the electromagnetic modes is known to be very weak. The solution is to transfer the spin state into orbital states which couple to the phonon or photon bath strongly. The entropy dissipation by rapid photon channel can be realized by optically pumping the spin states to a trion state and coupling the trion to a photon in a strongly coupled QD-microcavity-waveguide structure [120]. Or alternatively, excited trion states may provide an efficient entropy channel realized by the rapid phonon emission in QDs. Below we discuss these two possibilities.

## A. Initialization by entropy dumping to photon baths

### 1. Optical pumping

The idea of initializing a spin by optical pumping is illustrated in Fig. 23: An optical light brings one of the two spin states into a trion state, and then the trion state relaxes to either spin state by spontaneous emission. After sufficient cycling of the pumping process, the electron spin will be in the state that is not coupled to the trion state by the pump light, which has been demonstrated recently in experiments for single electron spins in QDs [256, 257]. The scheme has also been applied to initialize single heavy-hole spins in QDs [255]. With essentially the same physics, optical pumping has also been used to initialize spins of NV centers in diamond [90, 95].

To selectively excite only one electron spin state, one can choose the light polarization so that one transition is “forbidden” due to the selection rules. The selection rules are based on some symmetry, such as the (approximate) rotational symmetry about the growth direction. To exploit the selection rules resulting from the rotational symmetry, one can use a circularly polarized light. A  $\sigma_+$  polarized light, e.g., couples the spin state  $|+1/2\rangle$  to the trion state  $|t_+\rangle$  (see Fig. 23). Then the trion state will relax to both spin states by spontaneous emission. Now we have a dilemma: The selection rule prevents the spin state  $| - 1/2\rangle$  to be reached. But remember the selection rules we have are approximate and the “forbidden” transitions are actually slightly allowed. According to the discussions in Appendix A, the trion state  $|t_+\rangle$  has a small probability ( $\sim \zeta'^2$ ) to relax to the “forbidden” state  $| - 1/2\rangle$ . Also, due to the approximate selection rules, the state  $|t_-\rangle$  may be slightly excited, and the spin state  $| - 1/2\rangle$  can be excited by the  $\sigma_+$ -polarized light to the two trion states, which degrades the initialization efficiency. Furthermore, a magnetic field can be applied along the growth direction (i.e., in the Faraday configuration), so that all the transitions except the desired ones as depicted in Fig. 23 are off-resonance from the pump light. Thus the pump process is characterized by several rates: The excitation rate  $G$ , the spontaneous emission rates  $\Gamma$  and  $\tilde{\Gamma} \equiv \Gamma\zeta'^2$  (to the spin up and spin down states, respectively), and the longitudinal spin relaxation rate  $\gamma_1 \equiv T_1^{-1}$ . The rate equations for the trion population  $p_t$  and the electron populations in the two

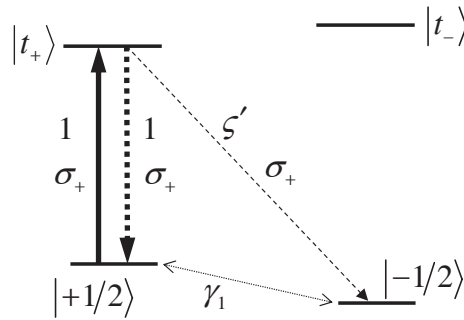


FIG. 23. Optical pumping of a spin in the Faraday configuration. The solid line indicates the optical excitation, and the dotted lines indicate the spontaneous emission. The polarization and the relative dipole matrix element for each transition are indicated. The two spins states are connected by a spin-flip process with rate  $\gamma_1$ .

spin states  $p_{\pm}$  are established as

$$\dot{p}_t = -(\Gamma + \tilde{\Gamma})p_t + Gp_+, \quad (17a)$$

$$\dot{p}_+ = -\gamma_1 p_+ + \gamma_1 p_- + \Gamma p_t - Gp_+, \quad (17b)$$

$$\dot{p}_- = -\gamma_1 p_- + \gamma_1 p_+ + \tilde{\Gamma} p_t. \quad (17c)$$

The quality of the initialization may be quantified by two factors: the saturation time  $T_s$  and the saturation spin polarization  $P_s$ . In a typical GaAs or InAs QD at low temperature and under a moderately strong magnetic field,  $\Gamma \sim 10^9 \text{ s}^{-1}$ ,  $\gamma_1 \sim 10^3 \text{ s}^{-1}$  (see Sec. II C for details), and  $\zeta' \sim 1\%$  (for a unstrained dot [81], the value may be increased by strain [80]). Assuming the pumping rate  $G \gg \Gamma$ , we obtain by the rate equations (note the trion population will eventually becomes spin up population when the light is switched off)

$$T_s \sim 10/\tilde{\Gamma} \sim 0.1 \text{ ms}, \quad (18a)$$

$$P_s \cong p_- - p_+ - p_t \approx 1 - 2\gamma_1/\tilde{\Gamma} \sim 98\%. \quad (18b)$$

Such a high degree of electron spin polarization by optical pumping has been experimentally demonstrated [256]. The initialization by optical pumping in the Faraday configuration, however, is rather slow and the saturation polarization is limited by the spin flip rate relative to the ‘‘forbidden’’ spontaneous emission rate. Furthermore, the energy cost of the pump light is considerable. To see the energy cost of the optical pumping in the Faraday configuration, we notice that for just one useful photon emitted (which results in the target spin state), the number of photon wasted (by spontaneous emission resulting in the original state) is  $\zeta'^{-2} \sim 400$  – only 0.25% energy of the pump light has been effective. The limiting factor is the small dipole moment for the ‘‘forbidden’’ transition.

The solution is straightforward. One can work in the Voigt configuration in which a magnetic field is applied in plane to quantized the electron spins to be  $|\pm x\rangle$  [118, 257, 325]. As shown in Fig. 24, now both spin eigenstates are connected to a trion state by a  $\sigma_+$ -polarized excitation with the same dipole matrix element. The efficiency of optical pumping in the Voigt configuration can be discussed similarly to that in the Faraday configuration. But now there is another limiting factor of the saturation polarization: the backward optical excitation process from the target spin state to the trion state which, though off-resonance, is not negligible because of the large dipole matrix element. The generation rate of the trion by the off-resonance excitation is  $\tilde{G} \equiv G\Gamma^2/(\Gamma^2 + \omega_c^2)$  where  $\omega_c$  is the angular Lamor frequency of the electron spin in the magnetic field. The rate equations for the trion population  $P_t$  and the electron populations in the two spin states  $P_{\pm}$  are established as

$$\dot{p}_t = -2\Gamma p_t + Gp_+ + \tilde{G}p_-, \quad (19a)$$

$$\dot{p}_+ = -\gamma_1 p_+ + \gamma_1 p_- - Gp_+ + \Gamma p_t, \quad (19b)$$

$$\dot{p}_- = -\gamma_1 p_- + \gamma_1 p_+ - \tilde{G}p_- + \Gamma p_t. \quad (19c)$$

Under the condition that  $G \gg \Gamma \gg \tilde{G} \gg \gamma_1$  (e.g.,  $G = 10\Gamma$  and  $\omega_c = 10^2\Gamma \sim 10^{11} \text{ s}^{-1}$ ), the efficiency of the initialization by optical pumping in the Faraday configuration is characterized by

$$T_s \sim 10/\Gamma \sim 10 \text{ ns}, \quad (20a)$$

$$P_s \cong p_- - p_+ \approx 1 - \tilde{G}/\Gamma \sim 99.9\%. \quad (20b)$$

Owing to using the allowed transition in the Voigt configuration instead of the forbidden transition in the Faraday configuration, the spin initialization is faster by orders of magnitude. Also, the saturating polarization is much closer to unity since now the limiting factor is the off-resonance transition probability relative to the resonant one, instead of the spin-flip rate relative to

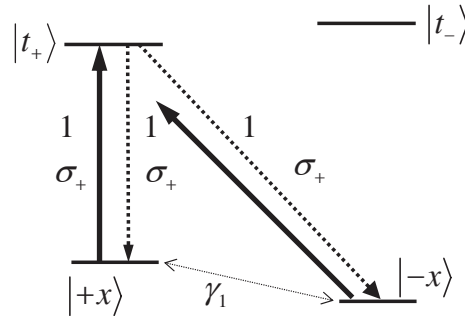


FIG. 24. The same as Fig. 23 except that the setup is in the Voigt configuration.

the trion recombination rate due to the forbidden transition in the Faraday configuration. The off-resonance transition could be suppressed simply by enlarging the electron Zeeman splitting. There are calculations [325] and experiments [257] demonstrating efficient optical pumping of single electron spins in the Voigt configuration.

## 2. Single-shot initialization with cavity enhancement

In the previous discussion on spin initialization by optical pumping, we have seen that it is crucial to have a rapid entropy dumping channel to have efficient qubit cooling. The cooling duration of 10 ns is acceptable in many cases, but it is still highly desirable to have even faster spin initialization so that the qubit refreshing rate could catch up with the quantum gate and the error generation rate. Suppose the error rate per qubit per operation is about the quantum error correction threshold  $10^{-3}$  and about 10 physical qubits are used to code one logical qubit to incorporate the error correction within the quantum logic. As we have discussed, the optical control for a simple quantum gate should take about 10 ps. That means we should have a qubit reset rate well above 1 qubit per nanosecond to avoid quantum computation being held up due to the lack of refreshed qubits. To have such ultrafast spin initialization, the entropy dumping channel should be specially engineered. One possible approach is to enhance the coupling to the photon bath by increasing the local density of states of photon modes. This enhancement is possible by putting a QD in the proximity of a microcavity [120]. As has been discussed earlier, a micro-photonic structure is in any case needed to form a scalable large structure of QDs for distributed quantum computation. Here we discuss how the in-situ cavity QED may be used to selectively enhance the photon emission for entropy dumping and hence for ultrafast spin initialization, following the procedure of Ref. [120].

The basic structure is depicted in Fig. 25. To be specific, we consider a micro-ring coupled to a QD. Such a structure may be constructed by etching a semiconductor surface where QDs are located. Structures in photonic crystals should be ideal alternatives (see Sec. III B). The specific structure, however, is not crucial to the physics to be discussed below. The attached micro-cavity would strongly modify the electromagnetic vacuum in the vicinity of the QD. The coupling to the cavity mode (which is taken as a whispering gallery mode) is realized due to the overlap between the QD and the evanescent wave of the cavity mode. A waveguide coupled to the cavity serves as a quantum channel for a cavity photon to escape rapidly to the environment. For the purpose of spin cooling, such a directional waveguide is not necessary, and actually one could as well use a cavity with large leakage (bad cavity situation). Since the emitted photon carries certain information about the qubit, a guided channel with cavity also enables such information to be retrieved, either for quantum measurement (as will be discussed later) and for quantum error diagnosis. The incorporation of a waveguide along a cavity then involves extra designing and fabricating cost.

We consider the Voigt configuration. The spin eigenstates under a static magnetic field in the  $x$  direction are denoted  $|\pm\rangle$ . The spin states may be flipped to the two degenerate trion (exciton plus an electron) states  $|T\mp\rangle$  or  $|T\pm\rangle$  by an  $X$ - or  $Y$ -polarized tipping pulse, respectively. The trion states are, by design, off-resonance from the cavity modes. We assume such off-resonance condition for several considerations: (1) It avoids the cavity-induced optical decoherence during quantum operations of the spin. (2) A local node usually consists of a number of QDs to a cavity, so it is unlikely to have all the QDs are in resonance with a cavity mode. (3) The resonance coupling may be realized by transient control via optical Stark effect which provides flexibility for selectively initialize a spin in a QD in the cluster. The relevant cavity mode is denoted by  $|C\rangle$ . The evanescent wave of the cavity mode is designed to be  $X$ -polarized in the vicinity of the nanodot, so that when brought within resonance, the trion states  $|T\pm\rangle$  and the cavity states  $|\mp, C\rangle$  are coupled into two split trion-polariton states, respectively. This provides a fast decay of the trion to a spin state by emitting a photon into the quantum channel. The pump light is  $Y$ -polarized so that a Raman pathway is formed from the spin state  $|+\rangle$  to the trion state  $|T+\rangle$  (by the optical pumping), to the cavity state  $|- , C\rangle$  (by dot-cavity coupling), and to the spin state  $|-\rangle$  (by spontaneous photon emission into the waveguide).

The optical cycle (similar to a reverse Carnot cycle) for cooling a spin qubit is illustrated in Fig. 26 [120]. Without loss of generality, we assume that the electron before optical pumping is in an unpolarized state, i.e.,  $\hat{\rho}(-\infty) = 0.5|-\rangle\langle -| + 0.5|+\rangle\langle +|$ . A

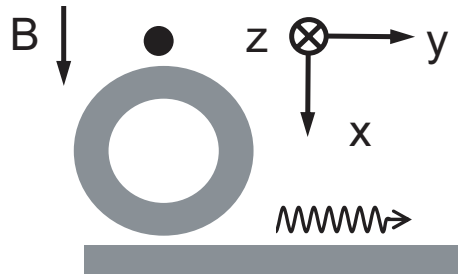


FIG. 25. Schematics of the dot-cavity-waveguide coupling structure.

cooling cycle consists of four basic steps:

1. An X-polarized AC Stark pulse is adiabatically switched on, bringing the states  $|T+\rangle$  and  $|-, C\rangle$  into resonance by AC Stark effect.
2. A Y-polarized pump pulse flips the spin up state  $|+\rangle$  to the polariton states formed by  $|T+\rangle$  and  $|-, C\rangle$ .
3. The polariton states relax to the spin down state  $|-\rangle$  rapidly by emitting a photon into the waveguide, dumping the spin entropy to the environment.
4. The AC Stark pulse is adiabatically switched off. No photon-generation or spin-flip would take place if the initial spin state is  $|-\rangle$ .

Ideally, after one cooling cycle, the spin is fully polarized with the entropy mapped into the quantum channel, and the final density matrix becomes  $|-\rangle\langle-| \otimes (0.5|0\rangle\langle 0| + 0.5|1\rangle\langle 1|)$ , where  $|n\rangle$  is the  $n$ -photon waveguide state. This is an idealization of the single-shot initialization of a spin qubit in a QD. In reality, the single-shot initialization is subject to errors due to the spontaneous emission of photons into free space, by which the trion state may relax to either spin state depending on the polarization of the emitted free-space photon, while the cavity photon couples only the transition to the target spin state.

The whole system under the optical control is described by the Hamiltonian

$$\begin{aligned} \hat{H} \equiv & \Omega_C \hat{a}^\dagger \hat{a} \pm \frac{\omega_c}{2} |\pm\rangle\langle\pm| + \Omega_T |T\pm\rangle\langle T\pm| + (g_{\text{cav}} |T\pm\rangle\langle\mp| \hat{a} + \text{H.c}) \\ & + [\chi_t(t) \mathbf{e}_t + \chi_p(t) \mathbf{e}_p] \cdot \mathbf{e}_X (|T\pm\rangle\langle\mp| + r_C \hat{a}^\dagger) + \text{H.c} \\ & + [\chi_t(t) \mathbf{e}_t + \chi_p(t) \mathbf{e}_p] \cdot \mathbf{e}_Y |T\pm\rangle\langle\pm| + \text{H.c}, \end{aligned} \quad (21)$$

where  $\hat{a}$  is the cavity mode annihilation operator,  $\Omega_C$  is the cavity mode frequency,  $\Omega_T$  is the bare trion state frequency,  $\omega_c$  is the electron Zeeman splitting,  $g_{\text{cav}}$  is the coupling between the cavity and the QD,  $\chi_p$  is the Rabi frequency of AC Stark pulses with polarizations  $\mathbf{e}_p$ ,  $\chi_t$  is the Rabi frequency of the pump pulse with polarization  $\mathbf{e}_t$ , and  $r_C$  is the strength of the direct coupling between the light pulse and the cavity mode (relative to the coupling to the trion state).

The dynamics in the cavity-dot system is rather complicated and some attention should be paid to the designing of the controlling pulses. To bring the trion state into the resonance with the cavity mode and to maintain the resonance, the AC Stark pulse is designed to have an almost square profile. Also, the switch-on and off of the pulse should be made smooth enough to avoid non-adiabatic excitation of the trion states from the target spin state. We choose the pulse to be of the profile

$$\chi_p(t) = \chi_p e^{-i\Omega_p t} \left[ \text{erf}(\sigma_p(t - t_1)) - \text{erf}(\sigma_p(t - t_2)) \right], \quad (22)$$

[see Fig. 28 (a)]. As the AC Stark pulse maintains the resonant cavity-dot coupling which facilitates the photon escape to the quantum channel, the trion state relaxes very fast (on the time-scale of  $g_{\text{cav}}^{-1}$  and  $\gamma^{-1}$ ,  $\sim 10$  ps). The flipping pulse should be a  $\pi$ -pulse for Rabi rotation between  $|+\rangle$  and  $|T+\rangle$ . Due to the dynamical nature of the states (dressed by the AC Stark pulse) and the rather small polariton splitting ( $\sim 0.1$  meV), a perfect  $\pi$ -rotation requires an extremely long pulse. In principle, a full excitation of the spin up state to the polariton states could be made much faster by pulse shaping. One of such pulse shaping is to use geometrical control of the transition which is robust against uncertainty of the polariton frequencies. The geometrical control is realized by using a chirped pulse as  $\chi_t(t) = \chi_t e^{-i\phi(t) - i\Omega_t t} \text{sech}(\sigma_t(t - t_i))$  with the phase sweeping rate  $\dot{\phi}(t) = -\sigma_c \tanh(\sigma_t(t - t_i))$  [314]. The frequency of the pulse now will sweep from  $\sigma_c$  above  $\Omega_t$  to  $\sigma_c$  below and the sweeping

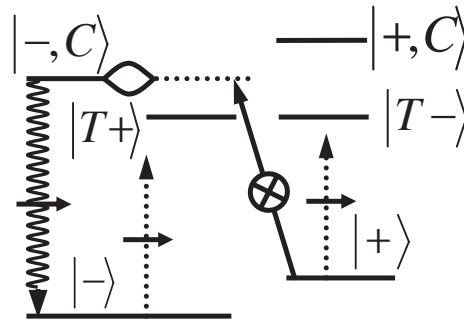


FIG. 26. Basic optical processes for initializing a spin by controlled cavity QED. The dotted, solid, and wavy arrows represent the AC Stark pulse (X-polarized), the tipping pulse (Y-polarized), and the spontaneous emission, respectively.



range  $[\Omega_t - \sigma_c, \Omega_t + \sigma_c]$  covers both of the trion-polariton states. The initial spin state  $|+\rangle$  will be brought adiabatically into a superposition of the two polariton states, which relaxes rapidly to the target spin state  $|-\rangle$ . Such a geometrical flip can also tolerate to some degree laser fluctuations and uncertainty in the dipole moment, transition energy, and selection rules.

The cooling process is simulated by numerically solving the master equation of the dot-cavity system

$$\partial_t \hat{\rho} = -i[\hat{H}, \hat{\rho}] - \frac{\gamma + \gamma'}{2} \mathcal{L}_{\hat{a}} \hat{\rho} - \frac{\Gamma}{2} \sum_{s,s'=\pm} \mathcal{L}_{|s\rangle\langle T s'|} \hat{\rho}, \quad (23)$$

where  $\mathcal{L}_{\hat{a}} \hat{\rho} \equiv 2\hat{a}\hat{\rho}\hat{a}^\dagger - \hat{a}^\dagger\hat{a}\hat{\rho} - \hat{\rho}\hat{a}^\dagger\hat{a}$  denotes a Lindblad super-operator,  $\gamma$  is the cavity-waveguide escape rate,  $\gamma'$  is the cavity-free-space loss rate,  $\Gamma$  is the trion decay rate due to spontaneous emission into free-space. The multi-photon cavity states were included in the numerical calculation, as they renormalize the AC Stark shift (the real excitation of multi-photon states is negligible due to the off-resonance condition). Inclusion of up to 3-photon states was found sufficient to obtain converged results.

We test the cooling efficiency with a set of realistic parameters [120]. The Zeeman splitting  $\omega_c = 1$  meV,  $\gamma = 0.2$  meV,  $\gamma' = 0.045$   $\mu$ eV (corresponding to an intrinsic  $Q$ -factor  $\sim 3 \times 10^7$ ), the dot-cavity coupling  $g_{\text{cav}} = 0.1$  meV, the cavity-trion detuning  $\Omega_C - \Omega_T - \omega_L/2 = 0.5$  meV,  $\Gamma = 1$   $\mu$ eV, and  $r_C = 0.3$ . For the parameters given above, the trion state  $|T+\rangle$  and the cavity state  $|-, C\rangle$  are brought into resonance when the AC Stark pulse strength ( $2\chi_p$ ) is maintained at 1.21 meV. Maintaining the resonance for  $t_2 - t_1 = 70$  ps is found sufficient for the total dissipation of the photon. The spectral width of the AC Stark shift pulse ( $\sigma_p = 0.354$  meV) is set much smaller than the detuning ( $\Omega_T + \omega_L/2 - \Omega_p = 5.5$  meV), so that the excitation due to non-adiabatic switch-on and off is negligible. The flipping pump pulse has a frequency sweep range of  $\sigma_c = 0.4$  meV, strength  $\chi_t = 0.2$  meV, and duration  $1/\sigma_t = 6.58$  ps. The spin state  $|+\rangle$  is flipped to the polariton states with negligible error.

Figure 28 (b) shows that a single cooling cycle completed within 80 ps produces an almost 100% polarized spin from a maximally mixed state. The density matrix at the end of the cycle is  $\hat{\rho} = 0.9945|-\rangle\langle -| + 0.0040|+\rangle\langle +| + \hat{\rho}_{\text{err}}$ , where  $\hat{\rho}_{\text{err}}$  is the probability ( $\approx 0.15\%$ ) of the system remaining in the trion states which results mainly from the non-adiabatic switching of the AC Stark pulse. The extra error ( $\approx 0.4\%$ ) comes mainly from the decay of the trion with photon emission into free space.

## B. Initialization by entropy dump to phonon baths

The phonon bath in a QD is often taken as a source of the qubit decoherence, but it can also be used as a resource for ultrafast cooling. The electronic energy levels in QDs are discrete, it has been argued that the phonon emission would be much suppressed due to the lack of available final states fulfilling the energy conservation [327]. This so-called phonon bottleneck effect, because of its importance in QD lasers and detectors, has been extensively studied both in experiments and in theories. Nonetheless, experiments have established various mechanisms for rapid relaxation of electrons from excited states to the ground states, such as the Auger-process and the multi-phonon process [328]. The observed relaxation time varies from tens of picoseconds to a few picoseconds [329, 330]. The spin relaxation, especially for holes due to the large spin-orbit coupling, always accompanies with the energy relaxation, for the mixing in the excited states is much stronger than in the ground states. Thus we can use the phonon emission as fast entropy dumping channel for an electron spin in a QD.

A cycle of the spin initialization is illustrated in the inset of Fig. 29:

1. A circularly polarized laser pulse resonantly pumps the electron states to an excited trion state.
2. The excited trion state relaxes rapidly to the ground trion states  $|\uparrow\uparrow\uparrow\rangle$  and  $|\uparrow\downarrow\downarrow\rangle$ . During the relaxation, the hole spin is not conserved due to the strong heavy-light hole mixing in the excited state, and without loss of generality we assume the rate is the same for the relaxation to the two ground trion states.

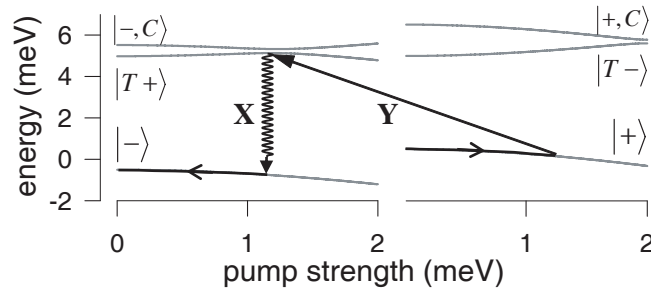


FIG. 27. (Extracted from Ref. [120]) A quantum version of the reverse Carnot cycle for spin qubit initialization in a QD. The grey curves are the energies of different states versus the Rabi frequency of the AC Stark pulse, in the rotating frame.

3. To deplete the population of one of the ground trion states, a circularly polarized laser pulse is applied to resonantly couple, e.g., the trion state  $|\uparrow\downarrow\downarrow\rangle$  to the electron spin state  $|\uparrow\rangle$ .
4. After a period of pumping and relaxation, the population will be accumulated to the trion state  $|\uparrow\downarrow\uparrow\rangle$ , and, thus, an ultrafast  $\pi$ -pulse can be applied to flip the trion state into a pure electron spin state.

The most time-consuming step of this laser cooling process is the pump and relaxation processes which is limited by the carrier relaxation rate and the pump strength. Care should be taken to avoid the population being trapped in some dark state which could be possible in the strongly driven multi-level system (similar to the electromagnetically induced transparency effect). Fig. 29 shows a typical spin initialization cycle in which the spin is pumped from a fully mixed state to a nearly fully polarized state in 120 ps (the polarization at the end of the cycle is about 97%), where  $\rho_3(t)$  is the population stored in the ground trion state  $|\uparrow\downarrow\uparrow\rangle$ , and  $P(t)$  is the polarization of the electron spin. The pump strength for the excited and ground trion states has been set to be 2 meV and 0.5 meV, respectively, the carrier relaxation time is 2 ps, and the spontaneous emission time is 1 ns. The  $\pi$ -pulse flipping the trion state into the spin state is chirped for optimized performance.

The phonon baths offer an alternative solution of ultrafast spin initialization with comparable speed to a photon bath enhanced by cavity QED. The real excitation of the excited electron and hole states, however, could cause some complications. One such issue is the trapping of electrons and holes in the dark states, which cause the loss of a spin qubit. And in fluctuation QDs, it is not likely the excited state energy is high enough for LO phonon emission.

## VI. QUANTUM NON-DEMOLITION MEASUREMENT OF SPIN QUBITS

The result of a quantum algorithm is obtained by quantum measurement of specific qubits. To diagnose the errors generated in quantum error correction, quantum measurement is also needed.

In current single-spin experiments in QDs [79, 256, 273, 326, 331–333] and in diamond color centers [88], the measurement is usually achieved by cycling read of the spins, which amounts to time-ensemble measurement. Remarkably, efficiency enhancement in measurement of NV center spins in diamond has been made using ancillary nuclear spin qubits [266, 334], but the single-shot measurement still remains illusive.

Eventually, single-shot measurement of quantum registers is demanded for scalable quantum computation for large-scale problems. In Appendix C, we show that quantum non-demolition (QND) measurement, even with certain errors, may be converted to a single-shot measurement and thus is scalable. To realize single-shot measurement, the crucial issue is how to enhance the coupling between the probe (photons, e.g.) and the spin qubits. Below we provide a possible solution of using cavity QED, which may be implemented in-situ in a quantum network (discussed in Sec.VII). The discussion is based on QD cavity-QED systems, but may be readily extended to NV centers where cavity-QED have been also demonstrated [260].

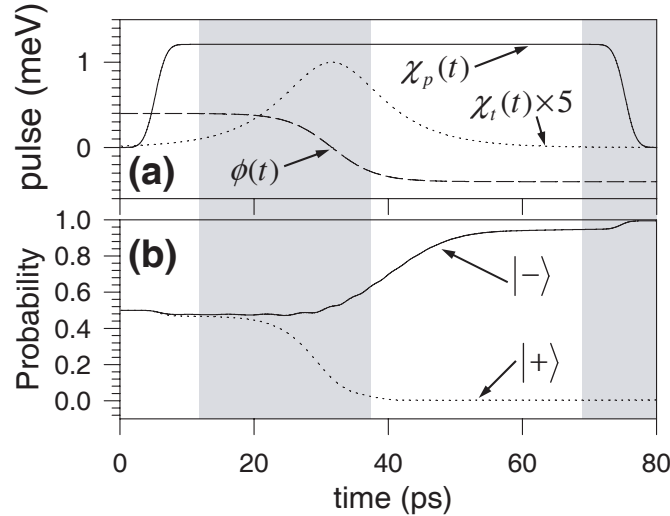


FIG. 28. (Extracted from Ref. [120]) (a) The Rabi frequencies of the AC Stark pulse and the tipping pulse (amplified by a factor 5), and the sweeping frequency of the tipping pulse. (b) Probabilities of spin down and up. Different steps of the cooling cycle, indicated by ①-④, are distinguished by shadowed areas.

### A. Scalability of quantum measurement in quantum computation

In quantum computation (such as in Shor’s algorithm [1, 172]), the quantum register could be in a superposition state right before the measurement  $|\Psi\rangle = \sum_x C_x|x\rangle$ , where  $|x\rangle \equiv |x_1, x_2, \dots, x_N\rangle$  is a computational basis state for the  $N$ -qubit register. The measurement should be in the computational basis which returns any  $|x\rangle$  contained in the superposition and the computation result is derived from the measured  $x$ . If an algorithm requires the measurement of the wavefunction  $C_x$ , i.e., the tomography of the quantum state, it would be an analog computation instead of a digital one, and much worse, it would not be scalable as the number of measurements would increase exponentially with the number of qubits in the register to be measured [335]. Such measurements are ensemble measurements.

A point we would like to put forward here about the scalability of quantum measurement in quantum computation is that an ensemble measurement is not scalable in the sense that the size of the ensemble would increase exponentially with the problem size (defined as the number of qubits registering the computation result involving a quantum measurement) [120]. It has been well-known that an ensemble quantum computation is not scalable if the qubits cannot be initialized to a pure state [336]. The issue of scalability associated with the ensemble measurement [120], however, has received less attention in spite of its importance in quantum computation. This problem is briefly explained below, and more detailed discussion is given in Appendix C.

First we notice that the uncorrelated ensemble measurement cannot be used to read out the quantum register in general algorithms (especially for those terminating in superposition states such as Shor’s algorithm). In an uncorrelated measurement, the spins are measured independently. Thus, in general which basis states are in the superposition cannot be deduced from the measured result. For example, the superposition state  $|000\rangle + |111\rangle$  will give the same uncorrelated measurement result as the state  $|000\rangle + |011\rangle + |101\rangle + |110\rangle$ . In some algorithms such as Shor’s algorithm for factorization, the number of basis states in the superposition may increase exponentially with the number of qubits, thus the number of possible superposition states yielding the same uncorrelated measurement result would increase exponentially with the number of qubits measured. So the quantum measurement has to be a correlated one (e.g., the photon counting should be in coincidence) to be scalable. If a coincidence measurement is a destructive one, the procedure has to be run from the very beginning in each repetition, and the superposition state can collapse into any possible  $|x\rangle$ , which is in general different from one cycle to another. To have a certain  $x$  to be measured at least twice for the sake of confidence, the number of repetitions to be performed should be in the order of the number of basis states in the superposition, which again could be an exponential function of the problem size. In conclusion, the enhancement of signal-background contrast by ensemble quantum computation is not a scalable solution.

In realistic cases, the signal of a single-shot measurement of a single quantum object is usually too weak to be distinguished from noise. Thus the signals are to be amplified either by simultaneously measuring a large number of identical “quantum computers” running the same quantum program or by repeating the quantum program under identical conditions for a large number of times. This renders the quantum computation to be an ensemble one and hence not scalable.

Using ensemble measurement as a solution to the detection efficiency problem has been applied in various systems, including nuclear spins in liquid-phase NMR [336] or solid-state NMR [62]. Here we consider quantum computing with optically controlled spins. The spin-dependent absorption (or other optical methods such as spin-dependent scattering and Faraday rotation) may be used to measure a single spin in a QD, in which a probe pulse resonant with the spin-trion transition in a QD measures

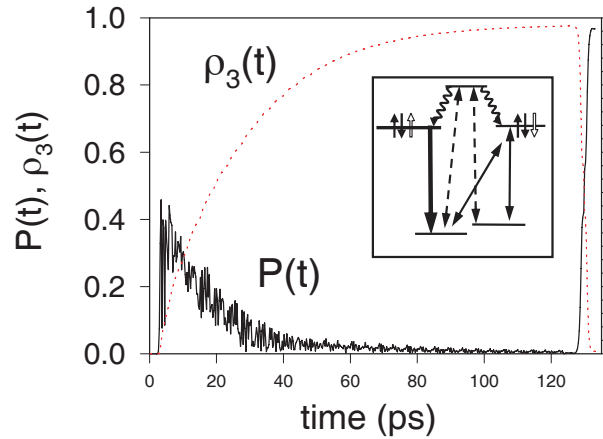


FIG. 29. The numerical simulation of a typical initialization cycle using phonon emission from excited trion states. Inset: Schematics for the spin initialization process.

the spin in the computational basis by detecting whether or not a single photon of the probe pulse has been absorbed. To measure a register with many qubits, the probe should be composed of many pulses in which each pulse addresses a QD individually by spatial and spectral resolution. In practice, the interaction between the probe pulse and a single spin is very weak, and also photon collection and detection efficiency is less than one, so the information obtained about a spin is on the average much less than one bit. The probe measurement has to be repeated for many times to accumulate statistical confidence in the measured result (or signal-to-noise ratio). Considering the fact that the probe process is destructive to the spin state (since a trion state excited by the probe pulse may return to either spin state regardless of the original spin state), the repetition has to be run from the very beginning of the quantum computation which prepares the quantum computer to the same superposition state. This makes the quantum computation an ensemble one, which in general is not scalable.

Nonetheless, the ensemble measurement could still be useful in demonstrating quantum algorithms for small-size problems. For instance, as will be shown later, to demonstrate Shor's algorithm for factorizing 15 by optical control of electron spins in QDs, the program would be completed in less than a few ns, and the number of computational basis states in the superposition is less than 10. A commercial Ti-Sapphire pulse laser with repetition rate of about 100 MHz could be used to carry out an ensemble of repeated running and measurement in a reasonably short time in a pump-probe configuration, where the initialization and gate control are viewed as a single complex pump pulse and the probe pulse is composed of many frequency components (and detected in multi-channels.)

### B. Quantum non-demolition measurement via cavity quantum electrodynamics

In essence, the realization of an efficient single-shot quantum measurement involves two key elements: rapid quantum state entanglement of the target qubit (here a spin in a QD) with a detectable information carrier (such as a photon), and efficient and faithful collection of the information carrier (such as by a photon detector with a high efficiency and a low dark count rate). Errors in the measurement, due to the efficiency or dark count problems, e.g., can not be fully eliminated. Thus cycling of single-shot measurement is required to accumulate statistical confidence. As discussed in Appendix C, the cycling of single-shot measurement is scalable when the measurement is a quantum non-demolition (QND) one, i.e., the qubit state after the measurement is (ideally) an eigenstate in the measurement basis corresponding to the measurement output.

The QND measurement being rapid is an essential element in the following sense: The cycling of measurement has to be completed in a time much shorter than the qubit is significantly disturbed by the environment. So we should look for a rapid quantum information transfer between the spin qubit and a medium to be detected. An ideal medium is photons. The cavity-enhanced entropy dumping in the ultrafast initialization is indeed a rapid information transfer (but there the information has been viewed as noise). Thus the ultrafast spin initialization and rapid QND may be integrated in the same micro-photon structure [120].

To ensure efficient detection of the transferred quantum information, the photons escaped from the cavity should be directed into a quantum channel, unlike in the initialization process where it does not matter which direction the dumped entropy flows. To realize such a directional information flow, a waveguide could be fabricated in the proximity of the cavity, and the waveguide may be coupled to a fiber which conducts the photon to a detector [295–301].

The optical control of the cavity-QED for a rapid measurement is similar to that for the ultrafast initialization [120]. But to enable measurement cycling, the measurement should be non-destructive, i.e., the spin basis state should return back to its initial state after a cycle of measurement, with close to unity probability. Thus we need to switch the polarizations of the tipping and the AC Stark pulses from  $(Y, X)$  to  $(X, Y)$ , respectively. The energy diagram with optical transitions indicated is shown in Fig. 30. A measurement cycle may be processed in four basic steps (see Fig. 31):

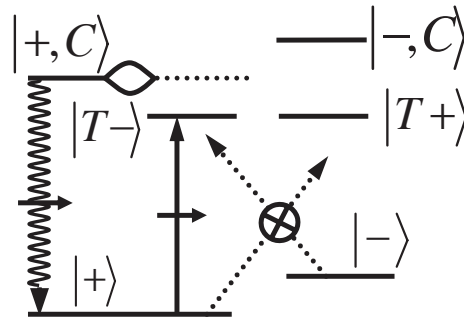


FIG. 30. Basic optical processes for QND measurement of a spin by controlled cavity QED. The dotted, solid, and wavy arrows represent the AC Stark pulse ( $Y$ -polarized), the tipping pulse ( $X$ -polarized), and the spontaneous emission, respectively.

1. An  $X$ -polarized tipping pulse flips the spin state  $|+\rangle$  to the trion state  $|T-\rangle$ .
2. A  $Y$ -polarized AC Stark pulse adiabatically switched on drives the trion state into resonance with the cavity state  $|+, C\rangle$ .
3. The trion state resonantly tunnels into the cavity state and relaxes rapidly back to the spin state  $|+\rangle$ , leaving a photon emitted into the quantum channel.
4. The AC Stark pulse is adiabatically switched off.

Suppose that the spin state to be measured is  $\alpha|+\rangle + \beta|-\rangle$  and the channel is initially in the vacuum state  $|0\rangle$ . An ideal measurement process will transform the system into the entangled state  $\alpha|+\rangle|1\rangle + \beta|-\rangle|0\rangle$ , so that the detection of the photon projects the electron into a spin basis state, providing a QND measurement of the spin. Note that the pulse timing for measurement is different from that for cooling [cf. Fig 28 (a) and Fig. 32 (a)]. In the measurement cycle, the flipping pulse need not be chirped, since here the Rabi flop occurs between stationary energy levels and the transition between the spin state and the trion is well separated in frequency from the cavity mode. Instead, a simple Gaussian  $\pi$  pulse  $\chi_t(t) = \chi_t e^{-\sigma_t^2(t-t_0)^2/2 - i\Omega_t t}$  may be used. The AC Stark pulse is chosen  $Y$ -polarized to avoid direct excitation of the cavity mode.

Numerically simulation is done to check the efficiency of the measurement cycle [120]. Since the initialization and the QND measurement are supposed to be operated via the same photonic structure, the simulation is done with the same physical structure as that in Fig. 28. The number of photons emitted into the waveguide is calculated with  $\partial_t n = \gamma \langle \hat{a}^\dagger \hat{a} \rangle$ . The tipping and the AC Stark pulses are set such that  $1/\sigma_t = 2.19$  ps,  $\chi_t = 0.192$  meV,  $\Omega_t = \Omega_T - \omega_L/2$ ,  $\sigma_p = 0.707$  meV,  $2\chi_p = 2.08$  meV,  $\Omega_T + \omega_L/2 - \Omega_p = 5.5$  meV, and the duration of the pump pulse  $t_2 - t_1 = 50$  ps. After a single cycle of measurement, an initial state  $\hat{\rho}_0 = |+\rangle\langle+|$  results in the final state  $\hat{\rho}_1 = 0.0161|-\rangle\langle-| + 0.9824|+\rangle\langle+| + \hat{\rho}_{\text{err}}$  with the number of photon emitted into the waveguide  $n = 0.9806$  [see Fig. 32 (b)], while an initial state  $\hat{\rho}_0 = |-\rangle\langle-|$  results in the final state  $\hat{\rho}_1 = 0.9955|-\rangle\langle-| + 0.0040|+\rangle\langle+| + \hat{\rho}_{\text{err}}$  with  $n = 0.0015$  (not shown). The photon emitted into the waveguide can be detected with high efficiency. If the detector has a zero dark-count rate and an efficiency of 50% [337], the POVM (positive operator-valued measures [172], see Appendix C for more discussions) for the measurement process can be defined as

$$\hat{P}_- = 0.9992|-\rangle\langle-| + 0.5097|+\rangle\langle+|, \quad (24a)$$

$$\hat{P}_+ = 0.0008|-\rangle\langle-| + 0.4903|+\rangle\langle+|, \quad (24b)$$

for a non-click or click event, respectively. Within 5 measurement cycles, e.g, the spin state is measured with accuracy higher than 97%, and the back-action noise to the spin is less than 10%, while the time duration is less than 0.4 ns, much shorter than the spin decoherence time.

The QND measurement of single spins thus can be completed within 100 ps, and the high-efficiency of collecting and detecting photons propagating in waveguides enables a near unity accuracy by repeating the single-shot measurement for only a few times. The measurement is still subject to the problem of less than unity efficiency as well as back-action noise. As discussed in Appendix C, quantum gates and error tolerating coding can be combined to achieve a sufficiently faithful measurement of a qubit without rewinding a quantum computing program.

## VII. NETWORKING LOCAL NODES

In section III B, we have introduced the dot-cavity-waveguide coupled structure for distributed quantum information processing. Quantum nodes are formed by clusters of singly charged QDs with electron spins as carriers of stationery qubits. Single

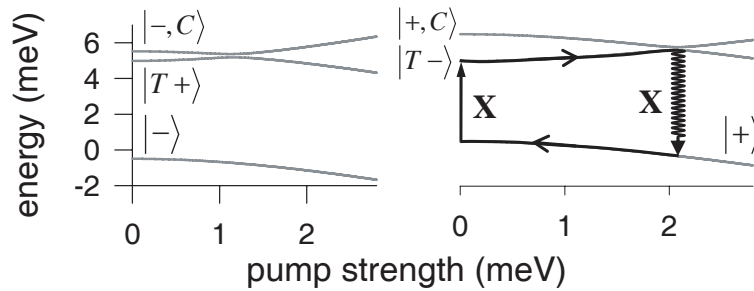


FIG. 31. (Extracted from Ref. [120]) Detailed optical process for the measurement cycle. The grey curves are the energies of different states versus the Rabi frequency of the AC Stark pulse, in the rotating frame.

photons in optical waveguides or fibers can transport quantum information between distant nodes. Interfacing between single spins in QDs and single photons is made possible by the strong photon confinement in solid state micro-cavities.

The separation between quantum nodes on a single chip which can range from  $\sim \mu\text{m}$  to  $\sim \text{cm}$  allows parallel optical control, and intra-chip communication is realized by optical waveguides. Inter-chip communication is possible by wiring chips together with optical fibers [338–340]. For intra-chip communication and short distance inter-chip communication, the decoherence of the photon qubit is negligible [341–343]. Thus, it is possible and also highly desirable to perform inter-node operations in a deterministic way (to be contrasted with most quantum cryptography and linear optics quantum computation schemes based on projective measurement which renders the logical controls probabilistic). The key component is a quantum interface that allows the deterministic state transfer between spin and photon qubit.

The prototype quantum interface for this purpose was proposed by Cirac *et al.* [277]. It is composed of a cavity coupled to a three-level  $\Lambda$  system, illustrated in Fig. 33. The two ground states,  $|g\rangle$  and  $|e\rangle$ , of the three level system form the stationary qubit. State  $|g\rangle$  is coupled to the intermediate state  $|t\rangle$  by the cavity mode and  $|e\rangle$  to  $|t\rangle$  by the external laser field. Direct excitation of cavity by the external laser is assumed absent. Through the imperfect mirror, the cavity is coupled to the electromagnetic continuum which forms a photonic channel. A Raman path from  $|e\rangle$  to  $|g\rangle$  through the intermediate state  $|t\rangle$  is thus formed. If the three level system is initially in state  $|e\rangle$ , an external laser pulse can bring it to state  $|t\rangle$  by a  $\pi$  rotation which relaxes to state  $|g\rangle$  by spontaneous emission of a cavity photon. The cavity photon then goes into the photonic channel forming a single photon wavepacket. If the three level system is initially in state  $|g\rangle$ , it will remain in this state provided the cavity is in its vacuum. The quantum state carried by the three-level system is thus mapped into the photon number subspace of the outgoing photon,

$$(C_g|g\rangle + C_e|e\rangle) \otimes |\text{vac}\rangle \rightarrow |g\rangle \otimes [C_g|\text{vac}\rangle + C_e|\alpha_{\text{out}}\rangle]. \quad (25)$$

where  $|\alpha\rangle$  denotes a single photon wavepacket in the photonic channel and  $|\text{vac}\rangle$  the channel vacuum. This process forms the basis for the sending function (i.e. the mapping from a stationary qubit to a flying qubit) of a quantum node. The receiving function is the mapping from a flying qubit to a stationary qubit and can be realized as the time reversal of a sending process,

$$|g\rangle \otimes (C_g|\text{vac}\rangle + C_e|\alpha_{\text{in}}\rangle) \rightarrow (C_g|g\rangle + C_e|e\rangle) \otimes |\text{vac}\rangle. \quad (26)$$

With the output of the sending node directed as the input of the receiving node (see Fig. 33), transfer of qubits between two distant nodes can be performed.

This quantum network by cavity QED was originally proposed for quantum computation with atomic systems [277]. Critical experimental steps towards realizing such a quantum interface in atom-cavity QED systems have been progressively demonstrated [153, 154, 344], including the initial demonstration of reversible state transfer between photons and atoms [345]. Via similar cavity-assisted Raman processes, schemes for mapping between motional states of single trapped atoms [346] or collective excitation of atomic ensembles [347] and the quantum states of single photons are also proposed.

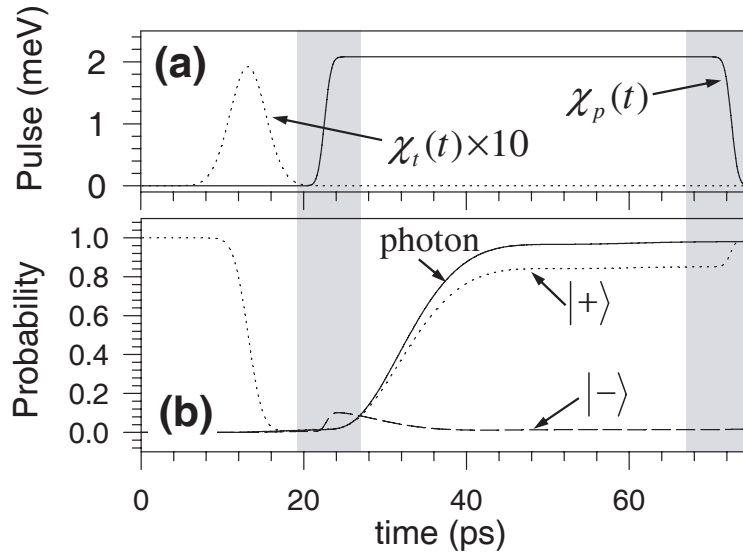


FIG. 32. (Extracted from Ref. [120]) (a) The Rabi frequencies of the AC Stark pulse and the tipping pulse (amplified by a factor 10). (b) Probabilities of spin down and up, and the number of waveguide photons, for a spin initially polarized up. Different steps of the cooling cycle, indicated by ①–④, are distinguished by shadowed areas.

For quantum computation with QD spins [63], deterministic quantum network control is indeed possible in the distributed structure discussed previously in section III B. In subsection VII A, we will first show how to realize such a prototype quantum interface between a QD electron spin and a photon mode in a waveguide/fiber. In subsection VII B, we will describe the exact solution to the interface dynamics between a spin qubit and a photon qubit in the prototype quantum node in the most general scenario. Control schemes based on the exact solution form the basis of a variety of inter-node operations in quantum networks as discussed in Sec. VII C. The issue of unavoidable inhomogeneity of solid-state quantum nodes is properly resolved with the exact interface solution. In subsection VII D, we study the effects of various sources of errors on the interface operations. A summary and outlook are given in subsection VII E.

### A. Dot-Cavity-Waveguide structure as spin-photon interface

Here we show how to implement a dot-cavity-waveguide coupled structure as a deterministic quantum interface for single spins in QDs and single photons in waveguides.

The coupled structure can be realized with any of the micro-cavity systems discussed in section III B. In Fig. 34(a), a QD sitting in the evanescence field of whispering gallery mode of a ring cavity is illustrated as an example. There are two essential requirements for such a coupled structure to be an efficient interface. First, the dot-cavity coupling must have a large Purcell factor, so that the QD optical transitions are dominantly coupled to the cavity field. Second, the leakage of the cavity photon into free space should be small as compared with the tunneling into the attached waveguide. If both conditions are fulfilled, the evolution through the desired quantum pathway, i.e. QD trion  $\leftrightarrow$  cavity photon  $\leftrightarrow$  waveguide photon, occurs on a much faster timescale than the leakage out of it [119, 120]. Lowering of the cavity  $Q$ -factor due to the coupling to the waveguide is part of the process and has no deleterious effects on the quantum operation. The cavity with the reduced  $Q$ -factor is *not* required to be in the strong coupling regime [119, 348, 349]. This will become clear when we discuss the control of this interface in the following subsections.

The qubit is represented by the two spin states  $|x-\rangle$  and  $|x+\rangle$  and spin manipulations are mediated by the two trion ground states  $|T-\rangle$  and  $|T+\rangle$  (see section II B). In the convention of the prototype quantum interface, the two spin states are also denoted here as  $|g\rangle$  and  $|e\rangle$  respectively, and the two trion states  $|T+\rangle$  and  $|T-\rangle$  as  $|t\rangle$  and  $|\bar{t}\rangle$ , respectively. While  $|g\rangle$  and  $|e\rangle$  have energies  $\omega_g$  and  $\omega_e$  in a static magnetic field normal to the optical axis of the dot (see Fig. 34(a)),  $|t\rangle$  and  $|\bar{t}\rangle$  typically have a much smaller energy splitting ( $\omega_t \approx \omega_{\bar{t}}$ ) in GaAs fluctuation dot because of its negligible in-plane  $g$ -factor of the heavy holes [200, 350], but a splitting comparable to the electron's in self-assembled InAs dot [257].

By design, the selected cavity mode of frequency  $\omega_c$  is  $X$ -polarized in the vicinity of the QD and a  $Y$ -polarized control laser of central frequency  $\omega_L$  and complex Rabi frequency  $\Omega(t)$  directly couples to the QD transitions [230, 308]. Therefore, by the selection rules shown in Fig. 34, the cavity field couples only to the straight transitions  $|g\rangle \rightarrow |t\rangle$  and  $|e\rangle \rightarrow |\bar{t}\rangle$ , and the controlling laser couples only to the cross transitions  $|g\rangle \rightarrow |\bar{t}\rangle$  and  $|e\rangle \rightarrow |t\rangle$ . The laser light and cavity mode satisfy the two-photon resonance condition:  $\omega_L + \omega_e = \omega_c + \omega_g$ . The Raman detuning  $\Delta \equiv \omega_t - \omega_L - \omega_e$  is also much smaller than the electron Zeeman splitting  $\omega_e - \omega_g$ . Thus, by the Zeeman splitting and the selection rules, the trion state  $|\bar{t}\rangle$  is off-resonance to the laser light and the cavity mode [shown by dashed lines in the Fig. 34(c)].

At a sending node, the Raman process consists in first the laser field exciting the spin state  $|e, 0\rangle$  to the trion state  $|t, 0\rangle$ , then the trion state resonantly coupled to the cavity state  $|g, 1\rangle$  which finally is rotated to the spin state  $|g, 0\rangle$  forming a photon wave packet in the waveguide (here 0 and 1 denote the number of photons in the single cavity mode). The receiving mode is just the time-reversed process. Undesirable dynamics involving the state  $|\bar{t}\rangle$  is eliminated by making the Zeeman splitting sufficiently larger than the cavity-dot coupling and the Rabi frequency. The resultant optical process is the cavity-assisted Raman process in a  $\Lambda$ -type three-level system as required by the prototype quantum interface (see Fig. 33). Numerical calculations including the

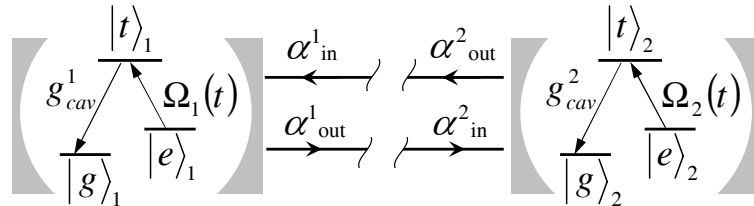


FIG. 33. Illustration of state transfer in a quantum network. The node is composed of a cavity coupled to a three-level  $\Lambda$  system. The two ground states  $|g\rangle$  and  $|e\rangle$  of the three level systems form the Hilbert space for the stationary qubits. State  $|g\rangle$  is coupled to the intermediate  $|t\rangle$  by the cavity mode with strength  $g_{cav}$  and  $|e\rangle$  to  $|t\rangle$  by a classical light with Rabi frequency  $\Omega(t)$ . Direct excitation of cavities by the classical light is assumed absent. The cavities themselves are coupled to the outside continuum which forms a photonic channel. Two nodes are connected by the photonic channel in the following way: the output of node 1 is directed to node 2 as its input and vice versa.

non-resonance transitions and realistic decoherence have been performed and high fidelity of desired operations at the quantum interface is demonstrated (see subsection VIID for details).

### B. Control of spin-photon interface

In the previous subsection, we have shown that the dot-cavity-waveguide coupled structure could be an efficient solid state realization of the prototype quantum interface. In order for such quantum interface to be suitable for a quantum network, proper control schemes are required.

The difficulty in realizing the network lies in the receiving end. Instead of being trapped at the quantum node, the single photon pulse can be reflected by the cavity unless the pulse shape of the classic control laser matches the single photon wavepacket exactly, known as quantum impedance matching [347, 351]. One way to deal with this requirement was provided in [277]. The central idea is that if a laser pulse can be found for generation of an outgoing photon wavepacket with time reversal symmetry, by using this laser control at the sending node and its time reversal at the receiving node, the time reversal symmetry will guarantee the photon wavepacket to be completely trapped at the receiving node. A solution for such a laser control pulse was given in [277].

The time reversal symmetric control scheme requires the sending and receiving quantum nodes to be identical in terms of optical transition frequencies and strength of coupling between the components. Unfortunately, such requirement is practically impossible to fulfill in solid state systems since the fabricated QDs and micro-cavities naturally have shape variations and size fluctuations, leading to inhomogeneity in optical frequencies. The cavity field has a highly non-uniform profile and thus cavity-dot coupling differ from dot to dot. For realization of a quantum network with solid state structures, control schemes beyond the time symmetric one is required. In the sending function, it is straightforward to solve for the outgoing single photon wavepacket  $\alpha(t)$  if we know the form of the laser control pulse  $\Omega(t)$ . The key problem is the inverse functional relation  $\Omega(t) = \mathcal{F}^{-1}[\alpha(t)]$ , i.e., given an arbitrary single photon wavepacket  $\alpha(t)$ , the exact laser pulse that can generate this single photon wavepacket at a sending node, or completely trap it at a receiving node. Knowing this relation allows the sending and receiving operations to be separately addressed and hence the construction of a quantum network with heterogeneous quantum nodes.

Solutions to  $\Omega(t) = \mathcal{F}^{-1}[\alpha(t)]$  were first given in the adiabatic approximations [347, 351]. Exact solutions in the non-adiabatic form were later found by the authors [119, 348], as briefly described below.

The Hamiltonian including the interaction between the single-mode cavity and the three-level system and the channel contin-

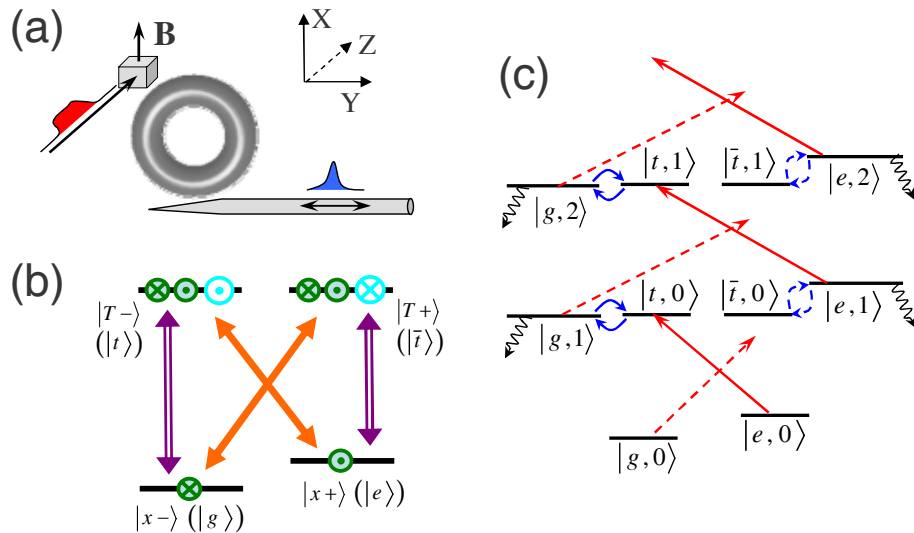


FIG. 34. (a) A high- $Q$  micro-ring coupling a ‘tapered’ waveguide and a singly charged QD. (b) Optical selection rules in the basis where spins are quantize along the field ( $x$ ) direction. The hollow two-headed arrow denotes  $X$ -polarized light and the solid arrow denotes  $Y$ -polarized light. (c) The level diagram and optical process. In  $|s,n\rangle$ ,  $s = g, e, t$  or  $\bar{t}$  denotes an electronic state in the dot and  $n$  denotes the number of photons in the single cavity mode. Straight, curved, and wavy arrows represent the laser excitation, dot-cavity coupling, and cavity-fiber tunneling, respectively. The resonant and off-resonance processes are represented by solid and dashed lines, respectively.



uum is,

$$H = \omega_c a^\dagger a + \omega_t |t\rangle \langle t| + \omega_e |e\rangle \langle e| + \int_0^\infty d\omega \omega b_\omega^\dagger b_\omega + g_{\text{cav}} (i |t\rangle \langle g| a + \text{H.c.}) + \frac{1}{2} \left[ i\Omega(t) e^{-i\omega_L t} |t\rangle \langle e| + \text{H.c.} \right] + \int_0^\infty d\omega \left( i\sqrt{\gamma/2\pi} b_\omega^\dagger a + \text{H.c.} \right), \quad (27)$$

where  $b_\omega$  is the annihilation operator for the mode of frequency  $\omega$  in the channel continuum and  $a$  is the annihilation operator for the cavity mode. The energy of state  $|g\rangle$  is set as zero. The  $|g\rangle \rightarrow |t\rangle$  transition is coupled to the cavity mode with strength  $g_{\text{cav}}$ . The  $|e\rangle \rightarrow |t\rangle$  transition is coupled by the external control laser of time-dependent Rabi frequency  $\Omega(t)$  and central frequency  $\omega_L$ . The coupling of the cavity mode to the channel continuum is assumed constant:  $\sqrt{\gamma/2\pi}$ . An ideal situation is assumed neglecting photon leakage into free space through intermediate state  $|t\rangle$  or the cavity sidewall.

We note that the system described by this Hamiltonian, under the laser excitation and the cavity-dot and cavity-channel interaction, has two invariant Hilbert subspaces, with the basis  $\{|g, 0\rangle |\text{vac}\rangle\}$  and  $\{|e, 0\rangle |\text{vac}\rangle, |t, 0\rangle |\text{vac}\rangle, |g, 1\rangle |\text{vac}\rangle, |g, 0\rangle |\omega\rangle\}$  (where in  $|s, n\rangle$ ,  $s = g, e$  or  $t$  denotes the state of the three-level system,  $n$  denotes the number of photons in the cavity mode, and  $|\omega\rangle$  denotes the one-photon Fock state of the channel mode of frequency  $\omega$ ). So the evolution of the system can be generally described by the state  $C_g |g, 0\rangle |\text{vac}\rangle + C_e |\Psi^e(t)\rangle$  in the interaction picture, where

$$|\Psi^e(t)\rangle = \beta_e(t) |e, 0\rangle |\text{vac}\rangle + \beta_t(t) |t, 0\rangle |\text{vac}\rangle + \beta_c(t) |g, 1\rangle |\text{vac}\rangle + \int_0^\infty d\omega \alpha_\omega(t) |g, 0\rangle |\omega\rangle. \quad (28)$$

The time evolution of the amplitudes in the interaction picture is described by the following Schrödinger equations,

$$\dot{\beta}_e = -\frac{\Omega^*}{2} e^{-i(\omega_t - \omega_L - \omega_e)t} \beta_t, \quad (29a)$$

$$\dot{\beta}_t = g_{\text{cav}} e^{i(\omega_t - \omega_c)t} \beta_c + \frac{\Omega}{2} e^{i(\omega_t - \omega_L - \omega_e)t} \beta_e, \quad (29b)$$

$$\dot{\beta}_c = -g_{\text{cav}} e^{-i(\omega_t - \omega_c)t} \beta_t - \sqrt{\gamma} \alpha_{\text{in}}(t) - \frac{\gamma}{2} \beta_c \quad (29c)$$

$$= -g_{\text{cav}} e^{-i(\omega_t - \omega_c)t} \beta_t - \sqrt{\gamma} \alpha_{\text{out}}(t) + \frac{\gamma}{2} \beta_c, \quad (29d)$$

where  $\alpha_{\text{in}}(t) \equiv \int d\omega \alpha_\omega(t_0) e^{-i(\omega - \omega_c)t} / \sqrt{2\pi}$  with  $t_0 \rightarrow -\infty$  and  $\alpha_{\text{out}}(t) \equiv \int d\omega \alpha_\omega(t_1) e^{-i(\omega - \omega_c)t} / \sqrt{2\pi}$  with  $t_1 \rightarrow +\infty$  can be regarded as the incoming and outgoing wavepacket of the photon in the quantum channel, respectively. From Eqs. (29c) and (29d), we note that evolution of  $\beta_c(t)$  is simply an instantaneous map of the difference between the input and output field in the photonic channel

$$\sqrt{\gamma} \beta_c(t) = \alpha_{\text{out}}(t) - \alpha_{\text{in}}(t). \quad (30)$$

$\beta_t(t)$  is also readily expressed in terms of  $\alpha_{\text{in}}(t)$  and  $\alpha_{\text{out}}(t)$  as,

$$\begin{aligned} \beta_t &= \frac{-\dot{\beta}_c - \sqrt{\gamma} \alpha_{\text{in}}(t) - \frac{\gamma}{2} \beta_c}{g_{\text{cav}}} e^{i(\omega_t - \omega_c)t} \\ &= \frac{-(\dot{\alpha}_{\text{out}} - \dot{\alpha}_{\text{in}}) / \sqrt{\gamma} - (\alpha_{\text{in}}(t) + \alpha_{\text{out}}(t)) \sqrt{\gamma} / 2}{g_{\text{cav}}} e^{i(\omega_t - \omega_c)t}. \end{aligned} \quad (31)$$

So as the amplitude of  $\beta_e(t)$ ,

$$\frac{d}{dt} |\beta_e|^2 = -\frac{d}{dt} |\beta_t|^2 + g_{\text{cav}} \left[ \beta_t^* \beta_t e^{-i(\omega_t - \omega_c)t} + \beta_c \beta_t^* e^{i(\omega_t - \omega_c)t} \right], \quad (32)$$

and the phase,

$$\begin{aligned} \frac{d}{dt} \arg(\beta_e) &= \frac{1}{2i} |\beta_e|^{-2} \left( \dot{\beta}_t \beta_t^* - \beta_t \dot{\beta}_t^* \right) \\ &\quad + \frac{g_{\text{cav}}}{2i} |\beta_e|^{-2} \left[ \beta_t \beta_c^* e^{-i(\omega_t - \omega_c)t} - \beta_c \beta_t^* e^{i(\omega_t - \omega_c)t} \right]. \end{aligned} \quad (33)$$

Finally, from Eq. (29b), the complex Rabi frequency of the laser pulse  $\Omega(t)$  can be expressed in terms of the amplitudes that have been solved above,

$$\Omega(t) = 2 \frac{\dot{\beta}_t - g_{\text{cav}} \beta_c}{\beta_e}. \quad (34)$$

Thus the desired operation, with  $\alpha_{\text{in}}(t)$  and  $\alpha_{\text{out}}(t)$  arbitrarily specified, can be generated on demand as long as the normalization condition of the wavefunction is not violated

$$\frac{d}{dt} (|\beta_e|^2 + |\beta_r|^2 + |\beta_c|^2) = |\alpha_{\text{in}}(t)|^2 - |\alpha_{\text{out}}(t)|^2. \quad (35)$$

The functions of this quantum interface can be classified into three types:

1. If there is no incoming photon, the quantum interface generates an outgoing photon wavepacket of a specified shape;
2. If there is an incoming photon wavepacket of a specified shape, it is completely trapped by the quantum interface so that there is non outgoing field;
3. If there is an incoming photon wavepacket of a specified shape, the quantum interface generates an outgoing photon wavepacket of another specified shape – a controlled scattering process.

The first two types of control form the basis for the quantum network operation. With control of the type III, the quantum interface can act as a controllable scatter or pulse shaper for single photon wavepackets. This control can also be considered as the combination of consecutive controls of type II and I. In the following subsection, we will discuss in more details how to implement the first two types of controls for a quantum network.

### C. Inter-node operations in a quantum network

The sending node of a quantum network is operated with control of type I. The initial conditions are:  $\alpha_{\text{in}}(t) = 0$ ,  $\beta_c(t_0) = 0$ ,  $\beta_e(t_0) = 1$  and  $\beta_r(t_0) = 0$ . The integral form of Eq. (35) becomes

$$|\beta_e|^2 = 1 - \sin^2 \theta \int_{t_0}^t |\tilde{\alpha}_{\text{out}}(\tau)|^2 d\tau - |\beta_c|^2 - |g_{\text{cav}}|^{-2} |\dot{\beta}_c + \gamma\beta_c/2|^2, \quad (36)$$

where  $\tilde{\alpha}_{\text{out}}$  is the normalized wavepacket of the emitted photon, and  $\sin^2 \theta$  is the average photon number. For a photon number and a pulse shape arbitrarily specified, the amplitude of the cavity mode is determined by Eq. (30) as  $\beta_c(t) = \sqrt{\gamma}\tilde{\alpha}_{\text{out}}(t) \sin \theta$ . If we pose the problem of finding the laser control pulse to produce a specified shape of the outgoing photon wavepacket, the fact that the right-hand side of Eq. (36) is positive requires the specified output pulse be sufficiently smooth, i.e., the pulse generation process be slower than the cavity-channel tunneling and the dot-cavity coupling rate (with time scales  $\gamma^{-1}$  and  $g_{\text{cav}}^{-1}$ , respectively). At the remote future time,  $t_1 \rightarrow +\infty$ , the photon emission process is completed, i.e.,  $\beta_c(t_1) = \dot{\beta}_c(t_1) = 0$ , so  $\beta_e(t_1) = e^{i\phi} \cos \theta$  with the controllable phase  $\phi$  given by Eq. (33). The general form of the photon generation process can be expressed as

$$\begin{aligned} & (C_g|g\rangle + C_e|e\rangle) \otimes |\text{vac}\rangle \\ & \xrightarrow{\Omega(t)} C_g|g\rangle \otimes |\text{vac}\rangle + C_e \left[ e^{i\phi} \cos \theta |e\rangle \otimes |\text{vac}\rangle + \sin \theta |g\rangle \otimes |\tilde{\alpha}_{\text{out}}\rangle \right]. \end{aligned} \quad (37)$$

A full Raman process corresponds to  $\theta = \pi/2$  and  $\beta_e(t_1) = 0$ , where Eq. (37) is reduced to,

$$(C_g|g\rangle + C_e|e\rangle) \otimes |\text{vac}\rangle \xrightarrow{\Omega(t)} |g\rangle \otimes (C_g|\text{vac}\rangle + C_e|\tilde{\alpha}_{\text{out}}\rangle), \quad (38)$$

which results in the mapping of the stationary qubit onto the flying qubit. If initially the three level system is entirely in state  $|e\rangle$ , this mapping operation can function as a deterministic generation of a single-photon wavepacket with any desired shape  $\tilde{\alpha}_{\text{out}}(t)$ . If the Raman cycle is controlled to be partially completed ( $\theta < \pi/2$ ), the state initially in  $|e\rangle \otimes |\text{vac}\rangle$  is transformed into an entangled state of the stationary spin and the flying photon

$$|e\rangle \otimes |\text{vac}\rangle \xrightarrow{\Omega(t)} e^{i\phi} \cos \theta |e\rangle \otimes |\text{vac}\rangle + \sin \theta |g\rangle \otimes |\tilde{\alpha}_{\text{out}}\rangle. \quad (39)$$

The entanglement entropy  $E = -\cos^2 \theta \log_2 \cos^2 \theta - \sin^2 \theta \log_2 \sin^2 \theta$  can be set at any value between 0 and 1 depending on the rotating angle  $\theta$ .

The receiving node is operated with control of type II, typically as a full Raman cycle, in the quantum network scheme. With the three level system initially on state  $|g\rangle$  and the incoming photon  $C_g|\text{vac}\rangle + C_e|\alpha_{\text{in}}(t)\rangle$ , the mapping transformation is,

$$|g\rangle \otimes (C_g|\text{vac}\rangle + C_e|\alpha_{\text{in}}\rangle) \xrightarrow{\Omega(t)} (C_g|g\rangle + C_e|e\rangle) \otimes |\text{vac}\rangle. \quad (40)$$

As in the sending process, the incoming photon pulse  $\alpha_{\text{in}}(t)$  can be arbitrarily specified, provided that it is smooth enough.

By combining the sending and receiving processes, the transfer of a qubit from one node to another can be easily implemented, with the outgoing photon from the sending node directed as the incoming photon for the receiving node. As the photonic channel is linear, two state-transfer operations with opposite directions can be performed in parallel, and qubits at the two nodes will be swapped. Swap operations can only be performed between nodes separated with sufficiently large distance so that photon traveling time in the channel is longer than the interface operation time.

If the operation at the sending node has been designed to produce an entangled state of the stationary and the flying qubit, the mapping process at the receiving node will just produce an entangled state of the two nodes by the transformation,

$$\begin{aligned} |e\rangle_1|g\rangle_2 \otimes |\text{vac}\rangle &\xrightarrow{\Omega_1(t)} e^{i\phi} \cos \theta |e\rangle_1|g\rangle_2 \otimes |\text{vac}\rangle + \sin \theta |g\rangle_1|g\rangle_2 \otimes |\tilde{\alpha}_{\text{out}}\rangle \\ &\xrightarrow{\Omega_2(t)} \left[ e^{i\phi} \cos \theta |e\rangle_1|g\rangle_2 + \sin \theta |g\rangle_1|e\rangle_2 \right] \otimes |\text{vac}\rangle. \end{aligned} \quad (41)$$

Non-local entanglement can thus be generated deterministically in the quantum network.

With the exact solutions for the interface dynamics, the sending and receiving functions can be separately addressed. This enables the construction of a quantum network with heterogeneous quantum nodes, which is essential for solid state realization. To illustrate this, we give below an exemplary control strategy. The control laser pulse at a sending node can have a general shape  $\Omega_1(t)e^{-i\omega_L^1 t}$  with the pulse area satisfying the specified rotation angle  $\theta$ . The outgoing single photon wavepacket has a definite shape  $\alpha_{\text{out}}^1(t)$  (in the rotating frame defined by frequency  $\omega_c^1$ ), determined by the laser control  $\Omega_1(t)$  and the parameters of the sending node  $g_{\text{cav}}^1$ ,  $\gamma_1$  and Raman detuning  $\Delta_1 \equiv \omega_t^1 - \omega_L^1 - \omega_e^1 = \omega_t^1 - \omega_c^1$ . Then we pose the problem of finding the optical control  $\Omega_2(t)e^{-i\omega_L^2 t}$  to trap the single photon wavepacket  $\alpha_{\text{in}}^2(t) \equiv \alpha_{\text{out}}^1(t)e^{i(\omega_c^2 - \omega_c^1)t}$  at the receiving node which may have a different set of parameters  $g_{\text{cav}}^2$ ,  $\gamma_2$ ,  $\omega_t^2$ ,  $\omega_e^2$  and  $\omega_c^2$ . From Eq. (36) and the discussion follows, it implies that the tolerance of the node inhomogeneity is determined by the node bandwidth, i.e. the dot-cavity coupling  $g_{\text{cav}}$  and dot-waveguide tunneling  $\gamma$ . Thus, a large dot-cavity coupling  $g_{\text{cav}}$  is essential. This tolerance was discussed more explicitly by Fattal *et al* in Ref. [349].

#### D. Operations with imperfections

In this subsection, we discuss the effects of various imperfections that may occur in a realistic quantum network and the corresponding mitigation.

##### 1. Intrinsic photon leakage into free space

The desired quantum evolution is through the pathway of trion - cavity photon - waveguide photon. The main causes of photon leakage out of this quantum pathway is through the trion decay by spontaneous emission and the cavity mode leakage other than the tunneling into the waveguide. The waveguide and fiber loss is negligible on the distance-scale of relevance for intra-chip communication and for inter-chip communications if the chips are distributed in a spatial range of  $\lesssim 10$  cm. As long as the photon leakage rate is much smaller than the bandwidth of the desired quantum pathway (determined by the dot-cavity coupling  $g_{\text{cav}}$  and the cavity-waveguide tunneling  $\gamma$ ), high fidelity operations can be expected. Typical trion decay rates in self-assembled QDs are  $\Gamma \sim \mu\text{eV}$  [229, 230], and the intrinsic loss rate of a high- $Q$  cavity (i.e. excluding coupling to the dot and the waveguide) can be potentially achieved at  $\gamma_0 \gtrsim 0.1 \mu\text{eV}$  (corresponding to a  $Q$ -factor  $\sim 10^7$ ) [282, 283]. The state-of-the-art dot-cavity coupling constant achieved is  $g_{\text{cav}} = 0.1 \text{ meV}$  [279, 284, 286], while the cavity-waveguide tunneling rate is controlled in design by the gap distance. Thus the bandwidth can be two orders larger than the leakage rate.

The simulation result of mapping a spin state to a flying photon wavepacket with the shape targeted as an asymmetric superposition of two sech-functions as  $\alpha_{\text{out}}^{\text{ideal}}(t) = \text{sech}(\gamma t/6 + 5) + 0.5\text{sech}(\gamma t/6 - 5)$  is shown in Fig. 35. The trion decay rate, based on experiment [229], is set at  $\Gamma = 3\mu\text{eV}$ , and the intrinsic cavity loss rate is assumed to be  $\gamma_0 = 0.1 \mu\text{eV}$  [283]. The cavity-fiber tunneling rate is chosen to be  $\gamma = 0.2 \text{ meV}$  and the dot-cavity coupling constant  $g_{\text{cav}} = 0.1 \text{ meV}$  [284]. The fidelity of the single photon generation  $|\langle \alpha_{\text{out}}^{\text{ideal}} | \alpha_{\text{out}} \rangle| \approx 0.9912$ . Because of the non-adiabatic optical pumping and dot-cavity coupling, the whole mapping process can be completed within 300 ps. The simulation of the photon absorption process shows an overall fidelity greater than 0.99 as well. With the above chosen parameters, the cavity mode broadening due to the coupling to waveguide is actually larger than the dot-cavity coupling. The system is therefore *not* in the strong coupling regime by the usual definition [279, 284, 286]. High fidelity is nonetheless guaranteed by the large Purcell factor.

##### 2. Unwanted coupling to energy levels beyond the 3-level $\Lambda$ system

In the energy level structure of the dot-cavity coupled system, non-resonance coupling to other energy levels could lead to excitation out of the 3-level  $\Lambda$  subspace and AC Stark shift of the qubit states of interest (see Fig. 34(c)). These effects have

been included in the numerical simulation given in Fig. 35. As shown in Fig. 35(c), AC stark shift induces a deterministic phase drift between  $|g\rangle$  and  $|e\rangle$ . As the two excitation pathways starting respectively from  $|g\rangle$  and  $|e\rangle$  are independent of each other (see Fig. 34(c)), this phase drift is independent of the coefficients  $C_g$  and  $C_e$ . Therefore, it can be compensated by a single-qubit operation irrespective of the quantum state being mapped. Leakage out of the qubit subspace by the non-resonance excitation to multi-photon states can be greatly suppressed if the Zeeman splitting is much larger than the Rabi frequency and the cavity-dot coupling. For InAs self-assembled QDs, Zeeman splitting  $\sim$  meV can be achieved in a moderately strong magnetic field ( $\sim$  10 T) due to the large g-factor of InAs materials.

### 3. Unknown parameter offsets

Solutions to the laser pulses for desired controls of the quantum interface are based on the knowledge of the coupling strength  $g_{\text{cav}}, \gamma$  and  $\Omega(t)$ . But in practice, there could be various unknown errors on parameters due to imperfect characterization of the system. The robustness of the control schemes in presence of unknown system parameter errors is thus a critical feature. In Table. I, we list the effects of unknown offsets from the assumed values of various parameters on the fidelity of two typical quantum network operations: (i) entangling two quantum nodes into state  $e^{i\phi}|g\rangle_1|e\rangle_2 + |e\rangle_1|g\rangle_2$ ; (ii) transfer of the state  $|g\rangle + |e\rangle$  between two nodes. In both cases, the target shape of the involved single photon wavepacket is  $\text{sech}(\frac{t}{6})$  and the design of the control laser pulses uses the assumed parameter values. The system shows a surprising robustness: 10% unknown errors on  $g_{\text{cav}}, \gamma$  or  $|\Omega(t)|$  only reduce the fidelity by less than 1%. This intrinsic robustness against unknown parameter errors paves the way for learning studies of the system parameters by trial and error [320, 322, 352], and classical feedback controls in the quantum network [353, 354].

### 4. Laser intensity fluctuations

The  $|\Omega(t)|$  error studied in Table. I is a global one on the amplitude, e.g. induced by the QD being slightly out of focus from the laser control field or an unknown offset from the assumed value of the dot dipole moment. The actual control laser pulse may have shape deviations from the desired ones, e.g. due to temporal fluctuations in laser amplitude. The effects of this error source have been studied in [348], where the control scheme is found to be immune against fast fluctuations (see Fig. 36). This robustness is due to the finite bandwidth of the quantum interface determined by the cavity-dot coupling strength and the cavity-waveguide tunneling rate. Any temporal fluctuations in the control field with the frequency higher than the interface bandwidth

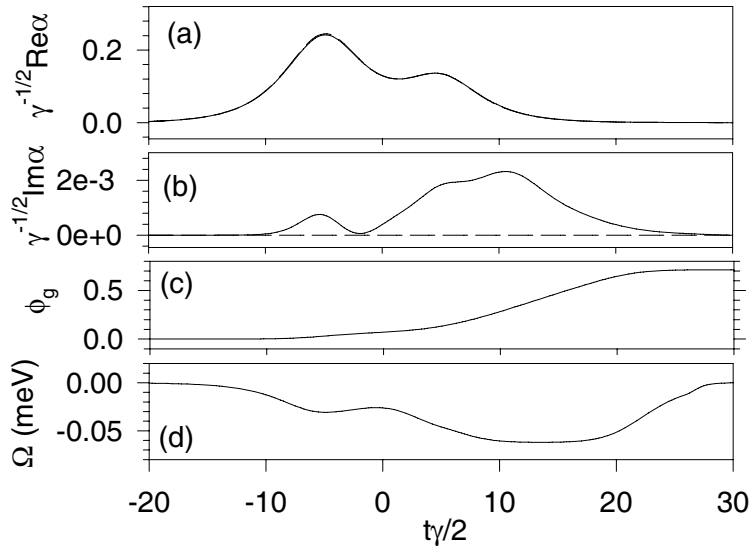


FIG. 35. (Extracted from Ref.[119]) Generation of a single photon wavepacket with an asymmetric double sech shape (see text). (a) Real part of the dimensionless amplitude of the simulated single photon wavepacket (solid line) as a function of the dimensionless time  $\gamma t/2$ . The deviation from the target shape (dashed line) is not visible. (b) Imaginary part of the simulated single photon wavepacket (solid line) and that of the target one (dashed line). (c) Phase drift of the component  $|g, 0\rangle$ . (d) Rabi frequency of the control laser pulse.

are effectively averaged out. The time independent amplitude error listed in Table. I may also be considered as a special shape error which is actually the worst scenario for the fidelity.

### 5. Laser phase fluctuations

The complex Rabi frequency  $\Omega(t)$  can also have phase uncertainties due to laser phase drift which is typically slower than the time scale of interface operation. Assume that the laser control field at the moment of sending operation has an unknown phase of  $\varphi_1$  and, hence, the Rabi frequency is  $\Omega_1(t) e^{i\varphi_1}$ . From the form of the coupling term that involves the laser field in the Hamiltonian Eq. (27), the unknown phase factor can be absorbed by redefining the state  $|\tilde{e}\rangle_1 \equiv e^{-i\varphi_1} |e\rangle_1$ , so that,

$$\frac{1}{2} \left[ i\Omega_1(t) e^{i\varphi_1} e^{-i\omega_L t} |t\rangle_{11} \langle e| + H.c. \right] \equiv \frac{1}{2} \left[ i\Omega_1(t) e^{-i\omega_L t} |t\rangle_{11} \langle \tilde{e}| + H.c. \right] \quad (42)$$

and we can make the same transform at the receiving node where the control laser has the unknown phase  $\varphi_2$  at the moment the single photon arrives. Starting from a general state  $(C_g |g\rangle_1 + C_e |e\rangle_1) |g\rangle_2 \otimes |\text{vac}\rangle \equiv C_g |g\rangle_1 |g\rangle_2 \otimes |\text{vac}\rangle + C_e e^{i\varphi_1} |\tilde{e}\rangle_1 |g\rangle_2 \otimes |\text{vac}\rangle$ , two-node operations in the presence of laser phase uncertainties can be generally expressed as,

$$\begin{aligned} & C_g |g\rangle_1 |g\rangle_2 \otimes |\text{vac}\rangle + C_e e^{i\varphi_1} |\tilde{e}\rangle_1 |g\rangle_2 \otimes |\text{vac}\rangle \\ \xrightarrow{\Omega_1(t)} & C_g |g\rangle_1 |g\rangle_2 \otimes |\text{vac}\rangle \\ & + C_e e^{i\varphi_1} \left[ e^{i\phi} \cos \theta |\tilde{e}\rangle_1 |g\rangle_2 \otimes |\text{vac}\rangle + \sin \theta |g\rangle_1 |g\rangle_2 \otimes |\tilde{\alpha}_{\text{out}}\rangle \right] \\ \xrightarrow{\Omega_2(t-\tau)} & \left[ C_g |g\rangle_1 |g\rangle_2 + C_e e^{i\varphi_1} \left( e^{i\phi} \cos \theta |\tilde{e}\rangle_1 |g\rangle_2 + \sin \theta |g\rangle_1 |\tilde{e}\rangle_2 \right) \right] \otimes |\text{vac}\rangle. \end{aligned} \quad (43)$$

The final state is equivalent to  $[C_g |g\rangle_1 |g\rangle_2 + C_e (e^{i\phi} \cos \theta |e\rangle_1 |g\rangle_2 + e^{i\varphi_1} e^{-i\varphi_2} \sin \theta |g\rangle_1 |e\rangle_2)] \otimes |\text{vac}\rangle$ . If the control laser fields at the two nodes is phase locked so that there is a certain relative phase between  $\Omega_1(t)$  and  $\Omega_2(t-\tau)$ , the two-node operation is well protected from laser phase fluctuations.

### 6. Deterministic phase and shape variations in photon propagation

Unknown offsets from the assumed waveguide/fiber dispersion relation or nonlinearity of the dispersion relation can cause phase and shape variations of the single photon wavepacket during the propagation. At low temperature where thermal fluctuations are suppressed, such variations are deterministic and can thus be incorporated in the design of the receiving node control. Close-loop adaptive feedback control [353, 354] or quantum learning algorithms [320, 322, 352] can be implemented to pre-characterize such variations.

### 7. Loss and indeterministic fluctuation in photon propagation

For inter-node operations between well separated nodes (distance  $\gtrsim m$ ), photon losses and indeterministic fluctuations during the propagation in the fiber could be non-negligible. Error correction schemes dealing with such propagation loss has been proposed using auxiliary stationary qubits in the quantum node [355]. The idea of quantum repeaters with nested purification schemes [356] might also be incorporated into the quantum network design for protection against the photon propagation loss and indeterministic fluctuations.

## E. Summary: Coherent quantum manipulation by remote control

In this section, we have discussed how to unite clusters of QD spins into a network for distributed quantum information processing. The advances in the fabrication of coupled structures of QDs, semiconductor micro-cavities, and optical waveguides

TABLE I. Effect of errors in coupling parameters on the fidelity of entanglement and of state transfer.

	no error	10% $g$ error	10% $\gamma$ error	10% $\Omega(t)$ error
Entanglement	0.9912	0.9872	0.9894	0.9862
Transfer	0.9901	0.9870	0.9891	0.9879

make possible a high efficiency quantum interface between stationary spin qubits and flying photon qubits, where the latter can be used for communication between separated clusters. As indicated in the DiVincenzo criteria [2], such capability greatly enhances the chance towards the construction of fault-tolerant scalable quantum computers in these systems.

Counterintuitively, real excitations of the continuum modes in the quantum channel act as a conduit for mediating coherent operations rather than the cause of dissipation. A more abstract picture for the network structure here is the 3-level  $\Lambda$  system coupled to a one-dimensional continuum modes, formed by the cavity-waveguide coupled structure, considered as a whole electromagnetic continuum. The important function of the cavity is in providing a local resonance in spectrum with large spectral weight near the frequency of the QD optical transition, which results in a large Purcell factor (i.e. the ratio between the spectral weight of the cavity-waveguide modes and the free-space modes). The unitary evolution dominates over the irreversible processes within the coupled system of the QD and the cavity-waveguide continuum. Temporal shaping of the laser control pulse provides sufficient freedom to control such evolution. While the relevant part of the spectrum of the cavity-waveguide continuum is of a simple Lorentz shape with width  $\gamma \ll \omega_c$ , this Markovian condition is not a mandatory requirement. Provided that the 3-level  $\Lambda$  system is coupled to a continuum where a spectral weight peak (irrespective of shape) results in a high Purcell factor at the relevant optical frequency, control schemes for high efficiency network operation is possible [357]. This opens up possibilities for networking localized stationary qubit by continuum modes without cavity QED and in the non-Markovian regime.

## VIII. CHALLENGES

We have discussed all the necessary elements for implementing scalable quantum computation with electron spins in QDs under optical control. To reach the larger goals, there remain many obstacles. Here we present an overview of what technologies may be at the top of the required list to accomplish the goals. To have a concrete idea of the challenges for short- to mid-term pursuit, we will also give an estimate of the resources for a benchmark task: factorization of 15 with Shor's algorithm.

### A. Resource estimate for Shor's algorithm for factorizing 15

Undoubtedly, Shor's algorithm for factorizing integers is the most important example demonstrating the superpower of quantum computation [1, 172]. It gives a solution with time consumption only polynomially increasing with the problem size (the bit length of the number to be factorized) and thus offers an exponential speedup over all known classical counterparts. Historically, Shor's algorithm has stimulated the exploding enthusiasm in quantum computation by showing its computation power. An efficient factorization scheme can be used to break the public-key encryptions such as the RSA protocol which is widely used in internet communication. The factorization of the first "non-trivial" number – 15 by Shor's algorithm has been realized with

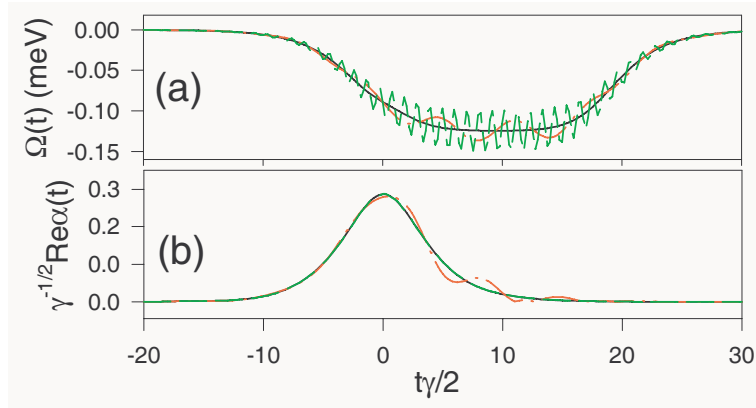


FIG. 36. (Extracted from Ref. [348]) Transfer of state  $|g\rangle + |e\rangle$  between two nodes in presence of amplitude fluctuations of the control lasers. (a) The desired control laser pulse by design at the sending node (solid curve) and the actually applied control pulse with slow fluctuations (dashed-dotted curve) and fast fluctuations (light curve). The control laser pulse at the receiving node has a similar error applied. (b) The generated intermediate single photon wavepacket. The solid curve shows the target shape of the single photon if the ideal control laser pulse is used (solid curve in (a)). Deviation of the generated single photon wavepacket is invisible in the case of fast laser fluctuations. The fidelity of the transfer is 0.9912 with slow fluctuations and 0.9922 with fast fluctuations. The parameters used are:  $\gamma = 0.2\text{meV}$ ,  $g_{\text{cav}} = \gamma/2$ ,  $\gamma_l = 3\mu\text{eV}$ , and intrinsic cavity leakage  $0.05\mu\text{eV}$ .

the liquid NMR spectroscopy [3], which serves as a benchmark for quantum computation in other systems. Here we give an estimate of the resources required to accomplish such a milestone in the optically controlled spin-based QD system.

The key step of Shor's algorithm for factorizing a number  $N$  is to find the smallest nonzero  $r$  satisfying  $a^r = 1 \pmod{N}$  (i.e., the order of  $a$  with respect to  $N$ ), where the seed  $a$  is co-prime to  $N$  [i.e. the maximum common factor of  $a$  and  $N$ , denoted as  $(a, N)$  is 1] and can be randomly selected. By the fact that the order  $r$  is the period of the modular exponentiation function  $f(x) = a^x \pmod{N}$ , it suffices to search for the period or to measure the frequency of the function  $f(x)$ , which can be accomplished by the quantum Fourier transformation (QFT). The process of finding the period can be expressed as [1, 172]

$$\begin{aligned} |0^n\rangle \otimes |0^m\rangle &\xrightarrow{QFT^{-1}} \sum_{x=0}^{2^n-1} |x\rangle \otimes |0^m\rangle \xrightarrow{f(x)} \sum_{x=0}^{2^n-1} |x\rangle \otimes |a^x \pmod{N}\rangle \\ &\xrightarrow{QFT} \sum_{y=0}^{2^n-1} \sum_{x=0}^{2^n-1} e^{i2\pi xy/2^n} |y\rangle \otimes |a^x \pmod{N}\rangle, \end{aligned} \quad (44)$$

where  $|0^{n(m)}\rangle$  denotes a  $n(m)$ -qubit register set at the zero state,  $m = \lceil \log_2 N \rceil + 1$  is the bit length of  $N$ ,  $x$  is a binary number, and the normalization constants for the states have been omitted. Both the QFT and the modular exponentiation can be carried out with the number of elementary quantum gates polynomially increasing with the problem size ( $m$ ). A more detailed review of the order-finding algorithm is given in Appendix C 1.

As  $f(x)$  is a periodic function with period  $r$ , the population of the basis state of the first register at the end of the program will be non-zero only for  $y \approx 2^n c/r$  ( $c = 0, 1, \dots, r-1$ ), for the QFT will transform a period function into sharp peaks at the multiples of the frequency  $2^n/r$ . Thus, a quantum measurement of the first register in the computational basis will result one of states in the superposition, thus yielding the number  $2^n c/r$  from which the order  $r$  can be derived and the number  $N$  factorized. The order  $r$  generally is of the order of magnitude of  $N \sim 2^m$ , so the number of basis states in the superposition is  $\sim 2^m$ , an exponential function of the problem size, which explains why a QND measurement is required to make Shor's algorithm scalable for factorizing large numbers, as discussed in Sec. VI.

The flow-chart of Shor's algorithm for order finding is shown in Fig. 37. The first QFT subroutine can be simplified to a series of single-qubit Hadamard gates (see Appendix C 1 for the definition of the elementary quantum gates) since the initial state is set to be  $|0^n\rangle$ . The second register is initialized to be  $|1\rangle$  to facilitate the modular exponentiation. In principle, the length of the first register  $n$  should be large enough to reproduce the real number  $1/r$  with sufficient effective bits. To factorize 15, it turns out that the orders of all co-primes of 15 are either 2 (for  $a=4, 11, 14$ ) or 4 (for  $a=2, 7, 8, 13$ ), both of which are a factor of  $2^3$ , so three-qubit register should be enough to resolve  $2^n/r$ . Including the second register, 7 qubits are sufficient to demonstrate the algorithm for the first "non-trivial" target: 15.

Figure 38 and 39 give the specific quantum circuits constructed with the elementary quantum gates (as defined in Appendix D) to implement Shor's algorithm for factorizing 15 with the seed number selected as  $a = 4$  (an easy example) and  $a = 13$  (a difficult example). Compilation and optimization have been performed to reduce the number of physical operations:

1. To minimize the number of SWAP gates for coupling remote qubits in the linear configuration, the labelling of the qubits in the register has been optimized, and at the end of the program the qubits are not swapped back to their original positions but re-labelled instead, as indicated in Fig. 16 (a).
2. The quantum gates are omitted if they act on the second register after the last gate controlled by the first register, since such gates have no effect on the QFT of the first register.
3. Whenever possible, the sequential single-bit operations on the same qubit are combined into one single-qubit gate (in experiment, all one-bit gates between two controlled gates can be realized by a single-spin rotation).

The numbers of gates and pulses and the running time needed in different cases are estimated with the following considerations:

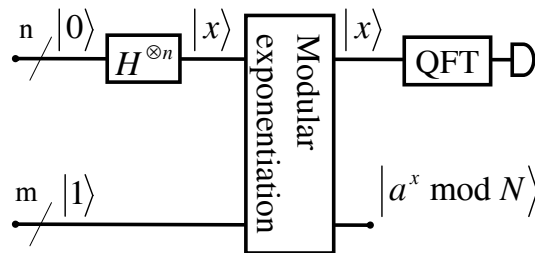


FIG. 37. Logic flow-chart of Shor's algorithm for order searching.

TABLE II. The numbers of gates and pulses and the time required to factorize 15 by Shor's quantum algorithm with two typical examples of seed numbers  $a$  for  $a' = 1 \pmod{15}$ .

$a$	# 1-bit gates	# SWAP	# phase gate	# pulses	time-cost
a=4	4	1	3	44	0.9 ns
a=13	20	8	15	142	1.3 ns

1. All sequential single-qubit gates on the same qubit are combined as one single-spin rotation which can be completed with three pulses within 10 ps.
2. Each SWAP gate can be completed by two pulses within 10 ps.
3. Each controlled phase gate can be completed by three pulses in 10 ps.
4. Each qubit can be initialized by three pulses within 120 ps.
5. To reduce the complexity of pulse designing, all operations within the local module should be performed serially (to factorize larger numbers, a large-scale quantum network of distributed modules will be needed and in that case operations could be performed in parallel in separated modules).
6. The time consumption for quantum measurement is not counted.

The timescales of the single- and two-qubit gates are chosen in accordance with the discussions in Sec. IV. While there are so far no experimental demonstrations of optically controlled two-qubit gates, the estimated timescales of the single-qubit gates are similar to the experimentally realized gates [78, 79, 181, 182]. The estimated resource requirements are summarized in Table II. Alternatively, the controlled phase gates can be replaced by the  $\sqrt{\text{SWAP}}$  gates, and the resource requirement is expected to be similar.

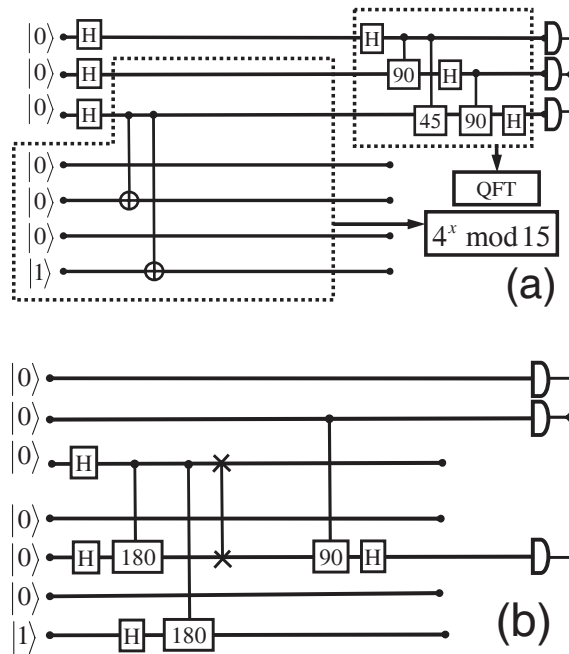


FIG. 38. (a) Quantum circuit for searching  $r$  for  $4^r = 1 \pmod{15}$ , where the subprograms for the modular exponentiation and the QFT are blocked together as indicated. (b) The simplified circuit with only local two-qubit gates.



**B. Technologies most needed**

*1. Complex multi-pulse optics*

As listed in Table II, to factorize the small number 15, the number of optical pulses needed is in the order of 100. It is would be extremely difficult to synchronize so many laser pulses and to stabilize the relative phases, but all the pulses may be viewed as a single one with complex frequency and phase design. The complex pulse may be formed from a single laser source by pulse shaping techniques, such as acousto-optical modulation [358, 359]. Design of such a complex pulse is also very challenging. Learning or genetic algorithms may be developed to deal with the problem, with lessons learned from controlling complex chemical processes by ultrafast optical pulses [320–322]. The measurement involves many probe pulses interacting with many QDs. The signals are to be analyzed through frequency multiplexer as well as phase modulation with heterodyne detection [331]. Thus multi-dimensional spectroscopies [360–363] are desirable for characterizing the systems and for implementing a small-scale benchmark demonstration. Eventually, the measurement would have to be done with an efficient quantum channel like a cavity-waveguide structure.

*2. System fabrication and characterization*

The design of the quantum computer and its operation follow the sequence: The physical system is constructed first, with certain uncontrollability. Then it is characterized. The optical control will be designed according to the system parameters. In such a procedure, we do not require an ultimate control of the system fabrication (hardware) but defer the difficult work to the control design (software) stage. For example, we do not require, and actually do not desire that all the QDs are almost identical. But of course, the system should be fabricated fulfilling certain conditions. Basically, we need a system made of QD clusters, which should meet the following requirements:

1. QDs are only locally coupled. For a system with coupling between remotely separated dots, the design of the controlling pulses would require overhead increasing exponentially with the number of qubits, since essentially the control design amounts to solving the Schödinger equation of the whole system.
2. The coupling between different QDs in a local node should be weak. Otherwise, tunneling between different dots would make the local node rather a large QD molecule instead of a cluster of individual dots, making even a single-qubit gate as complex as a control of all the qubits in the local node.
3. Even though we do not require all the QDs to be nearly identical, the size of different QDs in a cluster should be in

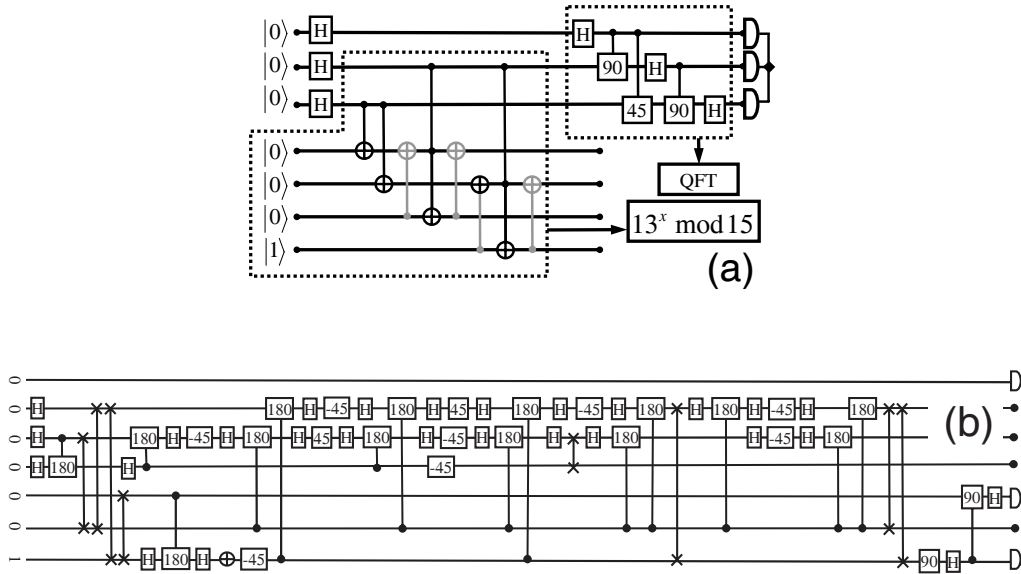


FIG. 39. (a) Quantum circuit for searching  $r$  for  $13^r = 1 \bmod(15)$ . The faded components can be removed without changing the computing result. (b) The simplified circuit with all gates experimentally realizable.

a relatively small range. Otherwise, the optical control, especially the energy shift by the AC Stark effect, would be extremely difficult.

4. The number of active electrons in each QD should be controlled to be one, either by doping or by gate voltage control.

Once a QD system has been constructed, the characterization is not any less demanding. The parameters to be determined include electron doping level, electron spin  $g$ -factors, frequencies of the ground and excited state transitions, selection rules or relative dipole matrix elements for different transitions, tunneling rates and exchange interaction of electrons in different levels and different dots, etc. Identification of the exciton, bi-exciton, or trion transitions in two-dot systems have already been demonstrated in two vertically coupled dots with the help of varying the gate voltage [195]. A pair of laterally coupled dots remains a challenge. The characterization of a cluster of, for example, seven QDs, is a tremendously difficult target for the current experiment capability. In the long run, we would expect no full characterization of the system be required. The solution may lie in, again, the learning algorithm, by which, the controlling optical pulses are to be designed, self-adaptive to the fidelity of a certain set of quantum gates.

### 3. Nano-photonics

The requirement of nano-optics is two-folded: First, the control of a local node requires near-field optical addressing. Second, the ultrafast fast initialization and QND measurement of a qubit, and coupling between different nodes need cavities and waveguides fabricated in-situ with the QDs.

To address individually each cluster of QDs, a micro-lens and micro-fiber may be used. Each QD within a cluster is distinguished by its fingerprint transition frequencies. The spatial resolution required is given by the distances between clusters instead of the size of the clusters. Using high-index material for the micro-lens, spatial resolution  $\sim 0.1 \mu\text{m}$  may be achievable. In cases where the spatial resolution is not enough to single out dot clusters, an alternative solution would be further pulse shaping (probably with a learning algorithm as well) to eliminate the coupling between different clusters covered by one micro-lens.

To connect QDs with cavities and waveguides, two structures look promising. One is obtained by etching the surface where the QDs are grown [278]. Electron-beam lithography and chemical etching (sometimes plus some annealing) have already produced high-quality microcavities and waveguides on semiconductor surfaces. Even strong coupling between a QD and microcavity in such a system has been demonstrated [279]. Photonic crystals are another promising possibility. Point defects in photonic crystals can be made into nano-cavities with Q-factor  $\gtrsim 10^6$  and effective volume less than a half-wavelength cubed [282, 283]. Strong coupling between a QD and a photonic crystal nano-cavity has also been demonstrated [284, 285]. Quantum electrodynamics of single QDs in nano-cavity in photonic crystals can be engineered [281, 304, 305]. Waveguides in photonic crystals can be made by line defects which may be coupled to remote nodes by optical fibers [301]. How to combine these photonic structures with the QD clusters, especially, how to assemble them in proper layouts and positions, would demand a great deal of progress in sample processing technologies.

We would like to point out that the photonic structure fabricated on the QD system may also be used to individually address each local node. Thus, we eventually may need no micro-lens or micro-fibers to attach each dot cluster.

A wilder conjecture is that the lasers be integrated in the photonic structure. Micro- or nano-lasers made of photonic crystal cavities have actually come into being. The remaining problem would be to make the laser emit into a waveguide, and to tailor it into wanted shapes and sequences. How is one to control the laser on-chip then? Electrical gates may be used. So we come around a full circle and find a point where different quantum computation strategies may be synthesized to achieve a common goal.

## IX. CONCLUSION

We have discussed various aspects of a scalable scheme of quantum computation based on optical control of electron spins in semiconductor QDs. To implement such a scheme, a number of outstanding challenges remain to be overcome.

We would like to add some remarks on two different philosophies in implementing digital computing or more generally automatic reasoning, which may give us some inspiration in the journey to realize quantum computation. One is related to the von Neumann structure of computers and the other is related to the Turing ACE structure, both of which are based on Turing's insightful view of programs and data as essentially the same for a universal computer. Turing's design is deeply rooted on his finding of universal computers and thus has a hardware of minimal instructions with complex functions to be implemented by software programming. The von Neumann structure, while keeps as well the important role of programming, tries to maximize the usage of hardware design to implement a large number of mathematical functions which would otherwise be solved simply by programming. We follow Turing's perception in describing the blueprint of a quantum computer based on semiconductor QDs and optical control of spins in them, simply for one reason: In implementing quantum computation, the hardware part is far more formidable than the design of optimal control. Thus we propose no need of perfectly controlled arrays of almost identical

QDs but a control scheme programmed after a physical structure has been constructed and characterized. The randomness in the system synthesis is not to be eliminated but to be utilized. The requirement for a functional physical block is relatively simple: sufficient coupling for a universal set of quantum gates to be programmed. Finally, we note that Turing's philosophy is becoming more and more important nowadays in large-scale classical computers which tend towards the RISC (reduced instruction set computer) architecture.

When will a quantum computer come into being of practical usage? We do not know. But a hint may lie in the comparison between our present situation and the situation something 60 years ago when engineers were working hard to maintain thousands of vacuum tubes functioning together for a while before one or another went wrong. Scaling up of a quantum computer may be not as rapid as classical computers have done, but just be aware that adding one functioning qubit supposedly doubles the power of a quantum computer, which is worth 18 hardworking months in the sense defined by Moore's law.

### ACKNOWLEDGEMENTS

This review is based on works done in long collaborations with many people, including D. G. Steel, D. Gammon, P. Chen, C. Peirmarocchi, S. E. Economou, S. K. Saikin, C. Emary, W. Yang and under financial supports from ARDA/ARO, ARO/NSA/LPS, QuIST/AFOSR, NSF and Hong Kong RGC.

### Appendix A: Hole-mixing and selection rules in a quantum dot

In the III-V bulk material, the top of valance band occurs at the  $\Gamma$  point of the Brillouin zone (see Fig. 40). The spin-orbit coupling of the  $p$ -orbit splits the  $p$ -type valance band to a quadruplet with  $\Gamma_8$  symmetry (or a total angular momentum  $J = 3/2$ ) and a doublet with  $\Gamma_7$  symmetry (or a total angular momentum  $J = 1/2$ ). The  $\Gamma_7$  band lies much lower in energy than the  $\Gamma_8$  bands. From now on, we focus on the bands derived from the  $J = 3/2$  quadruplet, which are described by the Luttinger Hamiltonian in the framework of effective-mass theory [364]

$$H_L = \frac{1}{2m_0} \begin{pmatrix} P_1 & Q & R & 0 \\ Q^* & P_2 & 0 & R \\ R^* & 0 & P_2 & -Q \\ 0 & R^* & -Q^* & P_1 \end{pmatrix}, \quad (\text{A1})$$

expressed in a matrix form in the basis  $\{|J_z = 3/2\rangle, |J_z = 1/2\rangle, |J_z = -1/2\rangle, |J_z = -3/2\rangle\}$ , with

$$P_1 = (\gamma_1 - 2\gamma_2)k_z^2 + (\gamma_1 + \gamma_2)(k_x^2 + k_y^2), \quad (\text{A2a})$$

$$P_2 = (\gamma_1 + 2\gamma_2)k_z^2 + (\gamma_1 - \gamma_2)(k_x^2 + k_y^2), \quad (\text{A2b})$$

$$Q = -2\sqrt{3}\gamma_3k_z(k_x - ik_y), \quad (\text{A2c})$$

$$R = -\sqrt{3}[\gamma_2(k_x^2 - k_y^2) - 2i\gamma_3k_xk_y], \quad (\text{A2d})$$

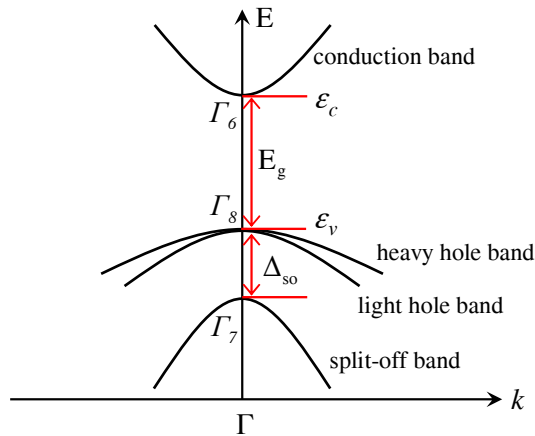


FIG. 40. Bulk band structures of direct bandgap III-V semiconductors.

where  $\gamma_{1,2,3}$  denote the Luttinger coefficients. The  $|J_z = \pm 3/2\rangle$  and  $|J_z = \pm 1/2\rangle$  bands are usually referred as the heavy hole and light hole bands respectively by their different effective mass in the  $z$  direction.

Hole mixing effects are caused by the QD confinement potential  $V_h(x, y, z)$ . Here for simplicity, the growth direction  $z$  is assumed to be along the [001] direction. For other growth directions, the discussions below can be generalized straightforwardly, and the essential conclusions would not be changed. Strong quantum confinement in the growth ( $z$ ) direction lifts the four-fold degeneracy at  $\Gamma$  point (see Fig. 41(a)). The light hole states actually have a larger in-plane effective mass and therefore their dispersion tend to cross into the heavy hole bands at finite in-plane wavevector  $k_\perp$  (see Fig. 41(b)). Spin-orbit coupling thus results in anti-crossing and the mixture of the heavy-hole and light-hole bands (see Fig. 41(c)) [364].

Let us consider first the zeroth-order approximation for the hole-mixing. When the confinement size along the  $z$ -direction is much smaller than the lateral size, we have  $\langle k_z^2 \rangle \gg \langle k_x^2 \rangle, \langle k_y^2 \rangle$ . If the off-diagonal couplings  $Q$  and  $R$  are neglected, the Hamiltonian is diagonal in the basis of the angular momentum quantized along the growth direction. The heavy and light holes, with kinetic energy  $P_1$  and  $P_2$ , are characterized by their angular momentum states as  $|\pm 3/2\rangle$  and  $|\pm 1/2\rangle$ , respectively. The heavy hole (HH) and the light hole (LH) are separated by an energy  $\Delta_{HL} = 2\gamma_2 \langle k_z^2 \rangle / m_0$  [364]. The hole-mixing are induced by  $Q$  and  $R$  terms. The  $Q$  terms couple  $|\pm 3/2\rangle$  to  $|\pm 1/2\rangle$ , and the  $R$  terms couple  $|\pm 3/2\rangle$  to  $|\mp 1/2\rangle$ . As we usually have  $\Delta_{HL} \gg \langle Q \rangle, \langle R \rangle$ , the zeroth-order approximation and the corresponding selection rules determined by the angular momentum conservation are often adequate to understand the optical transitions.

For small QDs, the mixing may be important. Now let us consider the HH-LH mixing in different situations.

First we consider a confinement potential with rotational symmetry about the growth direction. If we assume  $\gamma_2 = \gamma_3$ , the Hamiltonian has the rotational symmetry. The HH and LH states coupled by the  $Q$  and  $R$  terms must have different orbital angular momentum. So the light-hole components mixed into, e.g., the heavy hole ground state are not optical active. In this case, the mixing has no effect on the optical transitions but a reduction of the dipole matrix element. The problem comes from the fact that in reality we usually do not have a cylindrical  $V(x, y, z)$  or  $\gamma_2 \neq \gamma_3$  (since the lattice has no spherical symmetry).

Let us still make the assumption that the confinement potential  $V$  has inversion symmetry in the  $z$ -direction, which is reasonably fulfilled in fluctuation QDs. Since the  $Q$  terms are linear in the  $k_z$ , they couple HH and LH states with different parity which are separated by large energies due to the strong confinement in the  $z$ -direction. In the even parity ground state, the hole mixing effect caused by the  $Q$  terms is negligible, especially in optical transitions. Thus, we need only to consider the coupling induced by the  $R$  terms. Thus the optically active components of the HH ground states are

$$|H\pm\rangle = |\pm 3/2\rangle + \eta|\mp 1/2\rangle, \quad (\text{A3})$$

where  $\eta \sim L_z^2/L_{x,y}^2$  (with  $L_z$  and  $L_{x,y}$  being the vertical and lateral confinement sizes, respectively) and normalization is understood. The dipole matrix elements between the electron spin states  $|\pm 1/2\rangle$  and the trion states  $|t\pm\rangle$  which contains the HH in  $|H\pm\rangle$  are (in arbitrary units)

$$\langle t\pm | \mathbf{d} \cdot \boldsymbol{\sigma}_\pm | \pm 1/2 \rangle = 1, \quad (\text{A4a})$$

$$\langle t\pm | \mathbf{d} \cdot \boldsymbol{\sigma}_\mp | \pm 1/2 \rangle = \eta', \quad (\text{A4b})$$

$$\langle t\mp | \mathbf{d} \cdot \boldsymbol{\sigma}_\pm | \pm 1/2 \rangle = 0, \quad (\text{A4c})$$

$$\langle t\mp | \mathbf{d} \cdot \boldsymbol{\sigma}_\mp | \pm 1/2 \rangle = 0, \quad (\text{A4d})$$

where  $\boldsymbol{\sigma}_\pm$  is the circular polarization of a light normally propagating and  $\eta' \sim \eta$ . The selection rules are shown in Fig. 42. The two subspaces  $\{|+1/2\rangle, |t+\rangle\}$  and  $\{|-1/2\rangle, |t-\rangle\}$  are disconnected under optical coupling, which means the electron spin along the growth direction is still conserved unless an external magnetic field is applied along an in-plane direction. With a magnetic field along the  $x$ -direction, we can choose a light with the polarization, e.g.,

$$\tilde{\boldsymbol{\sigma}}_+ \equiv \boldsymbol{\sigma}_+ - \eta' \boldsymbol{\sigma}_-, \quad (\text{A5})$$

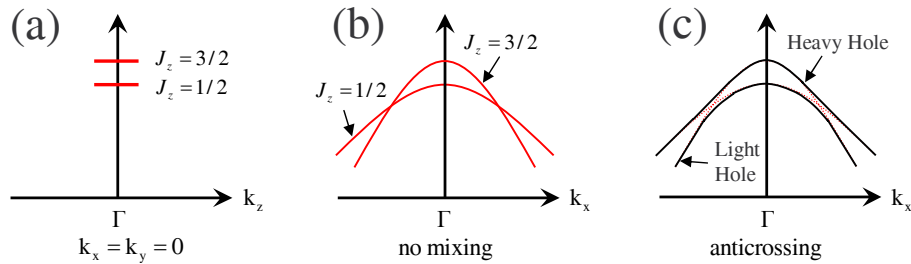


FIG. 41. Dispersion relation of the  $|J_z = 3/2\rangle$  and  $|J_z = 1/2\rangle$  valence bands in a quantum well [364]. (a) Energy shift due to the confinement in the growth direction. (b) In-plane dispersion of the two valence bands when the “off-diagonal” terms are neglected (without mixing). (c) Level anti-crossing when “off-diagonal” terms are included.

which couples the electron spin eigen states  $|\pm x\rangle$  to the common trion state  $|t+\rangle$  with renormalized dipole matrix elements  $(1 \pm \eta'^2)$ . The theories for the case without hole mixing can be generalized simply by replacing the dipole matrix elements there with the renormalized.

In systems without the inversion symmetry, which is often the case for InAs self-assembled QDs, the mixing would make the two ground HH states to be

$$|H+\rangle = | + 3/2\rangle + \zeta| + 1/2\rangle + \eta| - 1/2\rangle + \xi| - 3/2\rangle, \quad (\text{A6})$$

$$|H-\rangle = | - 3/2\rangle + \zeta| - 1/2\rangle + \eta| + 1/2\rangle + \xi| + 3/2\rangle, \quad (\text{A7})$$

where  $\eta$  and  $\zeta$  are small numbers ( $\lesssim 10\%$  for typical self-assembled QDs), and  $\xi \sim \eta\zeta$ . Now the dipole matrix elements are

$$\langle t \pm | \mathbf{d} \cdot \boldsymbol{\sigma}_{\pm} | \pm 1/2 \rangle = 1, \quad (\text{A8a})$$

$$\langle t \pm | \mathbf{d} \cdot \boldsymbol{\sigma}_{\mp} | \pm 1/2 \rangle = \eta', \quad (\text{A8b})$$

$$\langle t \mp | \mathbf{d} \cdot \boldsymbol{\sigma}_{\mp} | \pm 1/2 \rangle = \zeta', \quad (\text{A8c})$$

$$\langle t \mp | \mathbf{d} \cdot \boldsymbol{\sigma}_{\pm} | \pm 1/2 \rangle = \xi', \quad (\text{A8d})$$

with  $\eta' \sim \eta$ ,  $\zeta' \sim \zeta$ , and  $\xi' \sim \xi$ , all being small numbers. Interestingly, all the states now are optically connected. Thus it is possible to perform an arbitrary spin rotation by optical control without applying an external magnetic field or tilting the light beam from the normal direction. (For a QD without a symmetry axis, the normal direction is not special). For example, if the light polarization is chosen to be  $\mathbf{X} \equiv \boldsymbol{\sigma}_+ + \boldsymbol{\sigma}_-$ , the dipole matrix elements between the spin states  $|\pm x\rangle$  and the trion states  $|t \pm x\rangle \equiv |t+\rangle \pm |t-\rangle$  are

$$\langle t+x | \mathbf{d} \cdot \mathbf{X} | +x \rangle = 1 + \eta' + \zeta' + \xi', \quad (\text{A9a})$$

$$\langle t+x | \mathbf{d} \cdot \mathbf{X} | -x \rangle = 0, \quad (\text{A9b})$$

$$\langle t-x | \mathbf{d} \cdot \mathbf{X} | +x \rangle = 0, \quad (\text{A9c})$$

$$\langle t-x | \mathbf{d} \cdot \mathbf{X} | -x \rangle = 1 + \eta' - \zeta' - \xi'. \quad (\text{A9d})$$

Thus the AC Stark effect induces an effective magnetic field along the  $x$ -direction, which, as compared the effective magnetic field along the growth direction induced by a circularly polarized light, is reduced by a factor  $\sim (\zeta' + \xi')$ . To realize an arbitrary rotation without a static magnetic field, the optical field would need to be much stronger than with a static magnetic field, unless the QD lateral size is comparable to the vertical size (such as in the case nanocrystals or spherical QDs formed by chemical deposition).

The heavy-light hole mixing coefficients  $\zeta$  and  $\eta$  can be extracted using the polarization dependent absorption spectroscopy as described in Ref. [365]. For typical InAs self-assembled dots studied by Steel's group,  $\zeta$  is negligible and  $\eta$  varies in the range  $\sim 0.1 - 0.2$  for different dots [147, 257].

## Appendix B: Theory of electron spin decoherence by interacting nuclear spins

In this appendix, we give the details on the theory of electron spin decoherence by interacting nuclear spins in a strong magnetic field ( $\geq 1$  Tesla), which was first formulated in Ref [127].

The mesoscopic system consists of an electron with a spin vector  $\hat{\mathbf{S}}_e$  and  $N$  nuclear spins,  $\hat{\mathbf{J}}_n$ , with Zeeman energies  $\Omega_e$  and  $\omega_n$  under a magnetic field  $B_{\text{ext}}$ , respectively, where  $n$  denotes both positions and isotope types (e.g.  $^{75}\text{As}$ ,  $^{69}\text{Ga}$  and  $^{71}\text{Ga}$  in GaAs). The interaction can be separated as ‘‘diagonal’’ terms which involve only the spin vector components along the field ( $z$ )

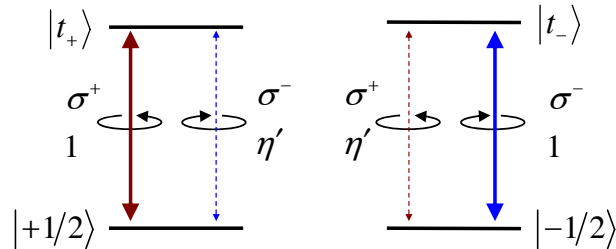


FIG. 42. Selection rules of optical transitions in a doped QD with inversion symmetry along the growth direction. The solid lines denote the allowed transitions, and the dashed lines denotes the ‘‘forbidden’’ transitions which have a relative dipole matrix element  $\eta'$ .

direction and “off-diagonal” terms which involve spin flips. Because the electron Zeeman energy is much larger than the strength of the hyperfine interaction, the off-diagonal term is eliminated by a standard canonical transformation, with the second-order correction left as the hyperfine-mediated nuclear interaction [127], called the extrinsic interaction in Section II D 1. For the same reason, the off-diagonal part of the nuclear interaction contributes only when the terms conserve the Zeeman energies (so-called secular terms in the NMR terminology). Hence, the non-secular terms are negligible. The total reduced Hamiltonian is obtained for the limit of long longitudinal electron spin relaxation time ( $T_1 \rightarrow \infty$ ),

$$\hat{H}_{\text{red}} = \hat{H}_e + \hat{H}_N + \sum_{\pm} |\pm\rangle \hat{H}^{\pm} \langle \pm|, \quad (\text{B1})$$

with  $\hat{H}_e = \Omega_e \hat{S}_e^z$ ,  $\hat{H}_N = \omega_n \hat{J}_n^z$ , and the interaction terms,

$$\hat{H}^{\pm} = \pm \hat{H}_A + \hat{H}_B + \hat{H}_D \pm \hat{H}_E, \quad (\text{B2})$$

given by,

$$\hat{H}_A = \sum'_{n \neq m} \frac{a_n a_m}{4\Omega_e} \hat{J}_n^+ \hat{J}_m^- \equiv \sum'_{n \neq m} A_{n,m} \hat{J}_n^+ \hat{J}_m^-, \quad (\text{B3a})$$

$$\hat{H}_B = \sum'_{n \neq m} B_{n,m} \hat{J}_n^+ \hat{J}_m^-, \quad (\text{B3b})$$

$$\hat{H}_D = \sum_{n < m} D_{n,m} \hat{J}_n^z \hat{J}_m^z, \quad (\text{B3c})$$

$$\hat{H}_E = \sum_n \frac{a_n}{2} \hat{J}_n^z \equiv \sum_n E_n \hat{J}_n^z, \quad (\text{B3d})$$

where  $|\pm\rangle$  are the eigenstates of  $\hat{S}_e^z$ , the summation with a prime runs over only the homo-nuclear pairs, the subscript  $A$  denotes the extrinsic hyperfine mediated interaction,  $B$  the off-diagonal part of the intrinsic nuclear interaction,  $D$  the diagonal part of the intrinsic interaction, and  $E$  the diagonal part of the contact electron-nuclear hyperfine interaction. The hyperfine energy, determined by the electron wavefunction, has a typical energy scale  $E_n \sim a_n \sim 10^6 \text{ s}^{-1}$  for a dot with about  $10^6$  nuclei [366]. The sum,  $\mathcal{A} \equiv \sum_n a_n$ , is the *hyperfine constant* depending only on the material. The intrinsic nuclear spin-spin interaction has the near-neighbor coupling strength  $B_{n,m} \sim D_{n,m} \sim 10^2 \text{ s}^{-1}$ . The extrinsic hyperfine-mediated interaction, which is unrestricted in range within the QD and associated with opposite signs for opposite electron spin states, has an energy scale dependent on the field strength,  $A_{n,m} \sim 1-10 \text{ s}^{-1}$  for field  $\sim 40-1 \text{ T}$ . Thus, the intrinsic interaction dominates local pair-interactions, while non-local pairs are driven by the extrinsic mechanism.

#### a. Formal theory of decoherence in a nuclear spin bath

After the initialization step of the electron spin qubit, the electron-nuclear spin system is prepared in a product state with the nuclear spins in a thermal state with temperature  $T$ , described by the density matrix

$$\hat{\rho}(0) = \hat{\rho}^e(0) \otimes \hat{\rho}^N. \quad (\text{B4})$$

The time evolution of the reduced density matrix of the electron spin,

$$\hat{\rho}^e(t) = \text{Tr}_N \hat{\rho}(t), \quad (\text{B5})$$

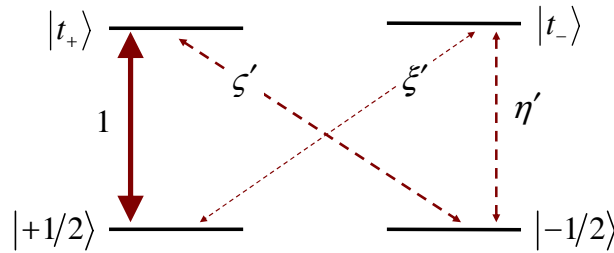


FIG. 43. The relative dipole matrix elements in a doped QD with irregular shape but a large lateral to vertical size ratio. The light polarization is assumed to  $\sigma_+$ . The solid lines denote the allowed transitions, and the dashed lines denotes the “forbidden” transitions which have relative dipole matrix elements  $\eta'$ ,  $\zeta'$ , and  $\xi'$ .

is obtained by tracing over the nuclear spins, may be expressed in the form,

$$\rho_{\mu,\nu}^e(t) = \sum_{\mu',\nu'} \mathcal{L}_{\mu,\nu;\mu',\nu'}(t) \rho_{\mu',\nu'}^e(0) \quad (\text{B6})$$

where  $\rho_{\mu,\nu}^e \equiv \langle \mu | \rho^e | \nu \rangle$ , and  $|\mu\rangle, |\nu\rangle \in \{|+\rangle, |-\rangle\}$ . The superoperator or correlation function  $\mathcal{L}_{\mu,\nu;\mu',\nu'}$  can be expressed in terms of the evolution operator and contains the information on the electron spin relaxation and decoherence.

The Hamiltonians of Eq. (B1) for the  $T_1 \rightarrow \infty$  limit conserves the electron  $\hat{S}_z^e$  quantum number:  $[\hat{H}, \hat{S}_z^e] = 0$ . Hence, the correlation function has following properties,

$$\mathcal{L}_{\mu,\nu;\mu',\nu'}(t) = \mathcal{L}_{\mu,\nu}(t) \delta_{\mu,\mu'} \delta_{\nu,\nu'}, \quad (\text{B7a})$$

$$\mathcal{L}_{\mu,\mu}(t) = 1, \quad (\text{B7b})$$

$$\mathcal{L}_{+,-}(t) = \mathcal{L}_{-,+}^*(t), \quad (\text{B7c})$$

and the specific expression for the free-induction decay (FID),

$$\mathcal{L}_{+,-}(t) = e^{-i\Omega_e t} \text{Tr}_N \left[ \hat{\rho}^N e^{+i\hat{H}^- t} e^{-i\hat{H}^+ t} \right], \quad (\text{B8})$$

which can be straightforwardly extended to dynamics under pulse control.

The ensemble of nuclear spins, at temperature  $T \gtrsim \omega_n \gg A_{n,m}, B_{n,m}, D_{n,m}, E_n$ , may be approximated by the density matrix,

$$\hat{\rho}^N \approx e^{-\hat{H}_N/T} = \sum_{\mathcal{J}} P_{\mathcal{J}} |\mathcal{J}\rangle \langle \mathcal{J}|, \quad (\text{B9})$$

where  $|\mathcal{J}\rangle \equiv \bigotimes_n |j_n\rangle$ ,  $j_n$  being the quantum number of nuclear spin  $n$  in the magnetic field direction.  $P_{\mathcal{J}}$  is the thermal distribution factor. While *single-system dynamics* (i.e., with the nuclear bath initially in a pure state  $|\mathcal{J}\rangle$ ) could be the ultimate aim for quantum applications, we note that all experiments to date are performed under the ensemble scenario, either in a spatial ensemble of many dots [109, 177, 205] or in a single dot with repeated measurements [112, 161, 202], where the statistical average over the initial configurations is needed.

The correlation function  $\mathcal{L}_{+,-}(t)$  can then be generally expressed as,

$$\mathcal{L}_{+,-}(t) = \sum_{\mathcal{J}} P_{\mathcal{J}} e^{-i\phi_{\mathcal{J}}(t)} \left| \langle \mathcal{J}^-(t) | \mathcal{J}^+(t) \rangle \right| \quad (\text{B10})$$

In FID,  $|\mathcal{J}^{\pm}(t)\rangle = e^{-i\hat{H}^{\pm}t} |\mathcal{J}\rangle$  and  $\phi_{\mathcal{J}}(t) = (\Omega_e + \mathcal{E}_{\mathcal{J}})t$  where  $\mathcal{E}_{\mathcal{J}} = \sum_n j_n a_n$  is the contribution to the electron zeeman splitting from the Overhauser field in the nuclear configuration  $|\mathcal{J}\rangle$ .

### b. Pair correlation approximation and pseudo-spin picture

The solution to the single-system evolution  $|\mathcal{J}^{\pm}(t)\rangle$  is key to both single spin decoherence and ensemble decoherence behaviors under free induction decay and pulse controls. Due to the slowness of the nuclear spin interacting dynamics, this evolution is well described by the pair-correlation approximation for the nuclear spin bath [127, 129]. Within a time  $t$  much smaller than the inverse nuclear interaction strength, the total number of pair-flip excitations  $N_{\text{flip}}$  is much smaller than the number of nuclei  $N$ . The probability of having pair-flips correlated can be estimated to be  $P_{\text{corr}} \sim 1 - e^{-qN_{\text{flip}}^2/N}$  ( $q$  being the number of homo-nuclear nearest neighbors), which is negligible in the relevant timescale of electron spin decoherence [127, 129, 130, 134, 220]. Thus, the pair-flips as elementary excitations from the initial state can be treated as independent of each other, with a relative error  $\epsilon \lesssim P_{\text{corr}}$ . Then the single-system dynamics  $|\mathcal{J}^{\pm}(t)\rangle$  can be described by the excitation of pair-correlations as non-interacting quasi-particles from the ‘‘vacuum’’ state  $|\mathcal{J}\rangle$ , driven by the ‘‘low-energy’’ effective Hamiltonian,

$$\hat{H}_{\mathcal{J}}^{\pm} = \sum_k \hat{\mathcal{H}}_k^{\pm} \equiv \sum_k \mathbf{h}_k^{\pm} \cdot \hat{\sigma}_k / 2, \quad (\text{B11})$$

which has been written in such a way that the pair-correlations are interpreted as 1/2-pseudo-spins, represented by the Pauli matrix  $\hat{\sigma}_k$ , with  $k$  labeling all possible flip-pairs [134]. The time evolution from the initial state  $|\mathcal{J}\rangle$  can be viewed as the rotation of the pseudo-spins, initially all polarized along the  $+z$  pseudo-axis:  $\bigotimes_k |\uparrow_k\rangle$ , under the effective pseudo-magnetic field,

$$\mathbf{h}_k^{\pm} \equiv (\pm 2A_k + 2B_k, 0, D_k \pm E_k), \quad (\text{B12})$$

where, for the electron spin state  $|\pm\rangle$ ,  $\pm A_k$  and  $B_k$  are the pair-flip transition amplitudes contributed by the extrinsic nuclear interaction  $\hat{H}_A$  and the intrinsic nuclear interaction  $\hat{H}_B$ , respectively, and  $D_k$  and  $\pm E_k$  are the energy cost of the pair-flip contributed

by the diagonal nuclear coupling  $\hat{H}_D$  and the hyperfine interaction  $\hat{H}_E$ , respectively. The decoherence then can be analytically derived as

$$\mathcal{L}_{+,-}^s(t) = \prod_k |\langle \psi_k^-(t) | \psi_k^+(t) \rangle| \approx \prod_k e^{-\delta_k^2/2}, \quad (\text{B13})$$

where  $|\psi_k^\pm(t)\rangle$  are the two conjugated states of pseudo-spin  $k$  at time  $t$  conditioned on the electron spin state  $|\pm\rangle$ . In FID,  $|\psi_k^\pm(t)\rangle \equiv e^{-i\hat{H}_k^\pm t} |\uparrow_k\rangle$ ; while with a  $\pi$  pulse to flip the electron at  $t = \tau$ ,  $|\psi_k^\pm(t > \tau)\rangle \equiv e^{-i\hat{H}_k^\pm(t-\tau)} e^{-i\hat{H}_k^\pm\tau} |\uparrow_k\rangle$ .  $\delta_k^2 \equiv 1 - |\langle \psi_k^- | \psi_k^+ \rangle|^2$  possesses a simple geometrical interpretation: the squared distance between the two conjugate pseudo-spin states on the Bloch sphere, which quantifies the entanglement between the electron spin and the pseudo-spin.

A couple of justified simplifications can provide an understanding of the effects of various mechanisms on the spin decoherence. First, the energy cost by the diagonal nuclear coupling ( $D_k$ ) can be neglected as it is by three orders of magnitude smaller than that by hyperfine interaction ( $E_k$ ). Second, for near-neighbor pair-flips, the intrinsic nuclear interaction is much stronger than the hyperfine mediated one for the field strength under consideration. Third, for non-local pair-flips, the intrinsic interaction is negligible due to its finite-range characteristic. Thus we can separate the flip-pairs into two subsets,  $K_A$ , which contains  $O(N^2)$  non-local flip-pairs driven by the effective pseudo-magnetic field  $\mathbf{h}_k^\pm \approx (\pm 2A_k, 0, \pm E_k)$ , and  $K_B$ , which contains  $O(N)$  near-neighbor flip-pairs driven by  $\mathbf{h}_k^\pm \approx (2B_k, 0, \pm E_k)$ . The conjugate pseudo-spins will precess along opposite directions in the non-local subset  $K_A$ , and symmetrically with respect to the  $y$ - $z$  plane in the near-neighbor subset  $K_B$ . The decoherence can be readily grouped by the two different mechanisms as

$$\mathcal{L}_{+,-}^s \cong \prod_{k \in K_B} e^{-\frac{t^4}{2} E_k^2 B_k^2 \text{sinc}^4 \frac{h_k t}{2}} \prod_{k \in K_A} e^{-2t^2 A_k^2 \text{sinc}^2(h_k t)}, \quad (\text{B14})$$

where  $h_k = |\mathbf{h}_k^\pm|$  and  $\text{sinc}(x) \equiv \sin(x)/x$ .

In III-V QDs, because of the large number of nuclear spins, the lost of electron spin coherence is much faster than the build-up of higher-order nuclear spin correlations. The decoherence is therefore well described by the pair-correlation approximation as given in Eq. (B14). In other systems such as Si or diamond NV centers with a dilute nuclear spin bath, corrections from higher-order nuclear spin correlations will become important [129, 220–222].

Lattice distortion can result in local electric field gradients, inducing the quadrupole interaction for nuclear spins with moment greater than  $1/2$ . Recent experimental works have indeed demonstrated signatures of quadrupolar interactions for nuclear spins in InAs self-assembled dot [367, 368]. The quadrupolar interaction can be well incorporated in the theory described in this appendix as contributions to energy cost for nuclear pair-flips [i.e. the  $D_k$  term in Eq. (B12)] when reliable parameter is extracted from experiments. We expect that quadrupolar interaction does not affect electron spin free induction decay and Hahn echo decay where the  $D_k$  term is unimportant, but may affect Carr-Purcell echoes and spin echoes by complex pulse sequences when the  $D_k$  term plays a non-negligible role [127, 130, 134, 221].

### Appendix C: Quantum measurement in Shor's algorithm

We show by explicitly examining Shor's algorithm the crucial role of quantum non-demolition measurement for quantum computation to be scalable.

#### 1. Order finding for Shor's algorithm

For the reader's convenience, we give a brief review of the algorithm for finding the order of a number, the core subroutine for Shor's algorithm. For a comprehensive description of the algorithm, the reader is referred to Ref. [172]. The order  $r$  of a number  $x$  with respect to a number  $N$  is defined by the relation  $x^r = 1 \pmod N$ . For  $2^{L-1} \leq N < 2^L$  and  $1 < x < N$ , the task is to find  $r$  with resources at most polynomial to  $L$ .

The observation is that  $f(n) \equiv x^n \pmod N$  is periodic with period  $r$ , i.e.,  $f(n+r) = f(n)$ , indicating a quantum Fourier transformation (QFT) may be used to find the spectrum of this function and thus to find  $r$ . The algorithm is outlined as follow.

1. Two registers with  $t$  and  $L$  qubits, respectively, are zeroed initially, and thus the initial state is,

$$|00 \cdots 0\rangle |00 \cdots 0\rangle.$$

2. The QFT is applied to the first register to obtain the state,

$$\frac{1}{\sqrt{2^t}} \sum_{n=0}^{2^t-1} |n\rangle |00 \cdots 0\rangle,$$

where  $n = b_1 b_2 \cdots b_t$  is a binary number with  $b_i = 0$  or  $1$ .



3. With the advantage of quantum parallelism, one evaluation of the function  $f(n)$  is added to the second register to reach the state

$$\frac{1}{\sqrt{2^t}} \sum_{n=0}^{2^t-1} |n\rangle |x^n \bmod N\rangle.$$

By  $f(n) = f(n+r)$ , the state can be rewritten as,

$$\frac{1}{\sqrt{2^t}} \sum_{k=0}^{r-1} \sum_{l=0}^{\lfloor (2^t-k)/r \rfloor} |k+lr\rangle |x^k\rangle,$$

where  $\lfloor n/m \rfloor$  denotes the greatest integer not greater than  $n/m$ . Such an expression suggests a solution of the spectrum by QFT.

4. After an inverse QFT applied to the first register, the state becomes,

$$\frac{1}{2^t} \sum_{j=0}^{2^t-1} \sum_{k=0}^{r-1} \sum_{l=0}^{\lfloor (2^t-k)/r \rfloor} e^{-i2\pi \frac{(k+lr)j}{2^t}} |k+lr\rangle |x^k\rangle.$$

If  $2^t$  happens to be an integer multiple of  $r$ , the terminating state is just,

$$\frac{1}{r} \sum_{s=0}^{r-1} \sum_{k=0}^{r-1} e^{-i2\pi ks/r} |2^t s/r\rangle |x^k\rangle,$$

only for  $j = 2^t(s/r)$  will the amplitude be nonzero. Generally,  $r$  would not divide  $2^t$ , but if  $2^t$  is much larger than  $r$ , the spectrum after the QFT will be distribution composed of peaks around  $2^t(s/r)$  for  $(0 \leq s < r)$ . The larger is the first register, the sharper will the peaks be. The probability of the state of the first register being away from  $2^t s/r$  by a distance  $2^p$  is calculated to be less than  $1/(2^{p+1} - 4)$ , so with probability greater than  $1 - 1/(2^{p+1} - 4)$ , the fraction  $s/r$  can be determined up to the first  $t - p$  bits by a measurement of the first  $t - p$  bits of the first register. If  $t - p$  is chosen to be  $2L + 1 \equiv N$ ,  $r$  can be determined from the first  $N$  bits of the binary fraction number  $s/r$ , i.e.,  $\lfloor 2^N s/r \rfloor$ , by continued fraction.

## 2. Issues with the measurement

The key feature of Shor's algorithm is that, though the terminating state is a superposition of many computational basis states  $\sum_x |x\rangle$  (where  $|x\rangle = |b_1 b_2 \cdots b_t\rangle$  with  $b_i = 0$  or  $1$ ), it is not necessary to know all the amplitudes to solve the problem. Actually, an ideal measurement on the computational basis will project the superposition state into an arbitrary basis state which has a nonzero amplitude, and with high probability, the fraction  $s/r$  can be determined up to  $2L + 1$  bits. If the measurement is performed in a single shot, the register may be read out bit by bit, and the superposition state will collapse in a cascade manner, so the resources required by the whole readout step is  $O(L)$  and thus the measurement is scalable. The cascading readout can be illustrated by the example of reading the state  $|000\rangle + |010\rangle + |110\rangle + |111\rangle$ , in which the state collapse may follow the steps shown in Fig. 44. Only  $N$  single-bit measurements are required to have a  $N$ -bit superposition state collapsed into a basis state and only  $N$  bits of classical memory are needed to record the measurement result. So a single-shot measurement on a single quantum register needs less resources than polynomial to the problem size in Shor's algorithm.

## 3. Ensemble measurement

Now we will show, that, in Shor's algorithm, an ensemble measurement requires resources increasing exponentially with the size of the problem. The terminating state of Shor's algorithm can be written as,

$$\frac{1}{r} \sum_{k=0}^{r-1} \sum_{s=0}^{r-1} |\widetilde{s/r}\rangle \otimes |R(s, k)\rangle \otimes |x^k\rangle,$$

where  $\widetilde{s/r}$  denotes the first  $N$  binary bits of  $s/r$ , and  $R(s, k)$  denotes the state of the last  $p$  bits of the first register which are not accurate in describing  $s/r$ . Only the first  $N$  bits of the first register need to be measured. The detected probability is uniformly distributed among the  $r$  states  $|\widetilde{s/r}\rangle$ , which are spaced almost equally by the distance  $2^t/r$ .

a. *Correlated measurement*

Suppose the first  $N$  qubits of the first register are measured with coincidence counting. Each basis state  $|b_1 b_2 \dots b_N\rangle$  could lead to a click in a corresponding channel. To accumulate confidence in an ensemble measurement, a channel should get at least two clicks. In each single-shot trial of the measurement ensemble, the state would collapse into different states. Each output has to be recorded and stored before one of them is confirmed. So the number of recording channels and the size of classical memories used for data storage scale as  $2^N$ , exponentially increasing with the problem size in Shor's algorithm. This requires exponentially increasing physical resources such as spectral resolution or spectrometer bandwidth in spectroscopy.

If the number of available channels and classical memory registers are limited by  $C$ . We may randomly or uniformly choose  $C$   $x$ 's from the  $2^N$  possible numbers. What is the chance that we can receive a signal at any one of these  $C$  channels? As the probability of having a signal in an arbitrary channel is  $\sim 2^{-N}$ , the probability of having signal in any of the  $C$  channels is  $P_C = 2^{-N}C$ . So, for any finite probability  $P_C$ , the number of channels needs to be  $C \sim 2^N P_C$ , increasing exponentially with the problem size.

b. *Uncorrelated measurement*

In an uncorrelated measurement of an  $N$ -qubit register, the ensemble is first divided into  $4^g(N/g)$  portions ( $g$  is a fixed small integer), and every  $4^g$  portions can be used for  $4^g$  independent  $g$ -qubit measurements to obtain the density matrix of these  $g$  qubits. Once the reduced density matrices for all the  $g$ -qubit subsystems have been obtained. One could apply some classical algorithm to re-construct the density matrix of the  $N$  qubits. The re-construction, of course, could not be certain, but the uncertainty nonetheless does not exclude the possibility that one might search for a correct result from all possible states which give the reduced matrix elements. The number of measurements, the number of recording channels, and the size of storage, all these resources scale only linearly with the problem size.

However, there is a fundamental problem underlying the uncorrelated measurement strategy: to yield an  $N$ -qubit output, essentially  $N$  bits of information have been generated. To generate the same amount of information, the  $g$ -qubit reduced density matrices have to be measured with  $N - \ln(N/g)$  bit accuracy. By the rule of thumb in experimental physics, measuring any physical quantity with  $N$ -qubit precision would require resources scaling as  $2^N$ . Only in exceptional cases, may the register state be derived from the knowledge of the reduced density matrices. For instance, if all one-qubit density matrices are pure states, the register state is obviously the outer product of all of them. But in general, it is difficult to determine the register state from the one-qubit density matrices. For example, if all the  $N$  qubits are maximally entangled with other qubits, such as in the states,

$$|0000\rangle + |0011\rangle + |0110\rangle + |1001\rangle + |1100\rangle + |1111\rangle,$$

and,

$$|0000\rangle + |0101\rangle + |1010\rangle + |1111\rangle,$$

the uncorrelated measurement would turn out to be  $N$  maximally mixed density matrices in both cases, from which little information can be obtained about the register state. To determine the order  $r$ , one has to search from all possibilities, of which the number is  $\sim 2^N$ .

Below we will show that, for the first  $N$  qubits in Shor's algorithm, there are  $\sim 2^N$  possible terminating states which would produce almost the same one-qubit reduced density matrix.

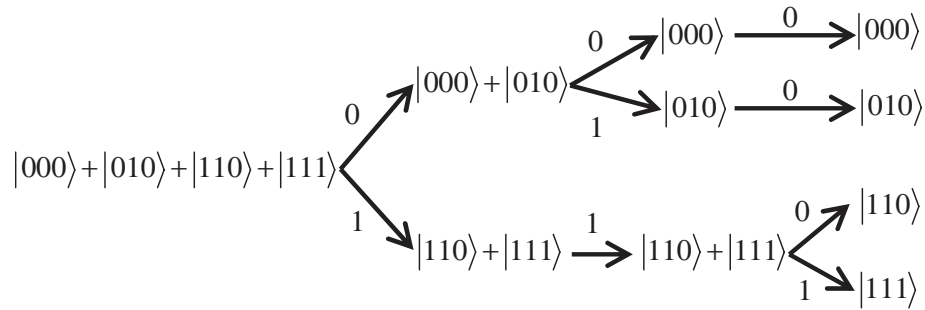


FIG. 44. The collapse (quantum jump) of a multi-qubit state under a measurement of the qubits in sequence. The number associated with each arrow indicates the output of the measurement.

**Lemma 1.** For a state  $\sum_{l=0}^{\lfloor (2^N-1)/k \rfloor} |lk\rangle$  ( $k$  is an odd number greater than 1), the reduced density matrix of any qubit has no off-diagonal term in the computational basis.

**Proof** If there is an off-diagonal term  $\langle 0|\rho|1\rangle$  for the  $j$ th qubit, there have to be at least two states  $|x\rangle$  and  $|x'\rangle$  in the superposition, which are different only at the  $j$ th bit. So we have that  $|x - x'| = 2^{N-j}$  is divided by  $k$ , which is impossible since  $k$  is an odd number  $\square$

**Corollary 1.** For the state  $\sum_{l=0}^{\lfloor (2^N-1)/(2^p k) \rfloor} |l2^p k\rangle$  ( $k$  is an odd number greater than 1), the reduced density matrix of any qubit has no off-diagonal term in the computational basis, and the reduced density matrices of the last  $p$  qubits are all  $|0\rangle\langle 0|$ .

**Corollary 2.** For the state  $\sum_{l=0}^{\lfloor (2^N-1)/2^p \rfloor} |l2^p\rangle$ , the reduced density matrices of the first  $n - p$  qubit are all  $(|0\rangle + |1\rangle) \frac{1}{2} (\langle 0| + \langle 1|)$ , and the reduced density matrices of the last  $p$  qubits are all  $|0\rangle\langle 0|$ .

**Lemma 2.** For the state  $\sum_{l=0}^{\lfloor (2^N-1)/k \rfloor} |lk\rangle$ , if the odd number  $k < 2^{\alpha N/2}$  for a specific number  $\alpha \in (0, 1)$ , the states  $|x\rangle$  with  $x_j = 0$  or 1 have the same probability up to  $cN$ -bit precision to occur in the superposition, where  $c$  is a constant less than 1.

**Proof** The integer numbers  $x = \{x_1 x_2 \cdots x_N\}$  with  $x_j = 0$  or 1 form alternatively  $2^j$  segments with length  $2^{N-j}$ . For an arbitrarily chosen number  $\beta \in (\alpha, 1)$ , the segment length  $2^{N-j}$  is either less or greater than  $2^{\beta N/2}$ . If  $2^{N-j} > 2^{\beta N/2}$ , as the number of the multiples of  $k$  in a segment is greater than  $2^{(\beta-\alpha)N/2}$ . The numbers of multiple  $k$  in two neighboring segments differ by at most 1. So the occurring probability of  $x_j = 0$  is different from that of  $x_j = 1$  by at most  $1/2^{(\beta-\alpha)N/2}$ . If  $2^{N-j} \leq 2^{\beta N/2}$ , we observe that the first  $x$  of every  $k$  segments is  $k2^{N-j}$ , a multiple of  $k$ . As  $k$  is an odd number, each  $k$  segments starting with  $x_j = 0$  will be followed by  $k$  segments starting with  $x_j=1$ , and vice versa, until the end of all segments. So, in every  $2k$  segments, the numbers of  $lk$ 's with  $x_j = 0$  or 1 are exactly the same. As the difference of the occurring numbers in 2 neighboring segments is at most 1, the difference in  $k$  segments is at most  $(k+1)/2$ . So, the difference of the occurring probability in all the segments is at most  $(k+1)2^{N-j}/2^{N+1} < 1/2^{N(1-\alpha/2-\beta/2)}$ . Let  $c = \min(1 - \alpha/2 - \beta/2, \beta/2 - \alpha/2)$ , we have the probability of occurring of  $x_j = 0$  is the same as that of occurring of  $x_j = 1$ , accurate up to  $cN$  bits  $\square$

From the Lemma 1 and 2, we have directly the following theorem.

**Theorem 1.** For all states  $\sum_{l=0}^{\lfloor (2^N-1)/k \rfloor} |lk\rangle$  [ $k$  is an odd number, and  $k < 2^{\alpha n/2}$  for a specific number  $\alpha \in (0, 1)$ ], all one-qubit reduced density matrices obtained by uncorrelated measurements are the same up to  $cN$  significant bits.

**Corollary 3.** For all states  $\sum_{l=0}^{\lfloor (2^N-1)/(2^p k) \rfloor} |l2^p k\rangle$  [ $k$  is an odd number, and  $k < 2^{\alpha N/2}$  for a specific number  $\alpha \in (0, 1)$ ], all one-qubit reduced density matrices obtained by uncorrelated measurements are the same with  $cN$  significant bits.

The theorem and corollary above are consistent with a theorem recently proved by Popescu et al [369]: Almost all  $N$ -qubit states would give almost the same  $g$ -qubit reduced density matrix, as long as  $N$  is large and  $N \gg g$ .

The terminating states of the register to be measured in Shor's algorithm have the form of the superposition states in the theorem above, with at most one-bit deviation. So, unless at least the density of matrix of one qubit is measured with  $O(N)$  effective bits, there are  $\sim 2^N$  possible superpositions corresponding to the same set of one-qubit reduced density matrices. On the one hand, searching the correct one from all those possibilities needs resources  $\sim 2^N$  in all known classical or quantum algorithms. On the other hand, determining the density matrix of a qubit with  $O(N)$ -bit accuracy also requires resources  $\sim 2^N$ . So uncorrelated single-qubit ensemble measurement is provably unscalable for Shor's algorithm. Though there is no proof in general cases, it would be rather surprising that some ensemble measurement scheme is scalable for Shor's algorithm.

#### 4. Single-object measurement with error

In general, scalable quantum computation needs to be performed on a single quantum object (rather than an ensemble) with single-shot measurement. In reality, detectors used in the readout procedure have unavoidable inefficiency or errors. Thus, the Kraus operators [172] for a POVM (positive operator-valued measure) of a certain qubit can be written as

$$A_0 = \sqrt{1-d}|0\rangle\langle 0| + \sqrt{1-e}|1\rangle\langle 1|, \quad (C1a)$$

$$A_1 = \sqrt{d}|0\rangle\langle 0| + \sqrt{e}|1\rangle\langle 1|, \quad (C1b)$$

with detector efficiency  $e$  and dark count rate  $d$ . For a state  $|\psi\rangle$ , the probability and the resultant state for the output 0 and 1 are, respectively,

$$P_0 = \langle \psi | A_0^\dagger A_0 | \psi \rangle \text{ and } A_0 | \psi \rangle, \quad (C2a)$$

$$P_1 = \langle \psi | A_1^\dagger A_1 | \psi \rangle \text{ and } A_1 | \psi \rangle, \quad (C2b)$$

Suppose that the detecting error rate at each qubit is greater than a finite number  $\varepsilon$ , the probability of reading out a  $N$ -qubit register is less than  $(1 - \varepsilon)^N$ , exponentially small with increasing the size of the register. A single-shot measurement then is insufficient for scalable quantum computation. Thus, if there exist detector errors as always, the measurement has to be repeated for enough times to obtain sufficient confidence in a readout result. Furthermore, if the measurement is destructive, the quantum computation has to be rewound from the very beginning of the algorithm, making the measurement equivalent to an ensemble measurement.

In an uncorrelated measurement, different qubits of the register are measured and recorded independently, and the error rate at each bit is finite, so the density matrices of each qubit of the register can be measured by repeating the quantum computation for a number of times proportional to the register size. But the problem here is the same as discussed for the uncorrelated measurement in the previous section.

In a correlated measurement, the probability of correctly reading out the projected state is exponentially small [ $\sim (1 - \varepsilon)^N$ ], and yet the probability of the terminating state collapsing into the same basis state is also exponentially small ( $< 1/r$ ). So before a readout result is repeated once for accumulating sufficient confidence, the quantum computation has to be repeated a number of times which increases exponentially with the problem size.

### 5. Quantum non-demolition measurement

In a QND measurement, the state will remain unchanged after the projection into the measurement basis (which is also the computational basis). So the readout can be repeated many times in every qubit to accumulate confidence of the readout result, without rewinding the whole algorithm from the beginning.

Now we calculate the resources required in reading out the state of a  $N$ -qubit register. If the error rate in reading out each qubit by an  $M$ -shot QND measurement is  $\varepsilon_M$ , the probability of successfully reading out the register is  $(1 - \varepsilon_M)^N$ . To have a finite success probability, we require  $s_N \equiv (1 - \varepsilon_M)^N > s$  where  $s$  is a finite number smaller than 1. When  $\varepsilon_M$  is small,  $s_N \approx e^{-N\varepsilon_M}$ , so we require the error rate of a  $M$ -shot QND measurement  $\varepsilon_M < -(1/N) \ln s$ .

To obtain the error rate of a  $M$ -shot measurement, we define its POVM's. The Kraus operators for the POVM of a  $M$ -shot measurement giving  $m$  photon counts can be derived as,

$$\begin{aligned} A_{M,m} &= \binom{M}{m}^{1/2} (1-d)^{(M-m)/2} d^{m/2} |0\rangle\langle 0| \\ &+ \binom{M}{m}^{1/2} (1-e)^{(M-m)/2} e^{m/2} |1\rangle\langle 1| \\ &\equiv \sqrt{d_{M,m}} |0\rangle\langle 0| + \sqrt{e_{M,m}} |1\rangle\langle 1|. \end{aligned} \quad (C3)$$

When  $d_{M,m} < e_{M,m}$ , it is more probable that the qubit is in the state  $|1\rangle$ , and vice versa. As

$$d_{M,m}/e_{M,m} = \left( \frac{1-d}{1-e} \right)^M \left[ \frac{d(1-e)}{e(1-d)} \right]^m. \quad (C4)$$

monotonically decreases with  $m$ , we can define a  $m_0$  so that all  $A_{M,m < m_0}$  are indicators of  $|0\rangle$  and all  $A_{M,m > m_0}$  are indicators of  $|1\rangle$ , with the  $m_0$  given by  $d_{M,m_0}/e_{M,m_0} = 1$  or,

$$m_0 = \frac{M \ln \frac{1-d}{1-e}}{\ln \frac{1-d}{1-e} + \ln \frac{e}{d}} \equiv \alpha M. \quad (C5)$$

As  $d_{M,m}$  and  $e_{M,m}$  as functions of  $m$  have peaks at  $dM$  and  $eM$ , respectively, we have,

$$d < \alpha < e. \quad (C6)$$

Now the POVM can be calculated from,

$$\begin{aligned} P_0^{(M)} &\equiv \sum_{m < m_0} A_{M,m}^\dagger A_{M,m} \equiv (1-d_M) |0\rangle\langle 0| + (1-e_M) |1\rangle\langle 1|, \\ P_1^{(M)} &\equiv \sum_{m \geq m_0} A_{M,m}^\dagger A_{M,m} \equiv d_M |0\rangle\langle 0| + e_M |1\rangle\langle 1|, \end{aligned}$$

where,

$$\begin{aligned}
 d_M &= \sum_{m \geq m_0} d_{M,m} = \sum_{m \geq m_0} \binom{M}{m} (1-d)^{M-m} d^m \\
 &= \frac{M!}{(M-m_0)!(m_0-1)!} \int_{1-d}^1 t^{M-m_0} (1-t)^{m_0-1} dt \\
 &< \frac{M!(1-d)^{M-m_0} d^{m_0}}{(M-m_0)!(m_0-1)!} \\
 &\sim \sqrt{\frac{\alpha M}{2\pi(1-\alpha)}} \left[ \frac{(1-d)^{1-\alpha} d^\alpha}{(1-\alpha)^{1-\alpha} \alpha^\alpha} \right]^M,
 \end{aligned} \tag{C7}$$

and similarly,

$$1 - e_M < \sqrt{\frac{\alpha M(1-e)^2}{2\pi(1-\alpha)e^2}} \left[ \frac{(1-e)^{1-\alpha} e^\alpha}{(1-\alpha)^{1-\alpha} \alpha^\alpha} \right]^M. \tag{C8}$$

The error rate is defined as  $\varepsilon_M = \max(d_M, 1 - e_M)$ , so the number of required QND measurements per qubit  $M \sim \ln N$ , and the total number of measurement is proportional to  $N \ln N$ . So a QND is scalable. In experiment,  $e$  and  $d$  cannot be determined exactly, but fortunately  $\alpha$  need not be determined exactly and whenever it is between  $d$  and  $e$ , the results for  $d_M$  and  $e_M$  are unchanged in the equations above.

Note that with the aid of entanglement gates and a supply of fresh qubits, a destructive measurement can be converted into a QND one. The idea is based on the transformation of a qubit and  $M$  zeroed auxiliary qubits into an entangled state by  $M$  entanglement gates:

$$(\alpha|0\rangle + \beta|1\rangle) \bigotimes_{m=0}^{M-1} |0\rangle \implies \alpha|0\rangle \bigotimes_{m=0}^{M-1} |0\rangle + \beta|1\rangle \bigotimes_{m=0}^{M-1} |1\rangle.$$

The  $M$  auxiliary qubits are to be read out. As all these qubits are entangled, once one qubit is collapsed into a basis state  $|0\rangle$  or  $|1\rangle$ , all the qubits will be collapsed into the same state. So even a destructive measurement with detecting error can be used to read out the qubit.

How about a QND measurement with back-action noise, i.e., reaction to measurement that disturbs the state after a measurement cycle? With the idea above for converting destructive measurement into a QND one, we can employ the concept of

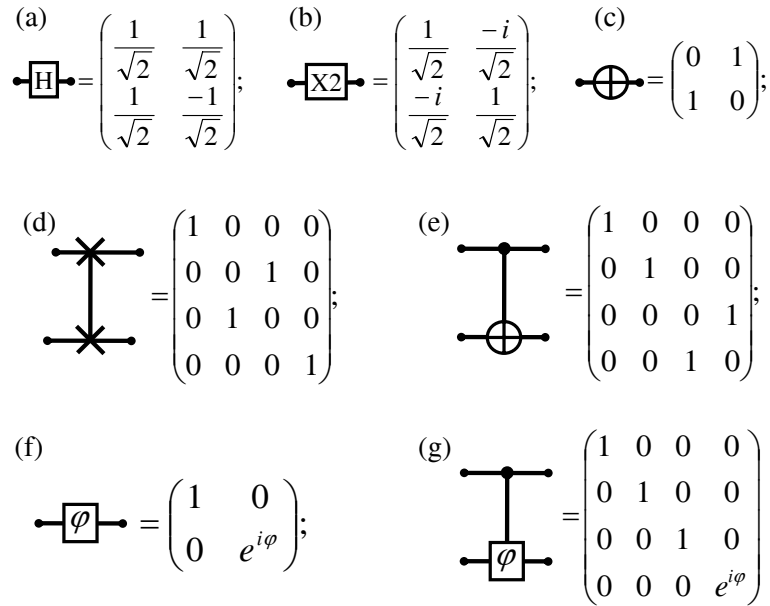


FIG. 45. Some elementary quantum gates and their matrix representation, including (a) Hadamard ( $H$ ), (b) rotation of 90 degrees about the  $x$ -axis ( $X2$ ), (c) NOT ( $N$ ), (d) SWAP ( $W$ ), (e) Controlled NOT ( $C$ ), (f) single-bit phase-shift ( $S_\phi$ ), and (g) Controlled phase-shift ( $P_\phi$ ).

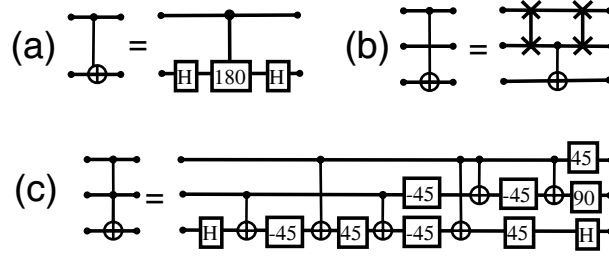


FIG. 46. Realization of several control gates, including (a) CNOT, (b) remote CNOT, and (c) Toffoli ( $C_2$ ).

*fault-tolerant measurement* to deal with this problem. In the so-called fault-tolerant measurement, a qubit is first encoded into a stabilizer code, after a single measurement, any back-action noise will be diagnosed and corrected using the error syndrome since this noise acts only on a single qubit (by assumption). After the error correction, another measurement would be performed, and so on. The fault-tolerant measurement thus allows an imperfect QND measurement to read out the result of a quantum algorithm with polynomial resources.

#### Appendix D: Elementary quantum gates

Here we define a series of elementary quantum gates used in the quantum circuits presented in Sec. VIII A. The quantum gates of interest are defined in Figs. 45 and 46. The Hadamard gate can be realized by the spin rotation operations up to a trivial global phase, as the transformation operator for the Hadamard gate can be expressed in terms of spin rotations as  $H = e^{i\pi/2} e^{i\pi s_x} e^{i\pi s_y/2}$ . The CNOT gate can be realized by the controlled  $\pi$ -phase gate together with two Hadamard gates. The CNOT gate on two remote bits can be realized by a local CNOT gate plus some SWAP gates. The doubly controlled NOT (Toffoli) gate can be realized by six CNOT gates plus some single-qubit gates. The controlled  $\pi$ -phase gate and the CNOT gate can be realized by two  $\sqrt{\text{SWAP}}$  gates plus some single-spin rotations. As any controlled phase gate can be realized by two CNOT gates plus some single-qubit gates, the circuits in Figs. 38 and 39 can be alternatively realized with  $\sqrt{\text{SWAP}}$  gates as well.

- 
- [1] P. W. Shor, in *Proceedings of the 35th Annual Symposium on Foundations of Computer Sciences*, edited by E. S. Goldwasser (IEEE press, Los Alamitos, California, 1994) pp. 124–134.
  - [2] D. DiVincenzo, *Fortschr. Der Physik* **48**, 771 (2000).
  - [3] L. M. K. Vandersypen, M. Steffen, G. Breyta, C. S. Yannoni, M. H. Sherwood, and I. L. Chuang, *Nature* **414**, 883 (December 2001).
  - [4] N. A. Gershenfeld and I. L. Chuang, *Science* **275**, 350 (JAN 17 1997).
  - [5] I. L. Chuang, L. M. K. Vandersypen, X. L. Zhou, D. W. Leung, and S. Lloyd, *Nature* **393**, 143 (MAY 14 1998).
  - [6] J. A. Jones and M. Mosca, *J. Chem. Phys.* **109**, 1648 (AUG 1 1998).
  - [7] D. G. Cory, M. D. Price, and T. F. Havel, *Physica D* **120**, 82 (SEP 1 1998).
  - [8] J. I. Cirac and P. Zoller, *Phys. Rev. Lett.* **74**, 4091 (MAY 15 1995).
  - [9] C. Monroe, D. M. Meekhof, B. E. King, W. M. Itano, and D. J. Wineland, *Phys. Rev. Lett.* **75**, 4714 (DEC 18 1995).
  - [10] A. Sorensen and K. Molmer, *Phys. Rev. Lett.* **82**, 1971 (1999).
  - [11] J. L. Cirac and P. Zoller, *Nature* **404**, 579 (APR 6 2000).
  - [12] R. Folman, P. Kruger, D. Cassettari, B. Hessmo, T. Maier, and J. Schmiedmayer, *Phys. Rev. Lett.* **84**, 4749 (MAY 15 2000).
  - [13] D. Kielpinski, C. Monroe, and D. J. Wineland, *Nature* **417**, 709 (JUN 13 2002).
  - [14] S. Gulde, M. Riebe, G. P. T. Lancaster, C. Becher, J. Eschner, H. Haffner, F. Schmidt-Kaler, I. L. Chuang, and R. Blatt, *Nature* **421**, 48 (JAN 2 2003).
  - [15] D. Leibfried, B. DeMarco, V. Meyer, D. Lucas, M. Barrett, J. Britton, W. M. Itano, B. Jelenkovic, C. Langer, T. Rosenband, and D. J. Wineland, *Nature* **422**, 412 (MAR 27 2003).
  - [16] F. Schmidt-Kaler, H. Haffner, M. Riebe, S. Gulde, G. P. T. Lancaster, T. Deuschle, C. Becher, C. F. Roos, J. Eschner, and R. Blatt, *Nature* **422**, 408 (MAR 27 2003).
  - [17] D. Leibfried, E. Knill, S. Seidelin, J. Britton, R. B. Blakestad, J. Chiaverini, D. B. Hume, W. M. Itano, J. D. Jost, C. Langer, R. Ozeri, R. Reichle, and D. J. Wineland, *Nature* **438**, 639 (DEC 1 2005).
  - [18] J. Benhelm, G. Kirchmair, C. F. Roos, and R. Blatt, *Nature Phys.* **4**, 463 (JUN 2008).
  - [19] G. K. Brennen, C. M. Caves, P. S. Jessen, and I. H. Deutsch, *Phys. Rev. Lett.* **82**, 1060 (FEB 1 1999).
  - [20] D. Jaksch, H. J. Briegel, J. I. Cirac, C. W. Gardiner, and P. Zoller, *Phys. Rev. Lett.* **82**, 1975 (MAR 1 1999).
  - [21] D. Jaksch, J. I. Cirac, P. Zoller, S. L. Rolston, R. Cote, and M. D. Lukin, *Phys. Rev. Lett.* **85**, 2208 (SEP 4 2000).

- [22] O. Mandel, M. Greiner, A. Widera, T. Rom, T. W. Hansch, and I. Bloch, *Nature* **425**, 937 (OCT 30 2003).
- [23] M. Anderlini, P. J. Lee, B. L. Brown, J. Sebby-Strabley, W. D. Phillips, and J. V. Porto, *Nature* **448**, 452 (JUL 26 2007).
- [24] S. Trotzky, P. Cheinet, S. Foelling, M. Feld, U. Schnorrberger, A. M. Rey, A. Polkovnikov, E. A. Demler, M. D. Lukin, and I. Bloch, *Science* **319**, 295 (JAN 18 2008).
- [25] E. Knill, R. Laflamme, and G. J. Milburn, *Nature* **409**, 46 (JAN 4 2001).
- [26] J. L. O'Brien, G. J. Pryde, A. G. White, T. C. Ralph, and D. Branning, *Nature* **426**, 264 (NOV 20 2003).
- [27] R. Raussendorf, D. E. Browne, and H. J. Briegel, *Phys. Rev. A* **68**, 022312 (AUG 2003).
- [28] M. A. Nielsen, *Phys. Rev. Lett.* **93**, 040503 (JUL 23 2004).
- [29] P. Walther, K. J. Resch, T. Rudolph, E. Schenck, H. Weinfurter, V. Vedral, M. Aspelmeyer, and A. Zeilinger, *Nature* **434**, 169 (MAR 10 2005).
- [30] D. E. Browne and T. Rudolph, *Phys. Rev. Lett.* **95**, 010501 (JUL 1 2005).
- [31] Y. Lim, A. Beige, and L. C. Kwek, *Phys. Rev. Lett.* **95**, 030505 (JUL 15 2005).
- [32] R. Prevedel, P. Walther, F. Tiefenbacher, P. Bohl, R. Kaltenbaek, T. Jennewein, and A. Zeilinger, *Nature* **445**, 65 (JAN 4 2007).
- [33] C. Y. Lu, D. E. Browne, T. Yang, and J. W. Pan, *Phys. Rev. Lett.* **99**, 250504 (DEC 21 2007).
- [34] M. Varnava, D. E. Browne, and T. Rudolph, *Phys. Rev. Lett.* **1**, 060502 (FEB 15 2008).
- [35] A. Shnirman, G. Schon, and Z. Hermon, *Phys. Rev. Lett.* **79**, 2371 (SEP 22 1997).
- [36] D. Averin, *Sold State Communication* **105**, 659 (MAR 1998).
- [37] Y. Makhlin, G. Schon, and A. Shnirman, *Nature* **398**, 305 (MAR 25 1999).
- [38] Y. Nakamura, Y. A. Pashkin, and J. S. Tsai, *Nature* **398**, 786 (APR 29 1999).
- [39] Y. Makhlin, G. Schon, and A. Shnirman, *Rev. Mod. Phys.* **73**, 357 (APR 2001).
- [40] Y. Yu, S. Y. Han, X. Chu, S. I. Chu, and Z. Wang, *Science* **296**, 889 (MAY 3 2002).
- [41] J. M. Martinis, S. Nam, J. Aumentado, and C. Urbina, *Phys. Rev. Lett.* **89**, 117901 (SEP 9 2002).
- [42] I. Chiorescu, Y. Nakamura, C. J. P. M. Harmans, and J. E. Mooij, *Science* **299**, 1869 (MAR 21 2003).
- [43] T. Yamamoto, Y. A. Pashkin, O. Astafiev, Y. Nakamura, and J. S. Tsai, *Nature* **425**, 941 (OCT 30 2003).
- [44] F. W. Strauch, P. R. Johnson, A. J. Dragt, C. J. Lobb, J. R. Anderson, and F. C. Wellstood, *Phys. Rev. Lett.* **91**, 167005 (OCT 17 2003).
- [45] A. Blais, A. van den Brink, and A. Zagoskin, *Phys. Rev. Lett.* **90**, 127901 (MAR 28 2003).
- [46] M. Grajcar, A. Izmailkov, S. H. W. van der Ploeg, S. Linzen, T. Plecenik, T. Wagner, U. Hubner, E. Il'ichev, H. G. Meyer, A. Y. Smirnov, P. J. Love, A. van den Brink, M. H. S. Amin, S. Uchaikin, and A. M. Zagoskin, *Phys. Rev. Lett.* **96**, 047006 (FEB 3 2006).
- [47] A. Wallraff, D. Schuster, A. Blais, L. Frunzio, R. Huang, J. Majer, S. Kumar, S. Girvin, and R. Schoelkopf, *Nature* **431**, 162 (SEP 9 2004).
- [48] A. O. Niskanen, K. Harrabi, F. Yoshihara, Y. Nakamura, S. Lloyd, and J. S. Tsai, *Science* **316**, 723 (May 2007).
- [49] J. Majer, J. M. Chow, J. M. Gambetta, J. Koch, B. R. Johnson, J. A. Schreier, L. Frunzio, D. I. Schuster, A. A. Houck, A. Wallraff, A. Blais, M. H. Devoret, S. M. Girvin, and R. J. Schoelkopf, *Nature* **449**, 443 (SEP 27 2007).
- [50] M. Neeley, M. Ansmann, R. C. Bialczak, M. Hofheinz, E. Lucero, A. D. O'Connell, D. Sank, H. Wang, J. Wenner, A. N. Cleland, M. R. Geller, and J. M. Martinis, *Science* **325**, 722 (AUG 7 2009).
- [51] M. Hofheinz, H. Wang, M. Ansmann, R. C. Bialczak, E. Lucero, M. Neeley, A. D. O'Connell, D. Sank, J. Wenner, J. M. Martinis, and A. N. Cleland, *Nature* **459**, 546 (MAY 28 2009).
- [52] L. DiCarlo, J. M. Chow, J. M. Gambetta, L. S. Bishop, B. R. Johnson, D. I. Schuster, J. Majer, A. Blais, L. Frunzio, S. M. Girvin, and R. J. Schoelkopf, *Nature* **460**, 240 (Jul. 2009), ISSN 0028-0836.
- [53] J. Q. You and F. Nori, *Phys. Today* **58**, 42 (NOV 2005).
- [54] J. Clarke and F. K. Wilhelm, *Nature* **453**, 1031 (JUN 19 2008).
- [55] J. M. Martinis, *Quantum Info. Proc.* **8**, 81 (JUN 2009).
- [56] P. M. Platzman and M. I. Dykman, *Science* **284**, 1967 (JUN 18 1999).
- [57] M. J. Lea, P. G. Frayne, and Y. Mukharsky, *Fortschr. Der Physik* **48**, 1109 (2000).
- [58] A. J. Dahm, J. M. Goodkind, I. Karakurt, and S. Pilla, *J. Low Temp. Phys.* **126**, 709 (JAN 2002).
- [59] S. A. Lyon, *Phys. Rev. A* **74**, 052338 (NOV 2006).
- [60] M. N. Leuenberger and D. Loss, *Nature* **410**, 789 (APR 12 2001).
- [61] B. E. Kane, *Nature* **393**, 133 (May 1998).
- [62] T. D. Ladd, J. R. Goldman, F. Yamaguchi, Y. Yamamoto, E. Abe, and K. M. Itoh, *Phys. Rev. Lett.* **89**, 017901 (JUL 1 2002).
- [63] D. Loss and D. P. DiVincenzo, *Phys. Rev. A* **57**, 120 (January 1998).
- [64] A. Imamoglu, D. D. Awschalom, G. Burkard, D. P. DiVincenzo, D. Loss, M. Sherwin, and A. Small, *Phys. Rev. Lett.* **83**, 4204 (November 1999).
- [65] G. Burkard, D. Loss, and D. P. DiVincenzo, *Phys. Rev. B* **59**, 2070 (JAN 15 1999).
- [66] R. Vrijen, E. Yablonoitch, K. Wang, H. W. Jiang, A. Balandin, V. Roychowdhury, T. Mor, and D. DiVincenzo, *Phys. Rev. A* **62**, 012306 (JUL 2000).
- [67] V. Cerletti, W. A. Coish, O. Gywat, and D. Loss, *Nanotech.* **16**, R27 (2005).
- [68] T. Calarco, A. Datta, P. Fedichev, E. Pazy, and P. Zoller, *Phys. Rev. A* **68**, 012310 (2003).
- [69] E. Pazy, E. Biolatti, T. Calarco, I. D'amico, P. Zanardi, F. Rossi, and P. Zoller, *Europhys. Lett.* **62**, 175 (2003).
- [70] A. Nazir, B. W. Lovett, S. D. Barrett, T. P. Spiller, and G. A. D. Briggs, *Phys. Rev. Lett.* **93**, 150502 (2004).
- [71] B. W. Lovett, E. Pazy, A. Nazir, S. D. Barrett, T. P. Spiller, and G. A. D. Briggs, *Phys. Rev. B* **72**, 115324 (2005).
- [72] P. Chen, C. Piermarocchi, L. J. Sham, D. Gammon, and D. G. Steel, *Phys. Rev. B* **69**, 075320 (2004).
- [73] C. Piermarocchi, P. Chen, L. J. Sham, and D. G. Steel, *Phys. Rev. Lett.* **89**, 167402 (October 2002).
- [74] G. Ramon, Y. Lyanda-Geller, T. L. Reinecke, and L. J. Sham, *Phys. Rev. B* **71**, 121305 (MAR 2005).
- [75] C. Emary and L. J. Sham, *Phys. Rev. B* **75**, 125317 (MAR 2007).

- [76] S. M. Clark, K.-M. C. Fu, T. D. Ladd, and Y. Yamamoto, *Phys. Rev. Lett.* **99**, 040501 (JUL 27 2007).
- [77] S. E. Economou and T. L. Reinecke, *Phys. Rev. Lett.* **99**, 217401 (NOV 23 2007).
- [78] A. J. Ramsay, S. J. Boyle, R. S. Kolodka, J. B. B. Oliveira, J. Skiba-Szymanska, H. Y. Liu, M. Hopkinson, A. M. Fox, and M. S. Skolnick, *Phys. Rev. Lett.* **100**, 197401 (MAY 16 2008).
- [79] D. Press, T. D. Ladd, B. Zhang, and Y. Yamamoto, *Nature* **456**, 218 (NOV 13 2008).
- [80] B. Eble, C. Testelin, P. Desfonds, F. Bernardot, A. Balocchi, T. Amand, A. Miard, A. Lemaitre, X. Marie, and M. Chamorro, *Phys. Rev. Lett.* **102**, 146601 (2009).
- [81] J. Fischer, W. A. Coish, D. V. Bulaev, and D. Loss, *Phys. Rev. B* **78**, 155329 (2008).
- [82] R. G. Clark, R. Brenner, T. M. Buehler, V. Chan, N. J. Curson, A. S. Dzurak, E. Gauja, H. S. Goan, A. D. Greentree, T. Hallam, A. R. Hamilton, L. C. L. Hollenberg, D. N. Jamieson, J. C. McCallum, G. J. Milburn, J. L. O'Brien, L. Oberbeck, C. I. Pakes, S. D. Prawer, D. J. Reilly, F. J. Ruess, S. R. Schofield, M. Y. Simmons, F. E. Stanley, R. P. Starrett, C. Wellard, and C. Yang, *Phil. Trans. Royal Soc. London A* **361**, 1451 (2003).
- [83] S. R. Schofield, N. J. Curson, M. Y. Simmons, F. J. Ruess, T. Hallam, L. Oberbeck, and R. G. Clark, *Phys. Rev. Lett.* **91**, 136104 (2003).
- [84] F. R. Bradbury, A. M. Tyryshkin, G. Sabouret, J. Bokor, T. Schenkel, and S. Lyon, *Phys. Rev. Lett.* **97**, 176404 (2006).
- [85] H. Huebl, A. R. Stegner, M. Stutzmann, M. S. Brandt, G. Vogg, F. Bensch, E. Rauls, and U. Gerstmann, *Phys. Rev. Lett.* **97**, 166402 (2006).
- [86] A. R. Stegner, C. Boehme, H. Huebl, M. Stutzmann, K. Lips, and M. S. Brandt, *Nature Phys.* **2**, 835 (2006).
- [87] J. Wrachtrup, S. Y. Kilin, and A. P. Nizovtsev, *Optics and Spectroscopy* **91**, 429 (2001).
- [88] F. Jelezko, I. Popa, A. Gruber, C. Tietz, J. Wrachtrup, A. Nizovtsev, and S. Kilin, *App. Phys. Lett.* **81**, 2160 (2002).
- [89] T. A. Kennedy, J. S. Colton, J. E. Butler, R. C. Linares, and P. J. Doering, *Appl. Phys. Lett.* **83**, 4190 (2003).
- [90] F. Jelezko, T. Gaebel, I. Popa, A. Gruber, and J. Wrachtrup, *Phys. Rev. Lett.* **92**, 076401 (2004).
- [91] F. Jelezko, T. Gaebel, I. Popa, M. Domhan, A. Gruber, and J. Wrachtrup, *Phys. Rev. Lett.* **93**, 130501 (2004).
- [92] C. Santori, P. Tamarat, P. Neumann, J. Wrachtrup, D. Fattal, R. G. Beausoleil, J. Rabeau, P. Olivero, A. D. Greentree, S. Prawer, F. Jelezko, and P. R. Hemmer, *Phys. Rev. Lett.* **97**, 247401 (2006).
- [93] R. J. Epstein, F. M. Mendoza, Y. K. Kato, and D. D. Awschalom, *Nature Phys.* **1**, 94 (2005).
- [94] T. Gaebel, M. Domhan, I. Popa, C. Wittmann, P. Neumann, F. Jelezko, J. R. Rabeau, N. Stavrias, A. D. Greentree, S. Prawer, J. Meijer, J. Twamley, P. R. Hemmer, and J. Wrachtrup, *Nature Phys.* **2**, 408 (2006).
- [95] R. Hanson, F. M. Mendoza, R. J. Epstein, and D. D. Awschalom, *Phys. Rev. Lett.* **97**, 087601 (2006).
- [96] R. Hanson, O. Gywat, and D. D. Awschalom, *Phys. Rev. B* **74**, 161203(R) (2006).
- [97] L. Childress, M. V. Gurudev Dutt, J. M. Taylor, A. S. Zibrov, F. Jelezko, J. Wrachtrup, P. R. Hemmer, and M. D. Lukin, *Science* **314**, 281 (2006).
- [98] M. V. Gurudev Dutt, L. Childress, L. Jiang, E. Togan, J. Maze, F. Jelezko, A. S. Zibrov, P. R. Hemmer, and M. D. Lukin, *Science* **316**, 1312 (2007).
- [99] R. Hanson, V. V. Dobrovitski, A. E. Feiguin, O. Gywat, and D. D. Awschalom, *Science* **320**, 352 (2008).
- [100] J. Wrachtrup and F. Jelezko, *J. Phys. - Cond. Mat.* **18**, S807 (2006).
- [101] A. Y. Kitaev, *Ann. Phys.* **303**, 2 (JAN 2003).
- [102] M. H. Freedman, A. Kitaev, M. J. Larsen, and Z. H. Wang, *Bull. Am. Math. Soc.* **40**, 31 (2003).
- [103] S. Das Sarma, M. Freedman, and C. Nayak, *Phys. Rev. Lett.* **94**, 166802 (APR 29 2005).
- [104] M. Dolev, M. Heiblum, V. Umansky, A. Stern, and D. Mahalu, *Nature* **452**, 829 (APR 17 2008).
- [105] I. P. Radu, J. B. Miller, C. M. Marcus, M. A. Kastner, L. N. Pfeiffer, and K. W. West, *Science* **320**, 899 (MAY 16 2008).
- [106] J. M. Taylor, C. M. Marcus, and M. D. Lukin, *Phys. Rev. Lett.* **90**, 206803 (2003).
- [107] W. M. Witzel and S. Das Sarma, *Phys. Rev. B* **76**, 045218 (2007).
- [108] J. R. Petta, A. C. Johnson, J. M. Taylor, E. A. Laird, A. Yacoby, M. D. Lukin, C. M. Marcus, M. P. Hanson, and A. C. Gossard, *Science* **309**, 2180 (2005).
- [109] A. Greilich, D. R. Yakovlev, A. Shabaev, A. L. Efros, I. A. Yugova, R. Oulton, V. Stavarache, D. Reuter, A. Wieck, and M. Bayer, *Science* **313**, 341 (2006).
- [110] A. M. Tyryshkin, S. A. Lyon, A. V. Astashkin, and A. M. Raitsimring, *Phys. Rev. B* **68**, 193207 (2003).
- [111] E. Abe, J. Isoya, and K. M. Itoh, *J. Supercond.* **18**, 157 (2005).
- [112] A. S. Bracker, E. A. Stinaff, D. Gammon, M. E. Ware, J. G. Tischler, A. Shabaev, A. L. Efros, D. Park, D. Gershoni, V. L. Korenev, and I. A. Merkulov, *Phys. Rev. Lett.* **94**, 047402 (2005).
- [113] S. Takahashi, R. Hanson, J. van Tol, M. S. Sherwin, and D. D. Awschalom, *Phys. Rev. Lett.* **101**, 047601 (2008).
- [114] G. Ramon and X. Hu, *Phys. Rev. B* **75**, 161301 (2007).
- [115] D. J. Reilly, J. M. Taylor, J. R. Petta, C. M. Marcus, M. P. Hanson, and A. C. Gossard, *Science* **321**, 817 (2008).
- [116] C. X. Deng and X. D. Hu, *Phys. Rev. B* **72**, 165333 (2005).
- [117] F. Jelezko, T. Gaebel, I. Popa, M. Domhan, A. Gruber, and J. Wrachtrup, *Phys. Rev. Lett.* **93**, 130501 (2004).
- [118] W. Yao, R. B. Liu, and L. J. Sham, *Phys. Rev. Lett.* **92**, 217402 (2004).
- [119] W. Yao, R. B. Liu, and L. J. Sham, *Phys. Rev. Lett.* **95**, 030504 (July 2005).
- [120] R. B. Liu, W. Yao, and L. J. Sham, *Phys. Rev. B* **72**, 081306(R) (2005).
- [121] A. V. Khaetskii, D. Loss, and L. Glazman, *Phys. Rev. Lett.* **88**, 186802 (May 2002).
- [122] J. Schliemann, A. V. Khaetskii, and D. Loss, *Phys. Rev. B* **66**, 245303 (2002).
- [123] R. de Sousa and S. Das Sarma, *Phys. Rev. B* **68**, 115322 (September 2003).
- [124] W. A. Coish and D. Loss, *Phys. Rev. B* **70**, 195340 (May 2004).
- [125] N. Shenvi, R. de Sousa, and K. B. Whaley, *Phys. Rev. B* **71**, 224411 (2005).
- [126] W. M. Witzel, R. de Sousa, and S. Das Sarma, *Phys. Rev. B* **72**, 161306(R) (2005).



- [127] W. Yao, R. B. Liu, and L. J. Sham, Phys. Rev. B **74**, 195301 (2006).
- [128] C. Deng and X. Hu, Phys. Rev. B **73**, 241303(R) (2006).
- [129] S. K. Saikin, W. Yao, and L. J. Sham, Phys. Rev. B **75**, 125314 (2007).
- [130] R. B. Liu, W. Yao, and L. J. Sham, New J. Phys. **9**, 226 (2007).
- [131] W. A. Coish, J. Fischer, and D. Loss, Phys. Rev. B **77**, 125329 (2008).
- [132] L. Cywinski, W. M. Witzel, and S. Das Sarma, Phys. Rev. Lett. **102**, 057601 (2009).
- [133] K. Khodjasteh and D. A. Lidar, Phys. Rev. Lett. **95**, 180501 (2005).
- [134] W. Yao, R. B. Liu, and L. J. Sham, Phys. Rev. Lett. **98**, 077602 (2007).
- [135] W. M. Witzel and S. Das Sarma, Phys. Rev. Lett. **98**, 077601 (2007).
- [136] W. M. Witzel and S. Das Sarma, Phys. Rev. B **76**, 241303(R) (2007).
- [137] W. X. Zhang, V. V. Dobrovitski, L. F. Santos, L. Viola, and B. N. Harmon, Phys. Rev. B **75**, 201302(R) (MAY 2007).
- [138] W. X. Zhang, N. P. Konstantinidis, V. V. Dobrovitski, B. N. Harmon, L. F. Santos, and L. Viola, Phys. Rev. B **77**, 125336 (MAR 2008).
- [139] G. S. Uhrig, Phys. Rev. Lett. **98**, 100504 (2007).
- [140] B. Lee, W. M. Witzel, and S. Das Sarma, Phys. Rev. Lett. **100**, 160505 (2008).
- [141] W. Yang and R. B. Liu, Phys. Rev. Lett. **101**, 180403 (2008).
- [142] G. S. Uhrig, Phys. Rev. Lett. (2009), in press.
- [143] M. S. Rudner and L. S. Levitov, Phys. Rev. Lett. **99**, 036602 (2007).
- [144] H. Ribeiro and G. Burkard, Phys. Rev. Lett. **102**, 216802 (2009).
- [145] W. Yao, arXiv:0905.2460(2009).
- [146] A. Greilich, A. Shabaev, D. R. Yakovlev, A. L. Efros, I. A. Yugova, D. Reuter, A. Wieck, and M. Bayer, Science **317**, 1896 (2007).
- [147] X. Xu, W. Yao, B. Sun, D. G. Steel, A. S. Bracker, D. Gammon, and L. J. Sham, Nature **459**, 1105 (June 2009).
- [148] I. T. Vink, K. Nowack, F. Koppens, J. Danon, Y. Nazarov, and L. Vandersypen, arXiv:0902.2659(2009).
- [149] G. Giedke, J. M. Taylor, D. D'Alessandro, M. D. Lukin, and A. Imamoglu, Phys. Rev. A **74**, 032316 (2006).
- [150] D. Stepanenko, G. Burkard, G. Giedke, and A. Imamoglu, Phys. Rev. Lett. **96**, 136401 (2006).
- [151] D. Klauser, W. A. Coish, and D. Loss, Phys. Rev. B **73**, 205302 (2006).
- [152] L. M. Duan, E. Demler, and M. D. Lukin, Phys. Rev. Lett. **91**, 090402 (AUG 29 2003).
- [153] M. Keller, B. Lange, K. Hayasaka, W. Lange, and H. Walther, Nature **431**, 1075 (October 2004).
- [154] J. McKeever, A. Boca, A. Boozer, R. Miller, J. Buck, A. Kuzmich, and H. J. Kimble, Nature **303**, 1992 (March 2004).
- [155] B. Darquie, M. P. A. Jones, J. Dingjan, J. Beugnon, S. Bergamini, Y. Sortais, G. Messin, A. Browaeys, and P. Grangier, Science **309**, 454 (2005).
- [156] P. Michler, A. Kiraz, C. Becher, W. V. Schoenfeld, P. M. Petroff, L. Zhang, E. Hu, and A. Imamoglu, Science **290**, 2282 (Dec 2000).
- [157] M. Pelton, C. Santori, J. Vučković, B. Zhang, G. S. Solomon, J. Plant, and Y. Yamamoto, Phys. Rev. Lett. **89**, 233602 (December 2002).
- [158] J. Meijer, B. Burchard, M. Domhan, C. Wittmann, T. Gaebel, I. Popa, F. Jelezko, and J. Wrachtrup, App. Phys. Lett. **87**, 261909 (2005).
- [159] J. Meijer, T. Vogel, B. Burchard, I. Rangelow, L. Bischoff, J. Wrachtrup, M. Domhan, F. Jelezko, W. Schnitzler, S. Schulz, K. Singer, and F. Schmidt-Kaler, Appl. Phys. A - Mat. Sci. & Proc. **83**, 321 (2006).
- [160] L. J. Sham and T. M. Rice, Phys. Rev. **144**, 708 (Apr 1966).
- [161] F. H. L. Koppens, C. Buizert, K. J. Tielrooij, I. T. Vink, K. C. Nowack, T. Meunier, L. P. Kouwenhoven, and L. M. K. Vandersypen, Nature **442**, 766 (2006).
- [162] A. V. Khaetskii and Y. Nazarov, Phys. Rev. B **61**, 12639 (May 2000).
- [163] A. V. Khaetskii and Y. Nazarov, Phys. Rev. B **64**, 125316 (Sep 2001).
- [164] L. M. Woods, T. L. Reinecke, and Y. Lyanda-Geller, Phys. Rev. B **66**, 161318(R) (Oct 2002).
- [165] J. L. Cheng, M. W. Wu, and C. Lu, Phys. Rev. B **69**, 115318 (2004).
- [166] V. N. Golovach, A. Khaetskii, and D. Loss, Phys. Rev. Lett. **93**, 016601 (July 2004).
- [167] Y. G. Semenov and K. W. Kim, Phys. Rev. Lett. **92**, 026601 (Jan 2004).
- [168] P. San-Jose, G. Zarand, A. Shnirman, and G. Schoen, Phys. Rev. Lett. **97**, 076803 (AUG 18 2006).
- [169] G. F. Quinteiro and C. Piermarocchi, Phys. Rev. Lett. **72**, 045334 (JUL 2005).
- [170] X. D. Hu and S. Das sarma, Phys. Rev. Lett. **96**, 100501 (2006).
- [171] W. A. Coish and D. Loss, Phys. Rev. B **72**, 125337 (2005).
- [172] M. A. Nielsen and I. L. Chuang, *Quantum Computation and Quantum Information* (Cambridge University Press, Cambridge, 2000).
- [173] S. K. Saikin, C. Emary, D. G. Steel, and L. J. Sham, Phys. Rev. B **78**, 235314 (DEC 2008), ISSN 1098-0121.
- [174] J. M. Elzerman, R. Hanson, L. H. Willems van Beveren, B. Witkamp, L. M. K. Vandersypen, and L. P. Kouwenhoven, Nature **430**, 431 (July 2004).
- [175] T. Fujisawa, D. G. Austing, Y. Tokura, Y. Hirayama, and S. Tarucha, Nature **419**, 278 (2002).
- [176] M. Kroutvar, Y. Ducommun, D. Heiss, M. Bichler, D. Schuh, D. Abstreiter, and J. J. Finley, Nature **432**, 81 (2004).
- [177] J. Cheng, Y. Wu, X. Xu, D. Sun, D. G. Steel, A. S. Bracker, D. Gammon, W. Yao, and L. J. Sham, Solid State Comm. **140**, 381 (2006).
- [178] J. S. Hodges, J. C. Yang, C. Ramanathan, and D. G. Cory, Phys. Rev. A **78** (2008).
- [179] J. Du, X. Rong, N. Zhao, Y. Wang, J. Yang, and R. B. Liu, Nature **461** (2009).
- [180] F. H. L. Koppens, K. C. Nowack, and L. M. K. Vandersypen, Phys. Rev. Lett. **100**, 236802 (2008).
- [181] S. M. Clark, K.-M. C. Fu, Q. Zhang, T. D. Ladd, C. Stanley, and Y. Yamamoto, Phys. Rev. Lett. **102**, 247601 (2009).
- [182] A. Greilich, S. E. Economou, S. Spatzek, D. R. Yakovlev, D. Reuter, A. D. Wieck, T. L. Reinecke, and M. Bayer, Nature Phys. **5**, 262 (APR 2009).
- [183] D. P. DiVincenzo, Phys. Rev. A **51**, 1015 (1995).
- [184] S. Lloyd, Phys. Rev. Lett. **75**, 346 (May 1995).
- [185] K. Brunner, U. Bockelmann, G. Abstreiter, M. Walther, G. Böhm, G. Tränkle, and G. Weimann, Phys. Rev. Lett. **76**, 3216 (1992).

- [186] D. Gammon, B. V. Shanabrook, and D. S. Katzer, *Phys. Rev. Lett.* **67**, 1547 (1991).
- [187] T. H. Stievater, *Transient Nonlinear Spectroscopy of single quantum dots*, Ph.d. diss., University of Michigan (2001).
- [188] K. Brunner, G. Abstreiter, G. Böhm, G. Tränkle, and G. Weimann, *Appl. Phys. Lett.* **64**, 3320 (1994).
- [189] K. Brunner, G. Abstreiter, G. Böhm, G. Tränkle, and G. Weimann, *Phys. Rev. Lett.* **73**, 1138 (1994).
- [190] A. Zrenner, L. V. Butov, M. Hagn, G. Abstreiter, G. Böhm, and G. Weimann, *Phys. Rev. Lett.* **72**, 3382 (1994).
- [191] D. Gammon, E. S. Snow, and D. S. Katzer, *Appl. Phys. Lett.* **67**, 2391 (1995).
- [192] D. Gammon, E. S. Snow, B. V. Shanabrook, D. S. Katzer, and D. Park, *Phys. Rev. Lett.* **76**, 3005 (1996).
- [193] D. Gammon, E. S. Snow, B. V. Shanabrook, D. S. Katzer, and D. Park, *Science* **273**, 87 (1996).
- [194] M. E. Ware, E. A. Stinaff, D. Gammon, M. F. Doty, A. S. Bracker, D. Gershoni, V. L. Korenev, S. C. Bädescu, Y. Lyanda-Geller, and T. L. Reinecke, *Phys. Rev. Lett.* **95**, 177403 (2005).
- [195] E. A. Stinaff, M. Scheibner, A. S. Bracker, I. V. Ponomarev, V. L. Korenev, M. E. Ware, M. F. Doty, T. L. Reinecke, and D. Gammon, *Science* **311**, 636 (FEB 3 2006).
- [196] P. M. Petroff and S. P. DenBaars, *Superlattices and Microstructures* **15**, 15 (1994).
- [197] N. Richard, *Semicond. Sci. Tech.* **11**, 1365 (1996).
- [198] G. Chen, *Coherent Optical Spectroscopy and Manipulation of GaAs Quantum Dots*, Ph.d. diss., University of Michigan (2002).
- [199] P. M. Petroff, A. Lorke, and A. Imamoglu, *Physics Today* **54**, 45 (2001).
- [200] J. G. Tischler, A. S. Bracker, D. Gammon, and D. Park, *Phys. Rev. B* **66**, 081310 (2002).
- [201] W. G. van der Wiel, S. De Franceschi, J. M. Elzerman, T. Fujisawa, S. Tarucha, and K. L. P., *Rev. Mod. Phys.* **75**, 1 (2003).
- [202] A. C. Johnson, J. R. Petta, J. M. Taylor, A. Yacoby, M. D. Lukin, C. M. Marcus, M. P. Hanson, and A. C. Gossard, *Nature* **435**, 925 (2005).
- [203] F. Jelezko, T. Gaebel, I. Popa, A. Gruber, and J. Wrachtrup, *Phys. Rev. Lett.* **92**, 076401 (2004).
- [204] P. Tamarat, T. Gaebel, J. Rabeau, M. Khan, A. D. Greentree, H. Wilson, L. C. L. Hollenberg, S. Prawer, P. R. Hemmer, F. Jelezko, and J. Wrachtrup, *Phys. Rev. Lett.* **97**, 083002 (2006).
- [205] M. V. G. Dutt, J. Cheng, B. Li, X. Xu, X. Li, P. R. Berman, D. G. Steel, A. S. Bracker, D. Gammon, S. E. Economou, R.-B. Liu, and L. J. Sham, *Phys. Rev. Lett.* **94**, 227403 (2005).
- [206] A. Imamoglu, E. Knill, L. Tian, and P. Zoller, *Phys. Rev. Lett.* **91**, 017402 (Jul 2003).
- [207] W. H. Zurek, *Rev. Mod. Phys.* **75**, 715 (2003).
- [208] E. Joos, H. D. Zeh, C. Kiefer, D. Giulini, J. Kupsch, and I.-O. Stamatescu, *Decoherence and the appearance of a classical world in quantum theory*, 2nd ed. (Springer, New York, 2003).
- [209] M. Schlosshauer, *Rev. Mod. Phys.* **76**, 1267 (2004).
- [210] S. Amasha, K. MacLean, I. P. Radu, D. M. Zumbuhl, M. A. Kastner, M. P. Hanson, and A. C. Gossard, *Phys. Rev. Lett.* **100**, 046803 (2008).
- [211] A. Greilich, R. Oulton, E. A. Zhukov, I. A. Yugova, M. Yakovlev, D. R. Bayer, A. Shabaev, and A. L. Efros, *Phys. Rev. Lett.* **96**, 227401 (2006).
- [212] F. H. L. Koppens, J. A. Folk, J. M. Elzerman, R. Hanson, L. H. W. van Beveren, I. T. Vink, H. P. Tranitz, W. Wegscheider, L. P. Kouwenhoven, and L. M. K. Vandersypen, *Science* **309**, 1346 (2005).
- [213] J. Cheng, W. Yao, X. Xu, D. G. Steel, A. S. Bracker, D. Gammon, and L. J. Sham, *Phys. Rev. B* **77**, 115315 (2008).
- [214] L. Cywiński, W. M. Witzel, and S. Das Sarma, *Phys. Rev. B* **79**, 245314 (JUN 2009).
- [215] N. Bloembergen and T. J. Rowland, *Phys. Rev.* **97**, 1679 (1955).
- [216] P. W. Anderson, *Phys. Rev.* **99**, 623 (1955).
- [217] R. G. Shulman, J. M. Mays, and D. W. McCall, *Phys. Rev.* **100**, 692 (1955).
- [218] R. G. Shulman, B. J. Wyluda, and H. J. Hrostowski, *Phys. Rev.* **109**, 808 (1958).
- [219] R. K. Sundfors, *Phys. Rev.* **185**, 458 (1969).
- [220] W. M. Witzel and S. Das Sarma, *Phys. Rev. B* **74**, 35322 (2006).
- [221] W. Yang and R. B. Liu, *Phys. Rev. B* **78**, 085315 (2008).
- [222] W. Yang and R. B. Liu, *Phys. Rev. B* **79**, 115320 (2009).
- [223] A. Khaetskii, D. Loss, and L. Glazman, *Phys. Rev. B* **67**, 195329 (2003).
- [224] C. P. Slichter, *Principles of Magnetic Resonance*, 3rd ed. (Springer-Verlag, New York, 1992).
- [225] E. L. Hahn, *Phys. Rev.* **80**, 580 (1950).
- [226] P. P. Zanker, J. Schmidt, J. Schmiedeskamp, R. H. Acosta, and H. W. Spiess, *Phys. Rev. Lett.* **99**, 263001 (2007).
- [227] J. R. West, B. H. Fong, and D. A. Lidar, *Phys. Rev. Lett.* **104**, 130501 (Apr 2010).
- [228] A. Zrenner, *J. Chem. Phys.* **112**, 7790 (2000).
- [229] M. Bayer and A. Forchel, *Phys. Rev. B* **65**, 041308 (Jan 2002).
- [230] A. Muller, E. B. Flagg, P. Bianucci, X. Wang, D. G. Deppe, W. Ma, J. Zhang, M. Xiao, G. J. Salamo, and C. K. Shih, *Phys. Rev. Lett.* **99**, 187402 (2007).
- [231] T. H. Stievater, X. Q. Li, D. G. Steel, D. Gammon, D. S. Katzer, D. Park, C. Piermarocchi, and L. J. Sham, *Phys. Rev. Lett.* **87**, 133603 (September 2001).
- [232] H. Htoon, T. Takagahara, D. Kulik, O. Baklenov, A. L. Holmes, Jr., and C. K. Shih, *Phys. Rev. Lett.* **88**, 087401 (2002).
- [233] H. Kamada, H. Gotoh, J. Temmyo, T. Takagahara, and H. Ando, *Phys. Rev. Lett.* **87**, 246401 (2001).
- [234] A. Zrenner, E. Beham, S. Stuffer, F. Findeis, M. Bichler, and G. Abstreiter, *Nature* **418**, 612 (2002).
- [235] G. Chen, T. H. Stievater, E. T. Batteh, X. Q. Li, D. G. Steel, D. Gammon, D. S. Katzer, D. Park, and L. J. Sham, *Phys. Rev. Lett.* **88**, 117901 (March 2002).
- [236] J. Berezovsky, M. H. Mikkelsen, N. G. Stoltz, L. A. Coldren, and D. D. Awschalom, *Science* **320**, 349 (2008).
- [237] I. A. Merkulov, A. L. Efros, and M. Rosen, *Phys. Rev. B* **65**, 205309 (2002).

- [238] A. S. Bracker, D. Gammon, and V. L. Korenev, *Semicond. Sci. Technol.*, 114004(2008).
- [239] C. W. Lai, P. Maletinsky, A. Badolato, and A. Imamoglu, *Phys. Rev. Lett.* **96**, 167403 (2006).
- [240] A. I. Tartakovskii, T. Wright, A. Russell, V. I. Fal'ko, A. B. Van'kov, J. Skiba-Szymanska, I. Drouzas, R. S. Kolodka, M. S. Skolnick, P. W. Fry, A. Tahraoui, H.-Y. Liu, and M. Hopkinson, *Phys. Rev. Lett.* **98**, 026806 (2007).
- [241] B. Eble, O. Krebs, A. Lemaître, K. Kowalik, A. Kudelski, P. Voisin, B. Urbaszek, X. Marie, and T. Amand, *Phys. Rev. B* **74**, 081306 (2006).
- [242] P.-F. Braun, X. Marie, L. Lombez, B. Urbaszek, T. Amand, P. Renucci, V. K. Kalevich, K. V. Kavokin, O. Krebs, P. Voisin, and Y. Masumoto, *Phys. Rev. Lett.* **94**, 116601 (Mar 2005).
- [243] K. Ono and S. Tarucha, *Phys. Rev. Lett.* **92**, 256803 (Jun 2004).
- [244] L. Viola and S. Lloyd, *Phys. Rev. A* **58**, 2733 (1998).
- [245] L. Viola, E. Knill, and S. Lloyd, *Phys. Rev. Lett.* **82**, 2417 (1999).
- [246] L. Viola, S. Lloyd, and E. Knill, *Phys. Rev. Lett.* **83**, 4888 (1999).
- [247] L. Viola, E. Knill, and S. Lloyd, *Phys. Rev. Lett.* **85**, 3520 (2000).
- [248] P. W. Shor, *Phys. Rev. A* **52**, 2493 (October 1995).
- [249] A. M. Steane, *Phys. Rev. Lett.* **77**, 793 (1996).
- [250] C. H. Bennett, D. P. DiVincenzo, J. A. Smolin, and W. K. Wootters, *Phys. Rev. A* **54**, 3824 (1996).
- [251] R. Laflamme, C. Miquel, J. P. Paz, and W. H. Zurek, *Phys. Rev. Lett.* **77**, 198 (1996).
- [252] D. Gottesman, *Phys. Rev. A* **54**, 1862 (1996).
- [253] A. M. Steane, *Phys. Rev. A* **68**, 042322 (October 2003).
- [254] D. Brunner, B. D. Gerardot, P. A. Dalgarno, G. Wüst, K. Karrai, N. G. Stoltz, P. M. Petroff, and R. J. Warburton, *Science* **325**, 70 (2009).
- [255] B. D. Gerardot, D. Brunner, P. A. Dalgarno, P. Hberg, S. Seidl, M. Kroner, K. Karrai, N. G. Stoltz, P. M. Petroff, and R. J. Warburton, *Nature* **451**, 441 (2008).
- [256] M. Atatüre, J. Dreiser, A. Badolato, A. Högele, K. Karrai, and A. Imamoglu, *Science* **312**, 551 (2006).
- [257] X. Xu, Y. Wu, B. Sun, Q. Huang, J. Cheng, D. G. Steel, A. S. Bracker, D. Gammon, C. Emary, and L. J. Sham, *Phys. Rev. Lett.* **99**, 097401 (AUG 31 2007).
- [258] R. Hanson and D. D. Awschalom, *Nature* **453**, 1043 (2008).
- [259] G. Balasubramanian, P. Neumann, D. Twitchen, M. Markham, R. Kolesov, N. Mizuochi, J. Isoya, J. Achard, J. Beck, J. Tissler, V. Jacques, P. R. Hemmer, F. Jelezko, and J. Wrachtrup, *Nature Materials* **8**, 383 (2009).
- [260] Y. S. Park, A. K. Cook, and H. L. Wang, *Nano Lett.* **6**, 2075 (2006).
- [261] S. Schietinger, T. Schroeder, and O. Benson, *Nano Lett.* **8**, 3911 (2008).
- [262] K. M. C. Fu, C. Santori, P. E. Barclay, I. Aharonovich, S. Praver, N. Meyer, A. M. Holm, and R. G. Beausoleil, *Appl. Phys. Lett.* **93**, 234107 (2008).
- [263] M. Barth, N. Nuisse, B. Loechel, and O. Benson, *Optics Lett.* **34**, 1108 (2009).
- [264] P. Neumann, N. Mizuochi, F. Rempp, P. Hemmer, H. Watanabe, S. Yamasaki, V. Jacques, T. Gaebel, F. Jelezko, and J. Wrachtrup, *Science* **320**, 1326 (2008).
- [265] L. Jiang, J. S. Hodges, J. R. Maze, P. Maurer, J. M. Taylor, D. G. Cory, P. R. Hemmer, R. L. Walsworth, A. Yacoby, A. S. Zibrov, and M. D. Lukin, *Science* **326**, 267 (2009).
- [266] M. Steiner, P. Neumann, J. Beck, F. Jelezko, and J. Wrachtrup, *Phys. Rev. B* **81**, 035205 (Jan 2010).
- [267] X. Wang, X. Ren, K. Kahen, M. A. Hahn, M. Rajeswaran, S. Maccagnano-Zacher, J. Silcox, G. E. Cragg, A. L. Efros, and T. D. Krauss, *Nature* **459**, 686 (2009).
- [268] M. Bayer, P. Hawrylak, K. Hinzer, S. Fafard, M. Korkusinski, Z. Wasilewski, O. Stern, and A. Forchel, *Science* **291**, 451 (JAN 19 2001), ISSN 0036-8075.
- [269] H. J. Krenner, M. Sabathil, E. C. Clark, A. Kress, D. Schuh, M. Bichler, G. Abstreiter, and J. J. Finley, *Phys. Rev. Lett.* **94**, 057402 (FEB 11 2005).
- [270] R. Songmuang, S. Kiravittaya, and O. G. Schmidt, *Appl. Phys. Lett.* **82**, 2892 (APR 28 2003).
- [271] J. V. Barth, G. Costantini, and K. Kern, *Nature* **437**, 671 (SEP 29 2005).
- [272] M. Schmidbauer, S. Seydmohamadi, D. Grigoriev, Z. M. Wang, Y. I. Mazur, P. Schafer, M. Hanke, R. Kohler, and G. J. Salamo, *Phys. Rev. Lett.* **96**, 066108 (FEB 17 2006).
- [273] N. H. Bonadeo, G. Chen, D. Gammon, D. S. Katzer, D. Park, and D. G. Steel, *Phys. Rev. Lett.* **81**, 2759 (Sep 1998).
- [274] J. I. Cirac, A. K. Ekert, S. F. Huelga, and C. Macchiavello, *Phys. Rev. A* **59**, 4249 (June 1999).
- [275] C. H. Bennett, F. Bessette, G. Brassard, L. Salvail, and J. Smolin, *J. Cryptology* **5**, 3 (1992).
- [276] E. Knill, R. Laflamme, and G. J. Milburn, *Nature* **409**, 46 (Jan 2001).
- [277] J. I. Cirac, P. Zoller, H. J. Kimble, and H. Mabuchi, *Phys. Rev. Lett.* **78**, 3221 (Apr 1997).
- [278] K. J. Vahala, *Nature* **424**, 839 (Aug 2003).
- [279] E. Peter, P. Senellart, D. Martrou, A. Lemaître, J. Hours, J. M. Gérard, and J. Bloch, *Phys. Rev. Lett.* **95**, 067401 (August 2005).
- [280] A. Scherer, O. Painter, J. Vuckovic, M. Loncar, and T. Yoshie, *IEEE Transactions on Nanotechnology* **1**, 4 (Mar 2002).
- [281] A. Kress, F. Hofbauer, N. Reinelt, M. Kaniber, H. J. Krenner, R. Meyer, G. Böhm, and J. J. Finley, *Phys. Rev. B* **71**, 241304 (Jun 2005).
- [282] Y. Akahane, T. Asano, B.-S. Song, and S. Noda, *Nature* **425**, 944 (October 2003).
- [283] B.-S. Song, S. Noda, T. Asano, and Y. Akahane, *Nature Material* **4**, 207 (2005).
- [284] T. Yoshie, A. Scherer, J. Hendrickson, G. Khitrova, H. M. Gibbs, G. Rupper, C. Ell, O. B. Shchekin, and D. G. Deppe, *Nature* **432**, 200 (November 2004).
- [285] K. Hennessy, A. Badolato, M. Winger, D. Gerace, M. Atatüre, S. Gulde, S. Falt, E. Hu, and A. Imamoglu, *Nature* **445**, 896 (2007).
- [286] J. P. Reithmaier, G. Sek, A. Löffler, C. Hofmann, S. Kuhn, S. Reitzenstein, L. V. Keldysh, V. D. Kulakovskii, T. L. Reinecke, and A. Forchel, *Nature* **432**, 197 (2004).

- [287] N. G. Stoltz, M. Rakher, S. Strauf, A. Badolato, D. D. Lofgreen, P. M. Petroff, L. A. Coldren, and D. Bouwmeester, *Appl. Phys. Lett.* **87**, 031105 (2005).
- [288] D. Press, S. Gotzinger, S. Reitzenstein, C. Hofmann, A. Löffler, M. Kamp, A. Forchel, and Y. Yamamoto, *Phys. Rev. Lett.* **98**, 117402 (2007).
- [289] A. Müller, C. K. Shih, J. Ahn, D. Lu, and D. G. Deppe, *Opt. Lett.* **31**, 528 (2006).
- [290] X. D. Fan, P. Palinginis, S. Lacey, H. L. Wang, and M. C. Lonergan, *Opt. Lett.* **25**, 1600 (Nov 2000).
- [291] B. Min, T. J. Kippenberg, and K. J. Vahala, *Opt. Lett.* **28**, 1507 (Sep 2003).
- [292] N. Le Thomas, U. Woggon, O. Schops, M. V. Artemyev, M. Kazes, and U. Banin, *Nano. Lett.* **6**, 557 (2006).
- [293] D. K. Armani, T. J. Kippenberg, S. M. Spillane, and K. J. Vahala, *Nature* **421**, 925 (February 2003).
- [294] S. M. Spillane, T. J. Kippenberg, K. J. Vahala, K. W. Goh, E. Wilcut, and H. J. Kimble, *Phys. Rev. A* **71**, 013817 (2005).
- [295] M. Cai, O. Painter, and K. J. Vahala, *Phys. Rev. Lett.* **85**, 74 (2000).
- [296] S. M. Spillane, T. J. Kippenberg, O. J. Painter, and K. J. Vahala, *Phys. Rev. Lett.* **91**, 043902 (2003).
- [297] T. J. Kippenberg, S. M. Spillane, D. K. Armani, and K. J. Vahala, *Appl. Phys. Lett.* **83**, 797 (July 2003).
- [298] P. Barclay, K. Srinivasan, and O. Painter, *J. Opt. Soc. Am. B* **20**, 2274 (2003).
- [299] K. Srinivasan, P. Barclay, M. Borselli, and O. Painter, *IEEE J. Sel. Areas Commun.* **23**, 1321 (2005).
- [300] K. Srinivasan, P. Barclay, O. Painter, B. Lev, and H. Mabuchi, *Appl. Phys. Lett.* **89**, 131108 (2006).
- [301] A. Faraon, E. Waks, D. Englund, I. Fushman, and J. Vuckovic, *Appl. Phys. Lett.* **90**, 073102 (2007).
- [302] A. Badolato, K. Hennessy, M. Atatüre, J. Dreiser, E. Hu, P. M. Petroff, and A. Imamoglu, *Science* **308**, 1158 (2005).
- [303] S. M. Thon, M. T. Rakher, H. Kim, J. Gudat, W. T. M. Irvine, P. M. Petroff, and D. Bouwmeester, *Appl. Phys. Lett.* **94**, 111115 (2009).
- [304] A. Laucht, F. Hofbauer, N. Hauke, J. Angele, S. Stobbe, M. Kaniber, G. Böhm, P. Lodahl, M. C. Amann, and J. J. Finley, *New J. Phys.* **11**, 023034 (2009).
- [305] M. Kaniber, A. Neumann, A. Laucht, M. F. Huck, M. Bichler, M. C. Amann, and J. J. Finley, *New J. Phys.* **11**, 013031 (2009).
- [306] M. T. Rakher, N. G. Stoltz, L. A. Coldren, P. M. Petroff, and D. Bouwmeester, *Appl. Phys. Lett.* **93**, 091118 (2008).
- [307] M. T. Rakher, N. G. Stoltz, L. A. Coldren, P. M. Petroff, and D. Bouwmeester, *Phys. Rev. Lett.* **102**, 097403 (2009).
- [308] E. B. Flagg, A. Müller, J. W. Robertson, S. Founta, D. G. Deppe, M. Xiao, W. Ma, G. J. Salamo, and C. K. Shih, *Nature Physics* **5**, 203 (2009).
- [309] W. Yao, R. B. Liu, and L. J. Sham, *J. Appl. Phys.* **101**, 081721 (2007).
- [310] K. Bergmann, H. Theuer, and B. W. Shore, *Rev. Mod. Phys.* **70**, 1003 (1998).
- [311] C. E. Pryor and M. E. Flatte, *Appl. Phys. Lett.* **88**, 233108 (JUN 5 2006), ISSN 0003-6951.
- [312] Y. Wu, E. D. Kim, X. Xu, J. Cheng, D. G. Steel, A. S. Bracker, D. Gammon, S. E. Economou, and L. J. Sham, *Phys. Rev. Lett.* **99**, 097402 (2007).
- [313] D. Press, K. De Greve, P. L. McMahon, T. D. Ladd, B. Friess, C. Schneider, M. Kamp, S. Hofling, A. Forchel, and Y. Yamamoto, *Nature Photonics* **4**, 347 (2010).
- [314] D. Goswami, *Phys. Report* **374**, 385 (2003).
- [315] G. Ortner, M. Bayer, A. Larionov, V. B. Timofeev, A. Forchel, Y. B. Lyanda-Geller, T. L. Reinecke, P. Hawrylak, S. Fafard, and Z. Wasilewski, *Phys. Rev. Lett.* **90** (FEB 28 2003).
- [316] H. J. Krenner, E. C. Clark, T. Nakaoka, M. Bichler, C. Scheurer, G. Abstreiter, and J. J. Finley, *Phys. Rev. Lett.* **97**, 076403 (AUG 18 2006).
- [317] B. D. Gerardot, S. Strauf, M. J. A. de Dood, A. M. Bychkov, A. Badolato, K. Hennessy, E. Hu, D. Bouwmeester, and P. M. Petroff, *Phys. Rev. Lett.* **95**, 137403 (SEP 23 2005).
- [318] M. Scheibner, M. F. Doty, I. V. Ponomarev, A. S. Bracker, E. A. Stinaff, V. L. Korenev, T. L. Reinecke, and D. Gammon, *Phys. Rev. B* **75**, 245318 (JUN 2007).
- [319] M. Scheibner, M. Yakes, A. S. Bracker, I. V. Ponomarev, M. F. Doty, C. S. Hellberg, L. J. Whitman, T. L. Reinecke, and D. Gammon, *Nature Physics* **4**, 291 (APR 2008).
- [320] R. S. Judson and H. Rabitz, *Phys. Rev. Lett.* **68**, 1500 (1992).
- [321] W. S. Warren, H. Rabitz, and M. Dahleh, *Science* **259**, 1581 (MAR 12 1993).
- [322] H. Rabitz, R. de Vivie-Riedle, M. Motzkus, and K. Kompa, *Science* **288**, 824 (May 2000).
- [323] A. Shabaev, A. L. Efros, D. Gammon, and I. A. Merkulov, *Phys. Rev. B* **68**, 201305(R) (November 2003).
- [324] M. Friesen, C. Tahan, R. Joynt, and M. A. Eriksson, *Phys. Rev. Lett.* **92**, 037901 (January 2004).
- [325] C. Emary, X. Xu, D. G. Steel, S. Saikin, and L. J. Sham, *Phys. Rev. Lett.* **98**, 047401 (JAN 26 2007).
- [326] D. Kim, S. E. Economou, S. C. Badescu, M. Scheibner, A. S. Bracker, M. Bashkansky, T. L. Reinecke, and D. Gammon, *Phys. Rev. Lett.* **101**, 236804 (DEC 5 2008).
- [327] U. Bockelmann and G. Bastard, *Phys. Rev. B* **42**, 8947 (1990).
- [328] B. Ohnesorge, M. Albrecht, J. Oshinowo, A. Forchel, and Y. Arakawa, *Phys. Rev. B* **54**, 11532 (1996).
- [329] S. Cortez, O. Krebs, S. Laurent, M. Senes, X. Marie, P. Voisin, R. Ferreira, G. Bastard, J. M. Gérard, and T. Amand, *Phys. Rev. Lett.* **89**, 207401 (2002).
- [330] S. Trumm, M. Wesseli, H. J. Krenner, D. Schuh, M. Bichler, J. J. Finley, and M. Betz, *Appl. Phys. Lett.* **87**, 153113 (2005).
- [331] N. H. Bonadeo, *Nano-optics: Coherent Optical Spectroscopy of Single Semiconductor Quantum Dots*, Ph.d. diss., The University of Michigan (1999).
- [332] M. Atatüre, J. Dreiser, A. Badolato, and A. Imamoglu, *Nature Physics* **3**, 101 (2007).
- [333] M. H. Mikkelsen, J. Berezovsky, N. G. Stoltz, L. A. Coldren, and D. D. Awschalom, *Nature Phys.* **3**, 770 (NOV 2007).
- [334] L. Jiang, J. S. Hodges, J. R. Maze, P. Maurer, J. M. Taylor, D. G. Cory, P. R. Hemmer, R. L. Walsworth, A. Yacoby, A. S. Zibrov, and M. D. Lukin, *Science* **326**, 267 (2009).
- [335] D. F. V. James, P. G. Kwiat, W. J. Munro, and A. G. White, *Phys. Rev. A* **64**, 052312 (October 2001).

- [336] D. G. Cory, A. F. Hahmy, and T. F. Havel, Proc. Natl. Acad. Sci. USA **94**, 1634 (March 1997).
- [337] S. Takeuchi, J. Kim, Y. Yamamoto, and H. H. Hogue, Appl. Phys. Lett. **74**, 1063 (February 1999).
- [338] P. Barclay, K. Srinivasan, and O. Painter, Opt. Express **13**, 801 (2005).
- [339] K. Srinivasan, P. E. Barclay, M. Borselli, and O. Painter, Phys. Rev. B **70**, 081306 (Aug 2004).
- [340] P. E. Barclay, K. Srinivasan, M. Borselli, and O. Painter, Appl. Phys. Lett. **85**, 4 (2004).
- [341] M. J. Cryan, Journal of Lightwave Technology **27**, 4841 (2009).
- [342] Y. Sugimoto, Y. Tanaka, N. Ikeda, Y. Nakamura, K. Asakawa, and K. Inoue, Opt. Express **12**, 1090 (2004).
- [343] J. Crisp and B. Elliott, *Introduction to Fiber Optics* (Newnes, 2005).
- [344] A. Kuhn, M. Hennrich, and G. Rempe, Phys. Rev. Lett. **89**, 067901 (August 2002).
- [345] A. D. Boozer, A. Boca, R. Miller, T. E. Northup, and H. J. Kimble, Phys. Rev. Lett. **98**, 193601 (2007).
- [346] A. S. Parkins and H. J. Kimble, J. Opt. B: Quant. Semiclass. Optics **1**, 496 (1999).
- [347] M. Fleischhauer, S. F. Yelin, and M. D. Lukin, Opt. Comm. **179**, 395 (2000).
- [348] W. Yao, R. B. Liu, and L. J. Sham, J. Optics B - Quantum & Semiclassical Optics **7**, S318 (2005).
- [349] D. Fattal, R. Beausoleil, and Y. Yamamoto, quant-ph/0606204(2006).
- [350] X. Marie, T. Amand, P. Le Jeune, M. Paillard, P. Renucci, L. E. Golub, V. D. Dymnikov, and E. L. Ivchenko, Phys. Rev. B **60**, 5811 (Aug 1999).
- [351] M. D. Lukin, S. F. Yelin, and M. Fleischhauer, Phys. Rev. Lett. **84**, 4232 (2000).
- [352] R. J. Levis, G. M. Menkir, and H. Rabitz, Science **292**, 709 (2001).
- [353] H. M. Wiseman and G. J. Milburn, Phys. Rev. Lett. **70**, 548 (February 1993).
- [354] J. M. Geremia, J. K. Stockton, and H. Mabuchi, Science **304**, 270 (2004).
- [355] S. J. van Enk, J. I. Cirac, and P. Zoller, Science **279**, 205 (1998).
- [356] H. J. Briegel, W. Dür, J. I. Cirac, and P. Zoller, Phys. Rev. Lett. **81**, 5932 (1998).
- [357] t. Chen and R. B. Liu (unpublished).
- [358] F. Verluise, V. Laude, Z. Cheng, C. Spielmann, and P. Tournois, Optics Lett. **25**, 575 (April 2000).
- [359] C. W. Hillegas, J. X. Tull, D. Goswami, D. Strickland, and W. S. Warren, Opt. Lett. **19**, 737 (MAY 15 1994).
- [360] X. Q. Li, T. H. Zhang, C. N. Borca, and S. T. Cundiff, Phys. rev. Lett. **96**, 57406 (2006).
- [361] M. Cho, Chem. Rev. **108**, 1331 (APR 2008).
- [362] S. Mukamel, Annual Rev. Phys. Chem. **51**, 691 (2000).
- [363] P. F. Tian, D. Keusters, Y. Suzuki, and W. S. Warren, Science **300**, 1553 (2003).
- [364] P. Y. Yu and M. Cardona, *Fundamentals of Semiconductors*, 1st ed. (Springer, Berlin, 1996).
- [365] A. V. Koudinov, I. A. Akimov, Y. G. Kusrayev, and F. Henneberger, Phys. Rev. B **70**, 241305 (2004).
- [366] D. Paget, G. Lampel, and B. Sapoval, Phys. Rev. B **15**, 5780 (1977).
- [367] D. Paget, T. Amand, and J.-P. Korb, Phys. Rev. B **77**, 245201 (2008).
- [368] P. Maletinsky, M. Kroner, and A. Imamoglu, Nat. Phys. **5**, 407 (2009).
- [369] S. Popescu, A. J. Short, and A. Winter, Nature Physics **2**, 754 (2006).